Delft University of Technology

RINGEN Geothermal Project Development MDP

Authors:
Sjoerd Akkermans (4958403)
John Sass (5713862)
Luis Barlet (5849454)
Esther Zijlstra (4849752)
Ayush Jha (5711673)

January 10, 2024

Abstract

In this multidisciplinary project several aspects of geosciences are combined. The regional geology background was summarized and linked to the borehole data.

Multiple tests were conducted on the well to answer several questions. The slug test indicated that the fracture is still open and essentially confirmed that it is a shear fracture, however it is unclear to what extent that the fracture is open. The fracture seems to be hydraulically connected to a permeable unit or shallow aquifer. Unfortunately, the length of the fracture could not be determined with the data collected from the test.

Electrical resistivity tomography (ERT) and seismics were both applied to a location near the borehole to acquire lateral information of the subsurface. The ERT results showed that the layers were horizontally continuous and indicated layers with different compositions based on resistive properties.

Seismic refraction tomography conducted along a part of the same profile showed similar results as the ERT for that part of the profile. P-wave velocities indicate a horizontally layered subsurface in the upper 40m. Additionally surface wave analysis of the same setup utilizing active and passive measurements resulted in a vertical s-wave velocity profile that can be used for future implementation of the planned Borehole Thermal Energy Storage (BTES) system.

The last geophysical method was using gravity data on the region around the site. A map was made by using available data on changes in gravity in the region and plotting the results. On this map the location of remnants of volcanos and the Litoměřice deep fault can be recognised.

Thermal properties of cores were analyzed using a Hot Disk and an optical scanner. Unfortunately the drilling of a new well from which the cores were to be analyzed was delayed, and cores from an uranium mine were used. This way the advantages and disadvantages of both measuring devices could be argued and used for future research.

Past analysis of geothermal regions have shown that exploration of geothermal energy causes surface displacement. It can also be observed during the drilling phase. Interferometric Synthetic Aperture Radar (InSAR) and Global Navigation Satellite System (GNSS) are valuable tools to monitor land surface changes. Measurement of surface deformation being one of its many applications. For this study, the above tools have been used to measure surface displacement in the region of Litoměřice.

Contents

1 Project Introduction

When discussing geothermal energy in the context of the energy transition, the most widely known sources are those located in high-temperature regions such as Iceland, Larderello (Italy), Kenya, Indonesia, the Western United States, or the Philippines. In these regions, very high temperature gradients exist at depths that are able to be reached economically with wells. These resources are very productive and hold the capability to produce both electricity and heat, but the benefits of geothermal energy are not limited to just extremely high-temperature regions.

In the Ústí nad Labem Region of the Czech Republic, the town of Litoměřice is home to the RINGEN geothermal development project. The goal of the project is to use the unique geology of the region to host a specialised geothermal research center. At this center, enhanced geothermal systems (EGS) and borehole energy storage (BTES) systems will be developed to both power and store energy for the local area.

The project is designed for research purposes as a number of pilot wells and monitoring systems are in place and planned. One such well is the PVGT-LT1 pilot well for EGS research. This well was designed to obtain a more reliable data for temperature estimates for depths as deep as 5 km, which is considered still economically viable [22]. A number of pilot wells will be drilled in the near future to gather data relevant to BTES operation at the site. For monitoring systems, a unique network that includes both ground seismometers and dilatometres and underground stations is in place and will be expanded with the creation of new wells.

2 Multi-Disciplinarity

Multi-disciplinarity is one of the core goals of this project. We strive to combine several Applied Earth Sciences disciplines within one project. In this report we use a wide variety of techniques and methods to create a better understanding of the sub-surface. To be more precise, the subsurface around the RINGEN project in Litoměřice. The information gathered in this project can be utilized to further develop geothermal energy in the Ústí nad Labem Region of the Czech Republic.

- **Geophysics:** We have used electrical resistivity tomography, seismics, and gravitational data to create a geophysical picture of the sub-surface.
- **Remote Sensing:** We have used inSAR and GNSS to look at the temporal evolution of the surface.
- **Well testing:** We have used well-testing techniques to make approximations of flow properties such as matrix permeability and various fracture properties.
- **Core analysis:** We have used both optical scanning and hot disk scanning to analyse the heat conductivity of wellbore cores.

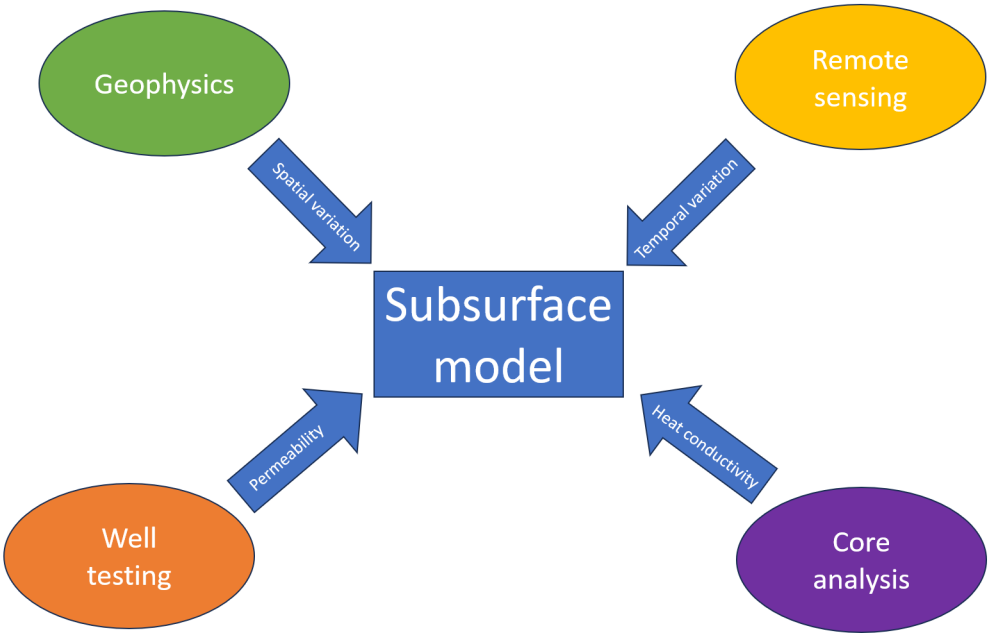

Figure 1: Diagram of how different aspects of the MDP are interconnected

3 Geology background Litoměřice area

This section will describe the geological history of the area around Litoměřice, including the occurring rock types, depositional environments, important brittle structures and relevant deformation processes. This will then be linked to the lithology of the PVGT-LT1 pilot borehole. Lastly there will be a short part on the thermal properties and geothermal potential of the area.

3.1 Regional geology

Litoměřice is located south-east of the Eger rift and in the Bohemian Cretaceous Basin. The area went through the Variscan orogeny, volcanism during the Upper-Carboniferous, was filled with continental siliciclastic sediments in the Upper-Carboniferous and with shallow marine sediments during the Cretaceous. During the Cenozoic, tectonic extensional activity lead to crustal thinning and consequently an increased heat flux. From the Oligocene onwards the tectonic activity caused the formation of the Eger rift system, followed by subsidence, sedimentation and basin closure. [5]

The Variscan metamorphic rocks are from the Teplá-Barrandian and Saxothuringian zones and form the crystalline basement rock. The contact between these zones contain high pressure rocks and that contact zone is mostly hidden by the overlying rocks. The location of the contact was estimated by St'ovicková (1973) by using gravity data. The Tepla-Barrandian rocks mainly consist of high-density metamorphic rock and the Saxothuringian rocks are predominantly low-density, therefore the maximum gravity gradient would indicate the boundary which is called the "Litoměřice deep fault". [18] [28]

In the PVGT-LT1 borehole (Figure 3) fairly homogeneous mica-schists with garnet-kyanite were found at the depth of the basement rock, below 900 meters. From the depth of approximately 1790m until the bottom of the well at 2110m there were greenschists present, as well as chlorite-sericite graphitic phyllites with pyrite or magnitite. [22]

The volcanic deposits from the Upper Carboniferous are rhyolite ignimbrites from the Altenberg-Teplice caldera volcanic complex. In the PVGT-LT1 borehole the rhyolite ignimbrites were fine grained and grey of colour. [22] The Carboniferous siliciclastic sediments were deposited on top of the volcanic rhyolite ignimbrites. The thickness of this sediment is variable due to the influence of pre-Cenomanian erosion of the top part. It increases from tens of meters in the south to approximately a kilometer in the basin centre. [8] The infill consists of four formations: Kladno, Týnec, Slaný and Líně formations, all of which were found to be present in the PVGT-LT1 borehole [22].

The Bohemian Cretaceous Basin was a marine basin which opened through NE-SW trending faults which were reactivated as a result of the alpine collisional zone and/or spreading of the bay of Biscay and northern Atlantic ocean. The reactivated faults originated from the Variscan basement of the Bohemian Massif. [31] [27] The infill is sandstone dominated with fine grained siliciclastics and carbonate offshore deposits towards the SE and reaches a maximum thickness of around 300 meters. [29] The Upper-Cretaceous can be subdivided into the following formations: Peruc-Korycany, Bílá Hora, Jizera, Teplice, Březno. The Peruc-Korycany contains sand- and claystones reaching a thickness of around 90 meters, followed by 40 to 90 meters of the marine sandstones of the Bílá Hora formation and 20 to 200 meters of similar rock types of the Jizera formation. The Teplice formation contains mud- and marlstones with small layers of limestone in between, with a thickness of up to 100 meters. Lastly, the Březno formation makes up the top of the Bohemian Cretaceous Basin and consists of mudstones. [22]

During the Cenozoic the area was tectonically active, with crustal compression until the Eocene and extensional movement since the Oligocene. [1] The extensional movement caused crustal thinning and subsequently volcanic activity and an increased heat flux, which is valuable for geothermal exploration. During the Late Eocene to Late Miocene volcanic activity was present in the Eger Graben. [5]

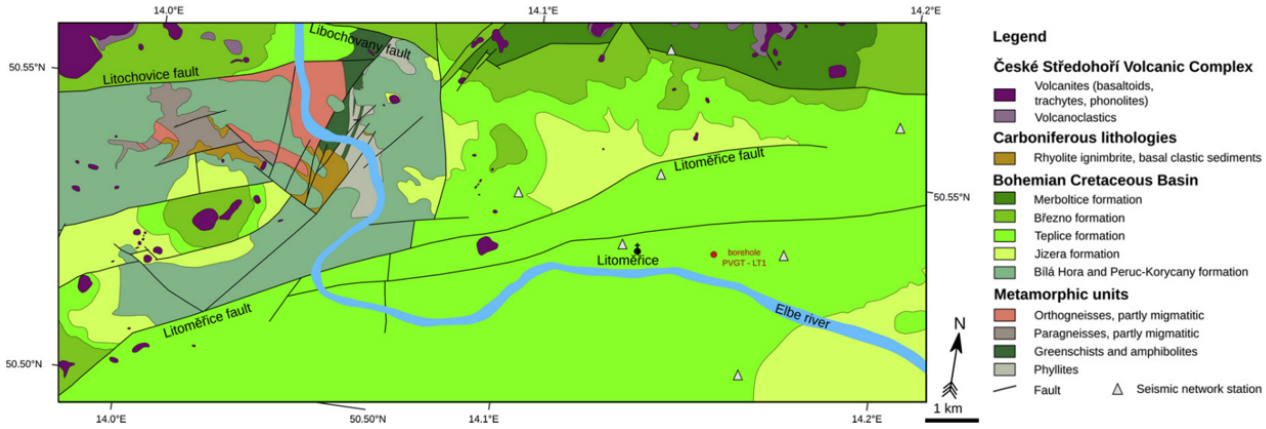

Figure 2: Regional geology and legend from Safanda et al. (2020) [22]

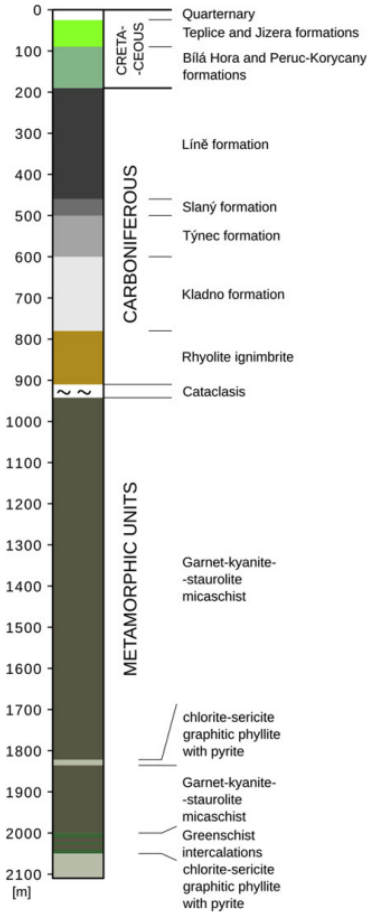

Figure 3: Lithology of the PVGT-LT1 borehole in Litoměřice

3.2 Thermal underground properties

The Litoměřice area shows an indicated heat flux of about 70-80 mW/m^2 and taking into account the effect of heat production this increases to 78 to 88 mW/m^2 [6]. Temperature logging measurements were previously taken in the borehole on several dates which can be seen in Figure 4. In 2007 the measured temperature at a depth of 1800m is 55.9 °C. In 2018 the temperature logging results were compared with the results from September 2007 and it was concluded that the largest difference between them was the 1 to 1.5 °C decrease in temperature in the upper part of the borehole. This decrease becomes smaller with depth, reaching zero at 1000m and increases slowly after 1100m. Using this difference the temperature at 1800m depth was extrapolated, which resulted in

an estimation of 57.5 °C.

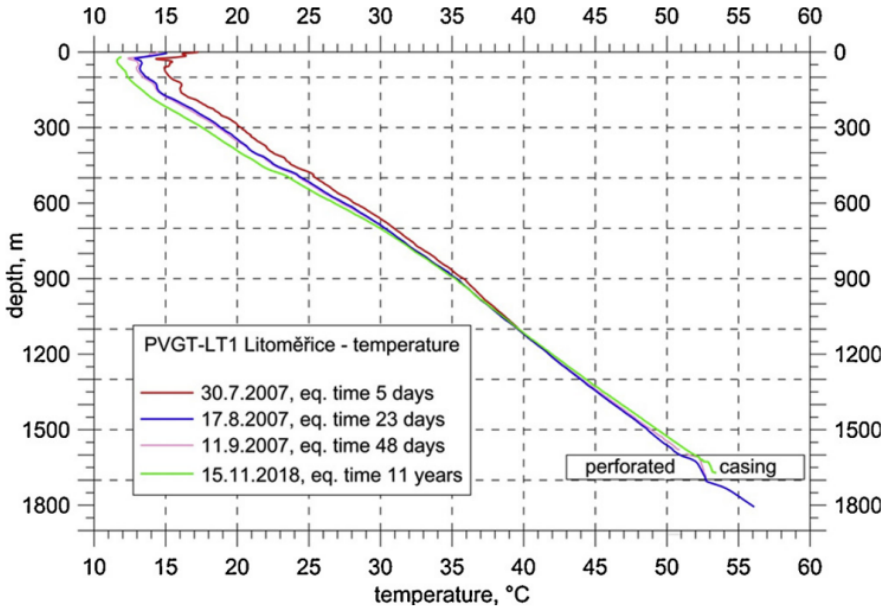

Figure 4: Temperature logging results from several tests conducted in the PVGT-LT1 borehole

4 Previous Injection Tests and Conclusions

4.1 January 2020 Injection Test

During an injection test on January 24th 2020, a fracture was unintentionally created in the PVGT-LT1 borehole in Litoměřice when the surface injection pressure exceeded 40 bar. An immediate increase in injection rate was measured as well as a decrease in injection pressure. This is indicative of a conductive fracture being formed. The increase in pressure to 41 bar can be seen in Figure 5 as the small single pressure peak around 16:00h on January 25th. Following this peak, the sharp decrease in pressure and the rapid increase in rate can be seen.

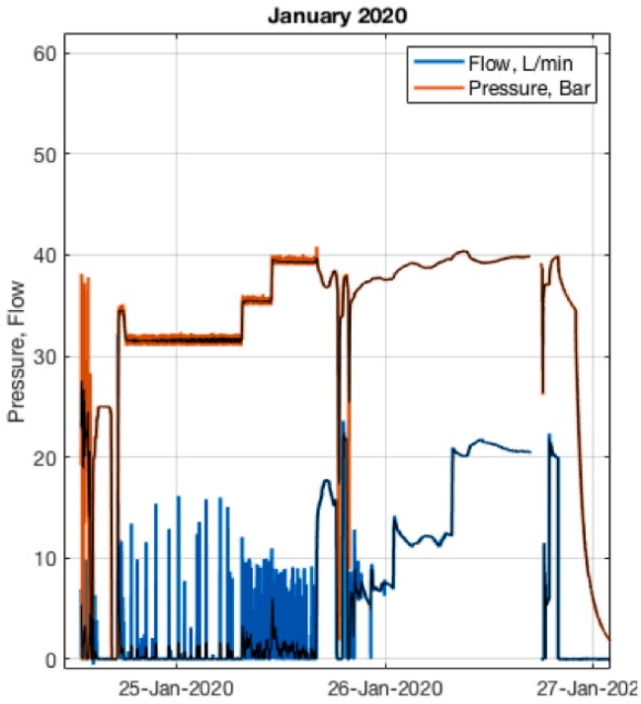

Figure 5: Graph of flow and pressure changes over time, fracture was created at small pressure peak [9]

During the January 2020 test, temperature in the wellbore was measured. To do this, Sentinel Distributed Temperature Sensing (DTS) by Sensornet was used. The DTS system has a temperature resolution lower than 0.01°C, and a spatial resolution of 1 meter [23]. The DTS cable was lowered to the bottom of the open hole section, above where the well collapsed. During the duration of the test, temperature in the well was measured along with pressure and rate.

When looking at the well temperatures for the January 2020 test in figure 6, the time of creation and location of the fracture can be seen. Around a depth of 880 m (only 30 m below casing shoe), a temperature unconformity is visible from the estimated time of fracture creation onward with temperatures in the mid-20s in direct contact with temperatures in high-30s. This unconformity shows where the cold injected fluid is being lost to the formation instead of making contact with the deeper, warmer fluid with the fracture providing the channel for the fluid losses.

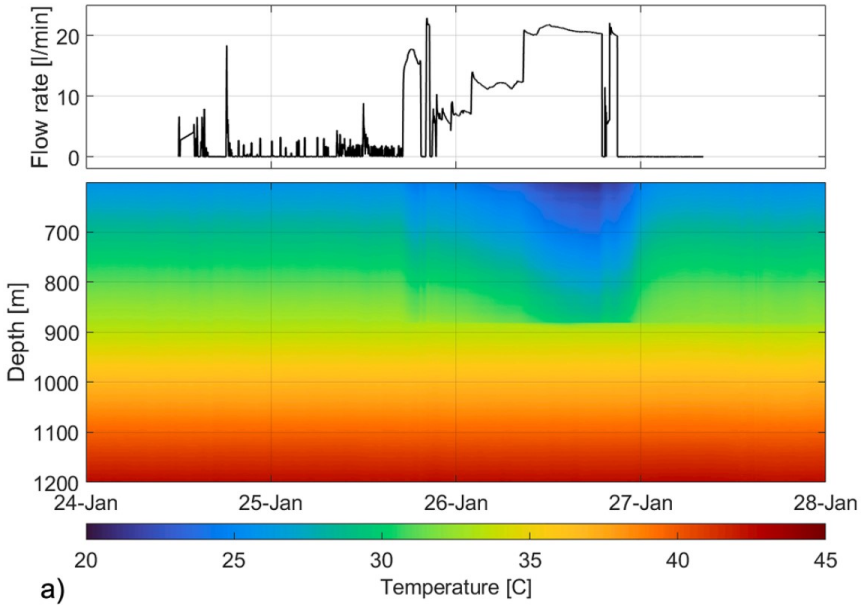

Figure 6: DTS measurement test January 2020
[9]

4.2 August-September 2020 Injection Test

In August and September of 2020 a second injection test based on the results of the first test was performed. This test consisted of three stages, the first of which was designed to understand the fracture's condition at the time of the experiment. Water was injected at an extremely low rate of 2 l/min. During this first stage, the pressure stabilized at 5 bar [9]. This confirmed that the fracture created in the January 2020 test remained at least partially open as during constant injection, pressure remained well below the previous opening pressure of 40 bar and remained stable over the course of the injection.

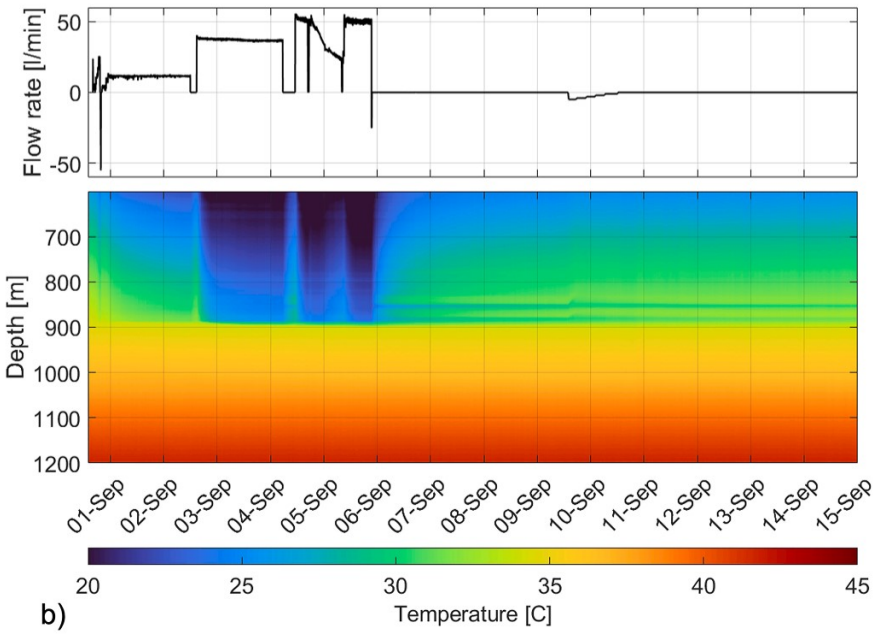

Figure 7: DTS measurement test September 2020
[9]

Confirmation of the fracture's condition was followed by a short second test that included short-term stepwise

injection periods to assess injectivity of the wellbore. Over the course of three and a half hours, injection occurred until pressure stabilized where the rate would then be increased [9]. This was performed for seven rates and the pressure rate plot can be seen in Figure 8.

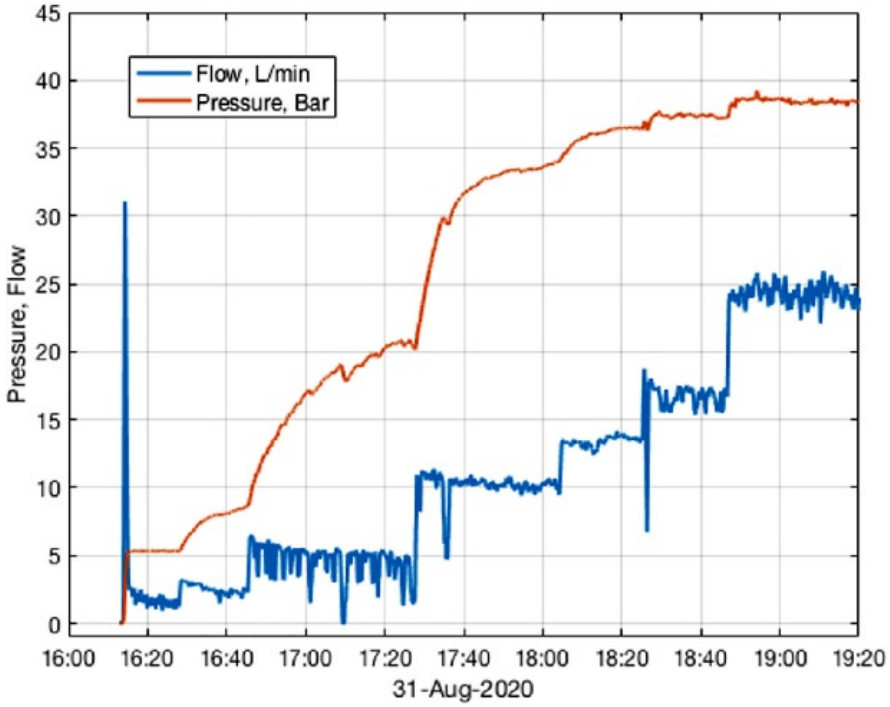

Figure 8: Second stage of August-September 2020 injection test
[9]

The main stage of the test was the third and final stage of the experiment. It consisted of three long-term periods of injection at constant rates with rate increasing every period. Between each stage, the well was allowed to bleed pressure and pressure was recorded for future analysis. Similar to the January test, DTS was used to measure wellbore temperature during injection. Results can be seen in Figure 7. Again, there is a temperature disconformity at the fracture depth. Even with higher injection rates and deeper penetration of lower temperatures when compared to the January test, the fracture acts as a thief and takes all injected fluid. No temperature changes are seen below 880 m depth. It should be noted that in the third injection period, pump instability caused a decrease in rate which can be seen in the rate plot of Figure 7 as well as in the temperature plot in the form of less penetration of cold fluids in the wellbore.

4.3 Injection Test Conclusions

During and after both tests, no induced seismicity was recorded. No seismic activity was monitored at the time and location the fracture occurred, although this might be masked by ambient background noise created by traffic and nearby train lines. This lack of measured seismicity made it difficult to estimate the location and length of the fracture.

As mentioned previously, the well was allowed to bleed pressure after each of three injection stages. The pressure data collected between each injection test was later used to calculate and estimate formation and fracture properties including fracture half-length and fracture conductivity. These results will referenced in-depth and compared to the results gathered in the 2023 test in the "Downhole Measurements" section, but half-length is estimated to exceed 100 m with the best estimation being 130 m and the fracture has a finite conductivity.

During an acoustic borehole televiewer log (BHTV) measurement several months before the creation of the fracture in January of 2020, two steep fractures were noted. These fractures were sealed and not conductive prior to fluid injection. The fractures were located at 880.5 m and 890 m, both are similar to the abrupt temperature change in Figures 6 and 7, but the shallower of the fractures is assumed to be the one that was opened during

injection as it more closely fits the DTS data.

The fracture was likely created as a result of shearing rather than tensile failure as it remained open for seven months between tests. In the case of a shear fracture, the roughness of the rock keeps the rock from closing cleanly or sliding back to its original position. This causes it to stay open for extended periods of time. A tensile failure fracture would close when the applied stress is smaller than the closure stress, σ_3, and would require the same amount of stress in order to reopen, which the results from the injection test in September 2020 contradicts.

The hydraulic head in the LT1 borehole was measured over time and compared to the hydraulic head in another borehole, SH-13 as seen in Figure 9. The changes over time are quite similar to each other, indicating that they are likely connected to the same permeable zone. The SH-13 borehole is located in a Cenomanian aquifer, which is approximately 690 m above the created fracture in the LT1 borehole. This would mean that either the half-length is larger than calculated and propagates upwards or the fracture cuts through a permeable Carboniferous zone that is hydraulically connected to the Cenomanian aquifer.

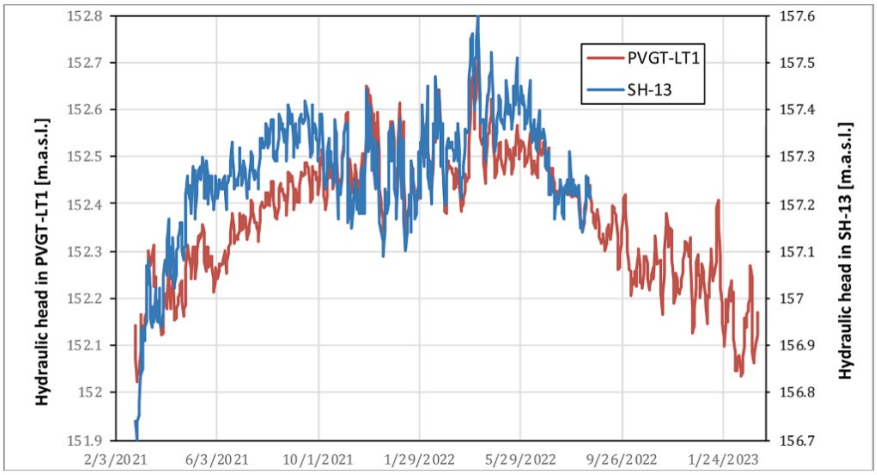

Figure 9: Hydraulic head in LT1 borehole and SH-13
[9]

In addition to the fracture, it is suspected that there is also a cavity present beneath the casing shoe but above the fracture. In Figure 10, the temperature response at the depth of the fracture can be seen, as well as a temperature anomaly. This anomaly is thought to be caused by a cavity rather than a second fracture due to the difference in temperature response. The response of an ellipsoid was modeled and compared to the measurements, resulting in a similar effect. Looking back to the results from the DTS results from the September 2020 test, the effect of this potential cavity can be noticed by the temperature anomaly which occurs as a second, slightly colder horizontal band around 850 m.

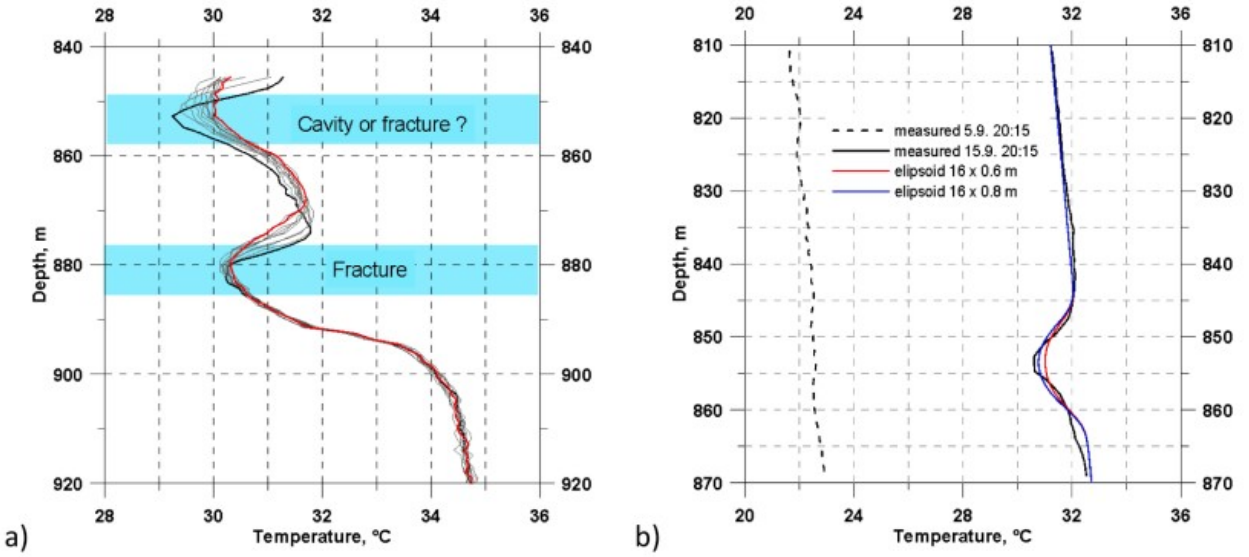

Figure 10: Temperature anomalies in borehole during water backflow, black and red curves from tests on Sept. 9th 2020

[9]

5 Downhole measurements

5.1 Slug test

The August-September injection test in 2020 was performed to determine if the fracture created in the January 2020 injection test was still open and permeable and to analyze its properties through the use of long term injection. Three years later, a third test was designed to again evaluate the fracture condition and properties. This test, referred to as a "slug test", was performed to answer the following questions: was the fracture still open and permeable, was the fracture connected to a shallow aquifer, and what is the half-length of the fracture. The second and third questions were dependent on the fracture remaining open three years after its formation.

As seen in Figure 9, the hydraulic head of the PVGT-LT1 well changed after the creation of the fracture. Prior to the January 2020 test, the hydraulic head of the well was $\sim$ 8.1 m above the the surface. After the second injection test in September of 2020, the hydraulic head was $\sim$ 21.1 m below the surface. The third injection test was designed to fill the well with water to the surface (adding a slug of water) and recording water level change as well as temperature in the wellbore.

5.2 Methodology

To begin the test, the initial water level was measured and water from the nearby Elbe river was poured into the well until the water level was raised to the top of the well head. Figure 11 shows the hose in the well that transferred the water from the water tank to the well. Prior to the addition of the water, three measurement devices were inserted into the well. These were the DTS cable, the levelogger water level measuring device [26], and a seismic device attached to the green cable in Figure 11. The DTS cable was lowered to 1700m depth in the well, just above the collapsed section. The levelogger device was lowered via a steel cable to a depth of 23.8 m below the wellhead.

Figure 11: Well is being filled with river water from tank

In addition to automatic measuring devices used in the test, the water level was manually recorded for a period. This was done to monitor decline during the test as the levelogger data was unavailable until after the completion of the test. For the first hour after injection, the water level was recorded every 10 minutes using a measuring tape with a sensor attached to the end. When the sensor touched water, it would make a noise, and the water level would be read off of the tape measure. During the second hour, no manual measurements were made. After two hours had elapsed, manual measurements were again recorded every 10 minutes for a period of one hour. No measurements were manually recorded the second day. During both the third and fourth days, two measurements were recorded per day at no specific times.

5.3 Water Level Results

The first results analyzed were the manual measurements as they were available for analysis immediately after being recorded. Figure 12 shows the manual data points and a logarithmic fitted curve. The early measurements fit this decline very well, but points recorded days later do not. This was initially thought to be because of either low precision when measuring water levels further from the surface, or from late time water level drop behaving differently from the initial decline. However, the manual measurements served their purpose and were effective in quickly providing an initial understanding of the behavior of the well.

The higher quality data came from the levelogger days after the completion of the test. The levelogger data can be seen in Figure 13. Because water level data was collected 13 minutes before the well was filled, the filling of the well can be seen on the plot. The manually measured data is overlaid with the levelogger data in Figure 13. When comparing the data, it can be assumed that the manual measurements taken the first day of the test were of high quality while the measurements taken days later at deeper depths are of lower quality as they do not fit either the logarithmic projection or the levelogger data.

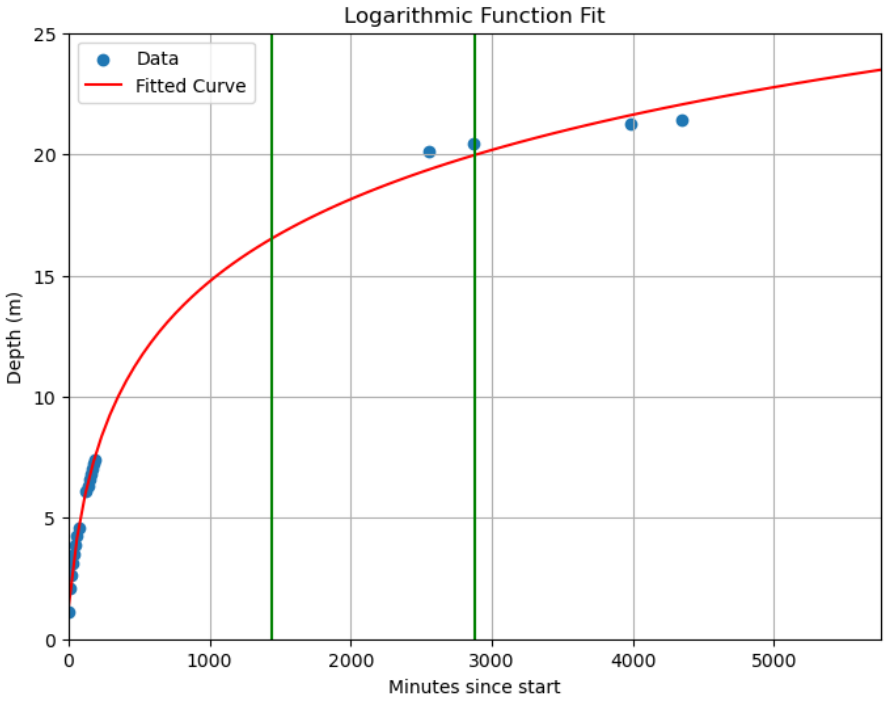

Figure 12: Manual water level measurements

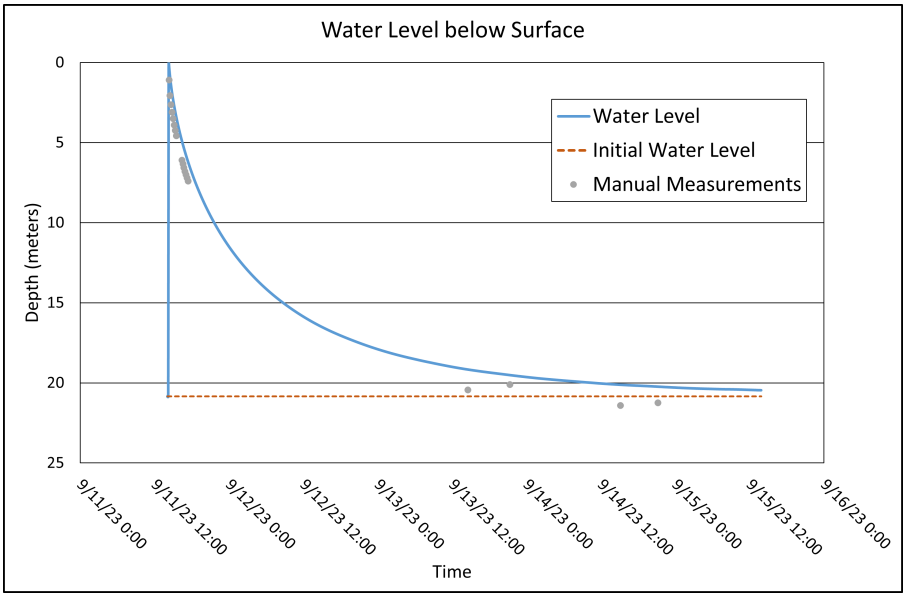

Figure 13: Water level over the course of the test with measurements from the levelogger and manual measurements

There are not many conclusions that can be made from the raw water level data as the number of data points is low outside of the first day. What can be said is that at the end of the experiment, the water level of the well decreased to just above the initial value. Additionally, although this data alone cannot confirm the condition of the fracture, it does suggest that the fracture is open. Fluid from the well was lost to the formation, and based on all previous knowledge of the well, the fracture is the most likely channel for additional fluid to exit the wellbore. More information on the fracture can be gathered by analyzing the DTS measurements, or by further analyzing the water level data using specific techniques.

5.4 DTS Results

As mentioned previously, borehole temperature was measured during the 2023 slug test using DTS. Figure 14 shows the DTS measurements in the first 35 m of the borehole, as below 30 m there was no noticeable temperature change. Figure 14 also shows the water level in the well. This is important, because it shows that the majority of the temperature changes located in the the first 5 m take place in air and are due to diurnal cycles. Soon after injection, the penetration of warm water can be seen. Water temperatures at these depths return to normal within $\sim$ 20 hours of the injection with the deepest depth of warm water moving upwards over time until the top of the water column was reached. It should noted that the DTS tool recorded measurements every 30 minutes while the water level was recorded every minute. This explains why the appearance of warm water at depth in the well occurs well after the slug was injected rather than immediately after.

The DTS measurements recorded in the slug test are unfortunately not effective in assessing the condition of the fracture or the heat properties of relevant formations. The injected water did not penetrate deep enough into the well to see responses from these targets. What can be concluded is that in the well, diurnal cycles do not have an effect on temperature below 5 m. In a BTES well, understanding how these fluctuations in near-surface temperature will effect temperatures below 5 m will be important. However to test how diurnal cycles effect BTES wells, the borehole(s) being tested must have a hydraulic head near the surface or above the surface. If additional data is desired related to the fracture located in this well, a new injection test would be needed that included higher rates of injection for longer periods of time to ensure that the injected water reached deeper depths.

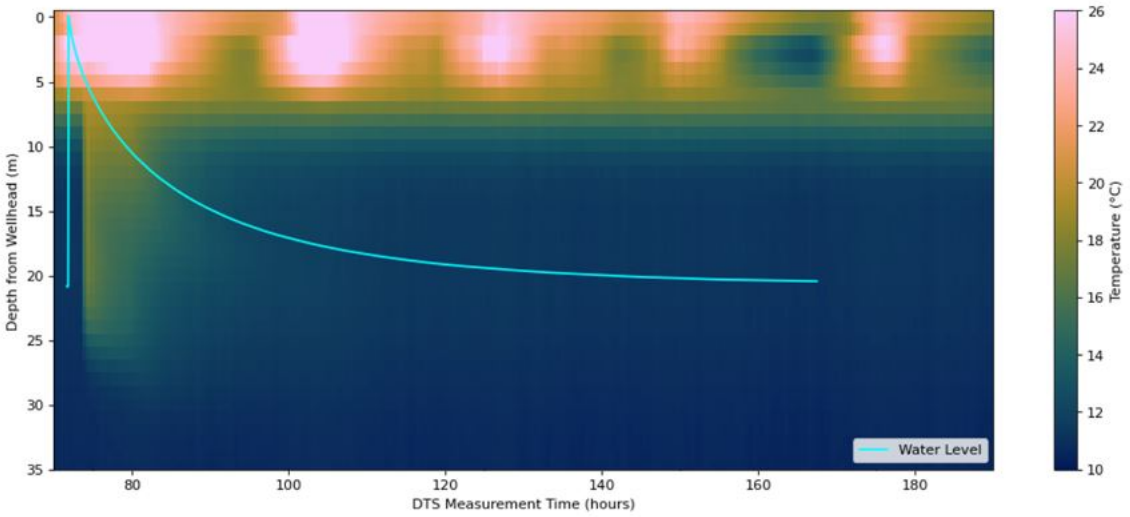

Figure 14: 2023 slug test DTS measurements with water level over time

5.5 Well Testing Analysis

In addition to providing only the water level decline, the slug test measurements were used to further analyze the behavior of the fracture. The water level measurements recorded using the levelogger were used as the basis to analyze the well using conventional well testing techniques. Well testing is a branch of reservoir engineering with the objectives of characterizing target formations and evaluating and predicting well performance [20]. Well testing analysis was used to analyze the data from the August-September 2020 injection tests. By analyzing the 2023 slug test, the results can be compared to the 2020 conclusions.

The general methodology of well testing is simple. A change in the well or in the reservoir is induced. This is generally a change in production or injection rate. The response from the reservoir (changes in pressure, rate, or both) is then measured and recorded. These changes are then compared to known responses that are based off of the governing flow equation (diffusion equation) [20]. By comparing it to known solutions, the condition of the tested well or reservoir can be determined. The most common target variable is permeability, but skin factor (a parameter that quantifies damage done to the reservoir by the well) and fracture parameters such as conductivity, half-length, and width are also able to be calculated.

5.5.1 Pressure Change and Pressure Derivative

In the slug test, like most well tests, the pressure response over time is an important measurable variable. However in the various analysis techniques, the actual pressure is not important when compared to the pressure change and pressure derivative at each time step. Because change is the key variable, it was possible to use the water level and hydrostatic pressure from the water column in the wellbore to find this pressure change. Pressure at the fracture was calculated using the estimated depth of 880 m below the surface along with the changing water level in well, but any point in the well that was never above the water level would have been sufficient. Figure 15 shows the pressure at fracture depth over time. It is very similar to Figure 13 as the pressure at the fracture is purely hydrostatic assuming a water density of 1.011 kg/L throughout the wellbore [9].

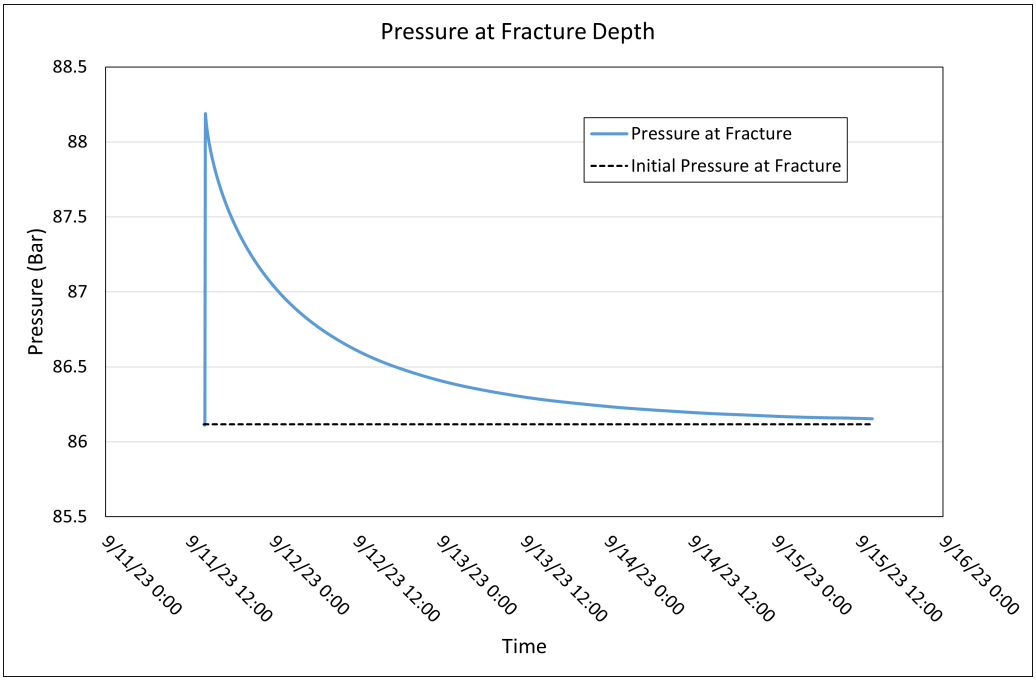

Figure 15: Calculated pressure at fracture depth over time

Calculating pressure change and pressure derivative are simple. Pressure change is the difference in pressures values at a time and the time step prior. The formula for pressure derivative can be seen in Figure 16 with the subscripts "1" and "2" representing the points directly before and after the target time step. The pressure derivative magnifies small changes and noise more than the raw pressure change data [20]. To ensure smooth derivatives, Bourdet et al. created a parameter, L in Figure 17, and suggested it remain between 0 and 0.5 with values generally around 0.1. "L" was calculated for the duration of the test data. Figure 18 shows the L values over the course of the 2023 slug test. The first time point is above the recommended 0.5 threshold, but this is acceptable as it is the first point.

$$\frac{dp}{dx} = \frac{\left(\frac{\Delta p}{\Delta x}\right)_1 \Delta x_2 + \left(\frac{\Delta p}{\Delta x}\right)_2 \Delta x_1}{\Delta x_1 + \Delta x_2}$$

Figure 16: Pressure derivative equation
[4]

$$\ln \frac{t_{i+1}}{t_i} \text{ and } \ln \frac{t_i}{t_{i-1}} \geq L$$

Figure 17: Bourdet et al. L variable formula
[4]

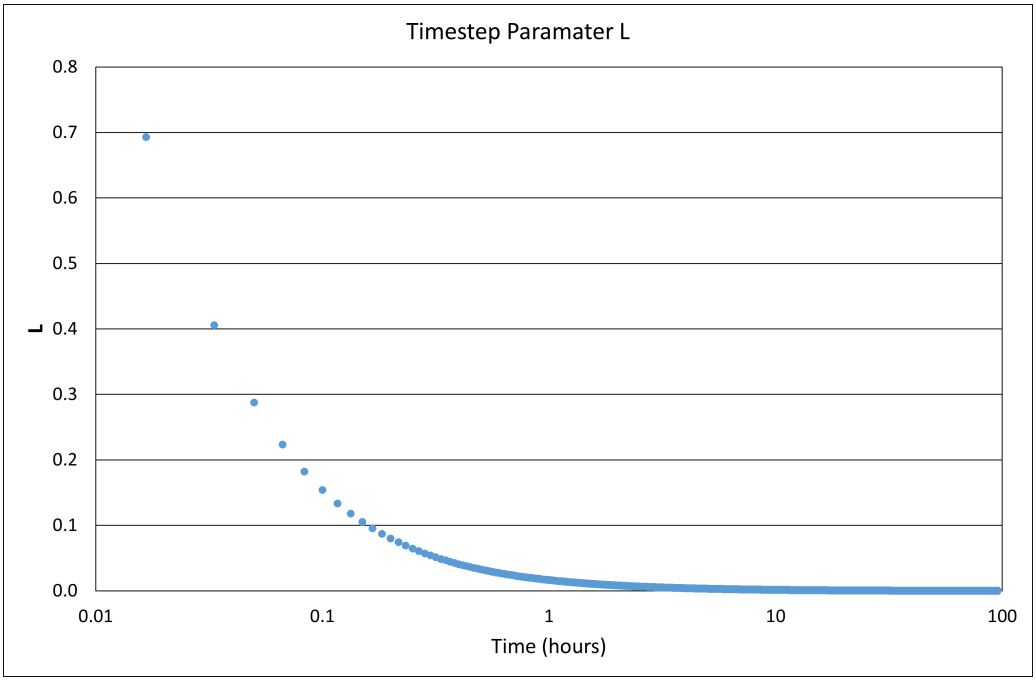

Figure 18: Bourdet et al. L variable for 2023 slug test

Figure 18 is concerning as the L values quickly approach 0 and are well below the recommended value of 0.1. This is acceptable to proceed further with the analysis, but suggests that the time steps are very small and that noise will be magnified. This can be seen in the late time, large noise seen in the pressure derivative in Figure 19. For the purpose of this analysis, hand calculations are sufficient and complex software is not required. As the general trend and shape of the derivative curve is visible amongst the noise, the data functions as normal. However, if more complex calculations were to be performed on the derivative data, the noise would make those calculations, that require smooth curves, impossible.

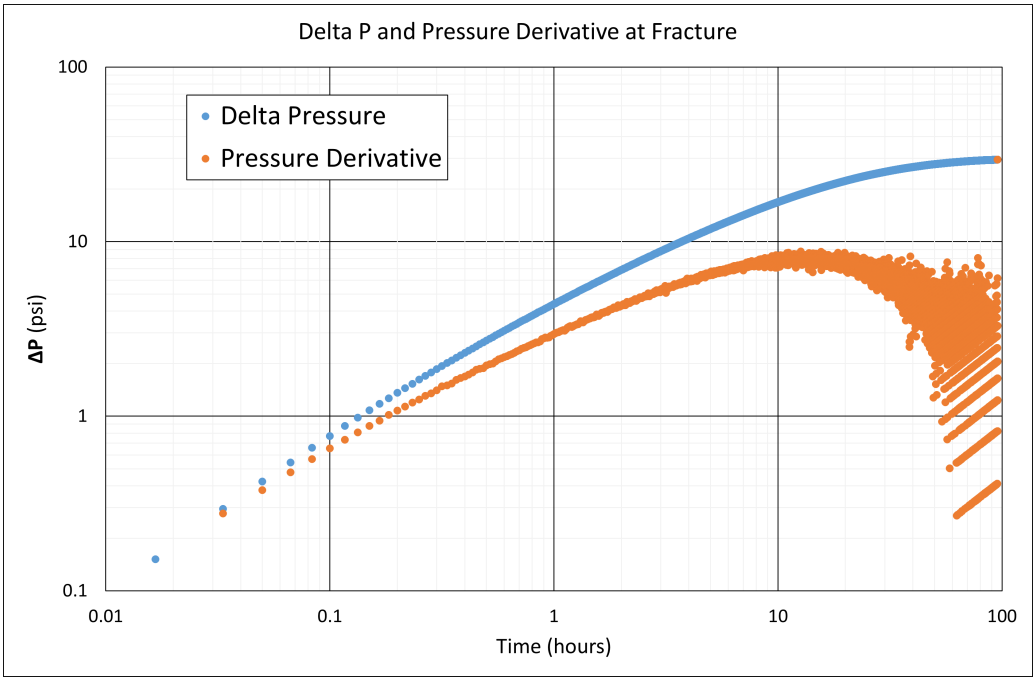

Figure 19: Combined plot of pressure change and pressure derivative on a log-log plot

5.5.2 Common Techniques

Two manual analysis techniques were used to interpret the slug test data. These techniques, straight-line analysis and type curve matching, are the two most common techniques used in well testing. There are computerized techniques that utilize regression analysis to fit synthetic response to the measured data, but these techniques often require the use of niche software packages that were not available for this project. One such software is Kappa Engineering's Saphir Pressure Transient Analysis software [16].

Theoretical models show that certain straight line relationships exist when pressure change is plotted against time on specific coordinates [20]. These coordinates are commonly unchanged time, log of time, fourth root of time, or square root of time, but depend on the type of flow occurring in the reservoir (flow regime). When the straight line sections are measured for their slope, the slopes are directly related to target properties as functions of those properties. Different time coordinates/flow regimes are related to different properties. For example, all flow regimes include permeability in their slope formulas, but only the slope of bilinear flow in fractures can give insight to fracture width and fracture permeability. Linear flow in a fractured well cannot give insight into fracture width, but its slope does does include fracture half-length, or the distance from the tip of the fracture to the well. To utilize straight-line analysis, it is important to understand flow regimes during the test. It is possible to determine flow regimes with different straight line plots where pressure change and time are both plotted on a log scale.

Type curve analysis also utilizes general solutions and theoretical models in the form of type curves to characterize the measured reservoir responses. These general solutions are in the form of dimensionless variables. Figure 20 shows example formulas for dimensionless pressure and time in oilfield units, the most common well testing units. All analysis in this report was done using oilfield units and later converted to metric units for target parameters. When the dimensionless variables are plotted on a log-log plot, they should have the same shape as the measured response data of pressure change and time also plotted on a log-log plot. Based on how the type curve is shifted laterally or vertically to fit the measured data, reservoir properties can be determined. Once the curves are adjusted to fit, any point on the figures can be chosen. As both curves are on log-log scales of the same size, any point chosen on the plot will give the same ratio. It is critical that the log cycles of both plots are the same size to prevent distortion. Figure 21 shows how the ratios of the dimensionless and measured pressure and time points can be used to estimate permeability.

$$p_D = \frac{kh}{141.2qB\mu}\Delta p$$

$$t_D = \frac{2.637\times10^{-4}k}{\phi c_t \mu r_w^2}t$$

Figure 20: Example formula for dimensionless pressure and time
[20]

$$\left(\frac{p_D}{\Delta p}\right)_M = \frac{kh}{141.2qB\mu} \qquad \left(\frac{t_D/r_D^2}{t}\right)_M = \frac{2.637\times10^{-4}k}{\phi c_t \mu r^2}$$

Figure 21: Formulas for matched dimensionless and measured pressure and time
[20]

5.5.3 Flow Regimes

In both techniques, flow regimes are critical to consider. In straight-line analysis, flow regimes can be identified and they dictates which straight-line plots are viable for property calculation. In type curve analysis, the type curve used will change based on the flow regime. In a fractured well there are five effective flow periods and four flow regimes. The first main flow period is wellbore storage. In this stage, the fluid entering the reservoir is not the injected fluid, but additional fluid stored in the annulus of the well or a nearby cavity in an open hole section. In the PVGT-LT1 well, this could come from the cavity at a depth of 850 m. This period can vary in length depending on the conditions of the test and the condition of the well. After the wellbore storage period, the standard flow regimes occur.

The four flow regimes of fractured wells in order of occurrence can be seen in Figure 22. In most well tests, linear flow in fractures occurs at the beginning of a test in the first few seconds. Because of this, it is not measurable [20]. However, in fractures through very low permeability rock, this period may be longer if flow rates are very low. In this linear flow in the fracture, fluid in the fracture is either produced, or injected further into the reservoir. In bilinear flow, production from the fracture continues, but some fluid from the reservoir is also produced. It enters the fracture perpendicular to the propagation of the fracture [20]. In linear flow in the reservoir, production comes entirely from the reservoir. The final flow regime, pseudoradial flow, is present in all wells at late time. Production comes from the reservoir and the flow converges to the well in a radial fashion. When in the vicinity of the fracture, the flow converges in a ellipsoidal shape which then evolves into linear flow at the surface of the fracture [20].

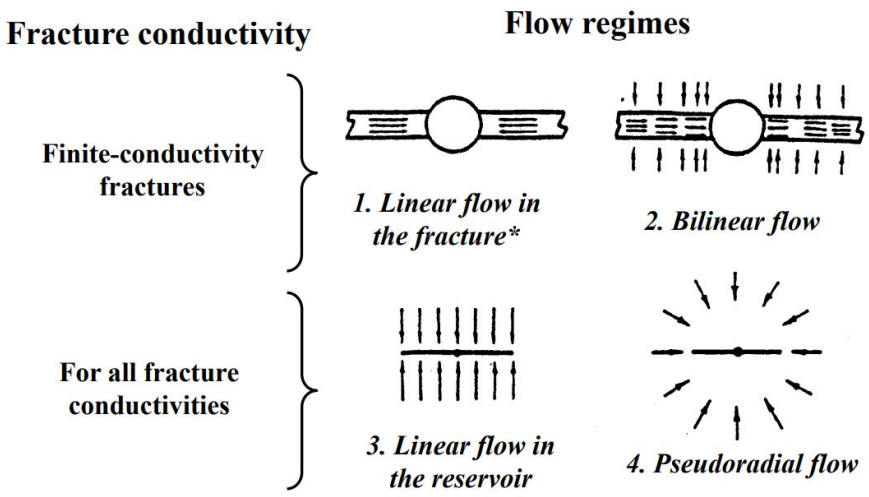

Figure 22: Fractured well flow regimes in order of occurrence [20]

5.5.4 Straight-line Analysis

The first step of straight line analysis is to identify flow regimes. This is done with the use of a log-log diagnostic plot of pressure change and pressure derivative vs time. This is the plot shown in Figure 19. Generally, the straight-line slope can be measured from either the pressure change or the pressure derivative as they are very similar. In our data, this is not the case. The linear section of the pressure derivative has a slope of 0.707 and the linear section of the pressure change has a slope of 0.879. In these scenarios, it is correct to use the value from the pressure change curve [4].

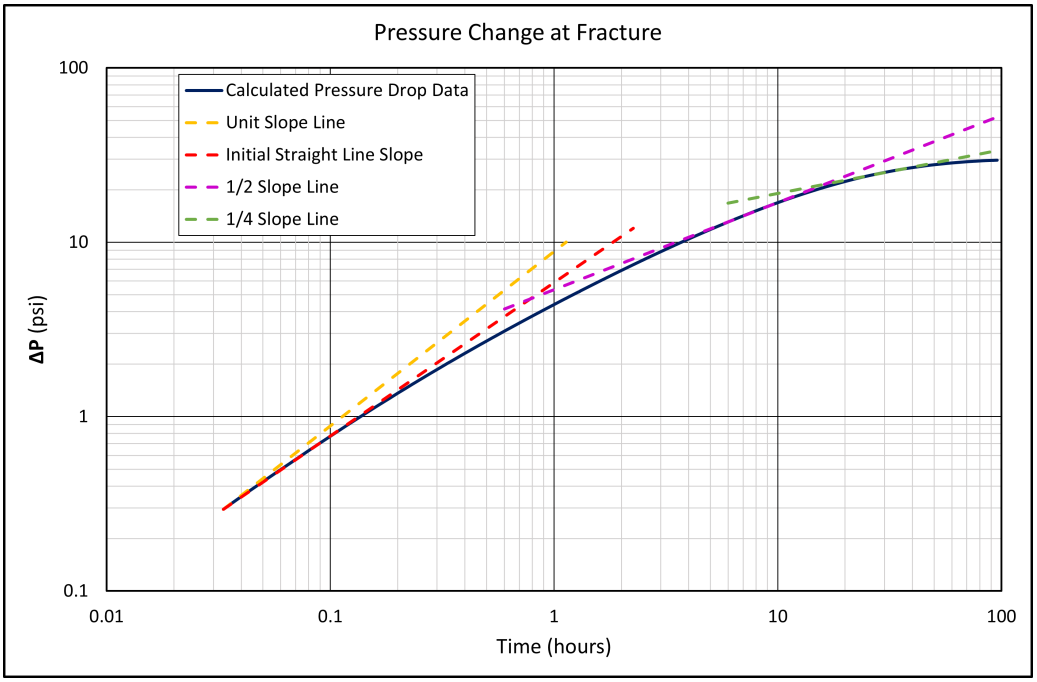

Figure 23: Log-log plot of pressure change with flow regime straight line guidelines

Figure 23 shows the pressure change data on a log log plot similar to Figure 19 but with identifiers slowing the initial straight-line slope and straight-line sections corresponding to the target flow regimes. The initial slope is nearest to the unit slope line of wellbore storage. After this period, the pressure drop curve indicates that both linear flow and bilinear flow occurred. Although this is rare and/or unlikely in this order (bilinear after linear), straight-line analysis can be performed using both regimes. It should be noted that radial flow exists on Figure 23, but is for such a short period at the very end time of the test that it is not shown on the figure.

Generally, the existence of additional fluid in an annulus leads to wellbore storage effects. However in the PVGT-LT1 well, there is no such annulus. There is additional fluid however. If the fracture itself can be considered as a pseudo annulus, the fluid in the fracture can be considered additional fluid. The water level of the well returned to the original level by the end of the test. This means that the amount of water injected into the well is equal to the volume lost to the reservoir. This volume was 429.48 liters. The fracture volume is considerably larger, meaning that the fluid lost to the reservoir was initially entirely within the fracture.

The origin of this fluid within the fracture had influence on the pressure drop curve, shifting its slope more towards unit slope, but as the fracture was a store of fluid within the reservoir and was itself the connection between the reservoir and the well, other flow regimes were able to occur. Figure 23 suggests this as pressure change declines over the course of the test.

The first flow regime to analyze is pseudoradial flow. Although it is the last regime to occur in a flowing well, it is often best to perform analyze this regime first. This is because the relationship between the pseudoradial straight-line slope and reservoir parameters only includes one unknown variable, permeability (k). The straight-line slopes of linear and bilinear flow can be related to permeability and one other parameter each. As permeability is a rock property and does not change over time, the order of analysis does not matter. By finding permeability first, the additional parameters, fracture half-length and fracture conductivity, can be found using the calculated permeability.

For pseudoradial flow, straight-line analysis is performed when pressure change is plotted against the log of time. This is very similar to the diagnostic log-log plot, but in this case, pressure change is on a Cartesian axis. Figure 24 shows the semi-log plot for pseudoradial flow. As pseudoradial flow occurs at the end of the test, the straight line section must be measured at the same time. The slope visible in Figure 24 is the log slope. Because of the semi-log nature of this plot, the slope must be converted to Cartesian slope to be used in the formula. To do this, the measured value of 1.2784 is multiplied by the natural log of 10. This results in a Cartesian slope of 2.9436. This value was then used in the straight-line analysis equation.

Figure 25 shows the equation for semi-log pseudoradial flow straight-line analysis. In this formula, m_{pr} is the Cartesian slope found from straight-line analysis, 'q' is injection rate, 'B' is a formation volume factor that for water is always 1, 'μ' is viscosity which was calculated using the DTS measurement of the water temperature and was 0.00074 Pa*s (0.74 cp), 'k' is the target parameter permeability, and 'h' is pay zone height, or the height of the unit. In this formula, imperial well testing units are used, so a conversion factor is included.

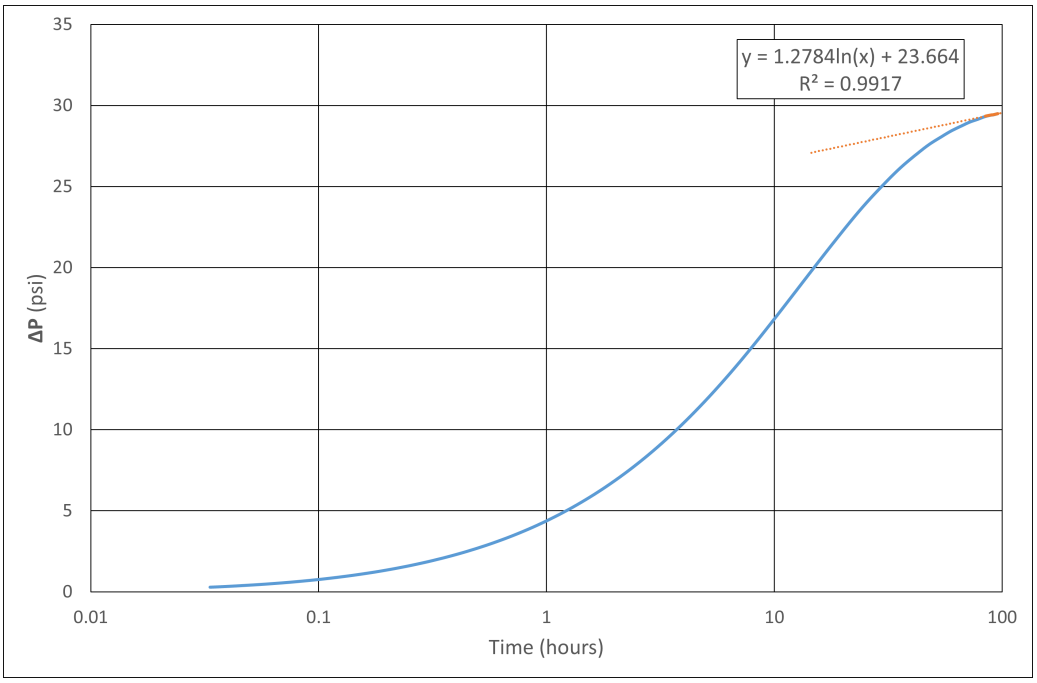

Figure 24: Semi-log plot for pseudoradial flow analysis

$$\left|m_{pr}\right| = \frac{162.6qB\mu}{kh}$$

Figure 25: Pseudoradial slope equation
[20]

Injection rate, q, and pay zone height, h, are uncertain parameters. For rate, a range of possible values was created with the minimum (20 l/min) being based on previous tests and the maximum (100 l/min) being based on the volume of water added to the well and the injection period for this 2023 test. As injection only measured indirectly via water level and because injection occurred for a very short time period, a wide range was used. For pay zone height, the range of values from the Fischer et al. paper of 20 m to 100 m was used [9]. For both variables, 81 values ranging from 20 to 100 (increments of 1) were used to analyze how different combinations of rate and pay zone height affected permeability. All values of both rate and pay zone height are assumed to be equally likely in terms of occurrence. Figure 26 shows the 6561 combinations of rate and height and their resulting permeabilities. Values ranged 22-562 md with an average of 137 md. Fischer et al. had their own uncertainty for permeability, but their values ranged from 0.385-1.925 md [9].This is a substantial difference in results. However, it is believed that these values of permeability measure different subsurface features. The permeability measurements from Fischer et al. measure the permeability of the rhyolite ignimbrite matrix through which the fracture was created. The values found in the 2023 slug test are most likely an effective permeability that includes both the ignimbrite matrix as well as the fracture. A shear fracture through a relatively impermeable matrix that is hydraulically connected to a more permeable unit would give values within the range found, especially if the fracture was narrow in aperture.

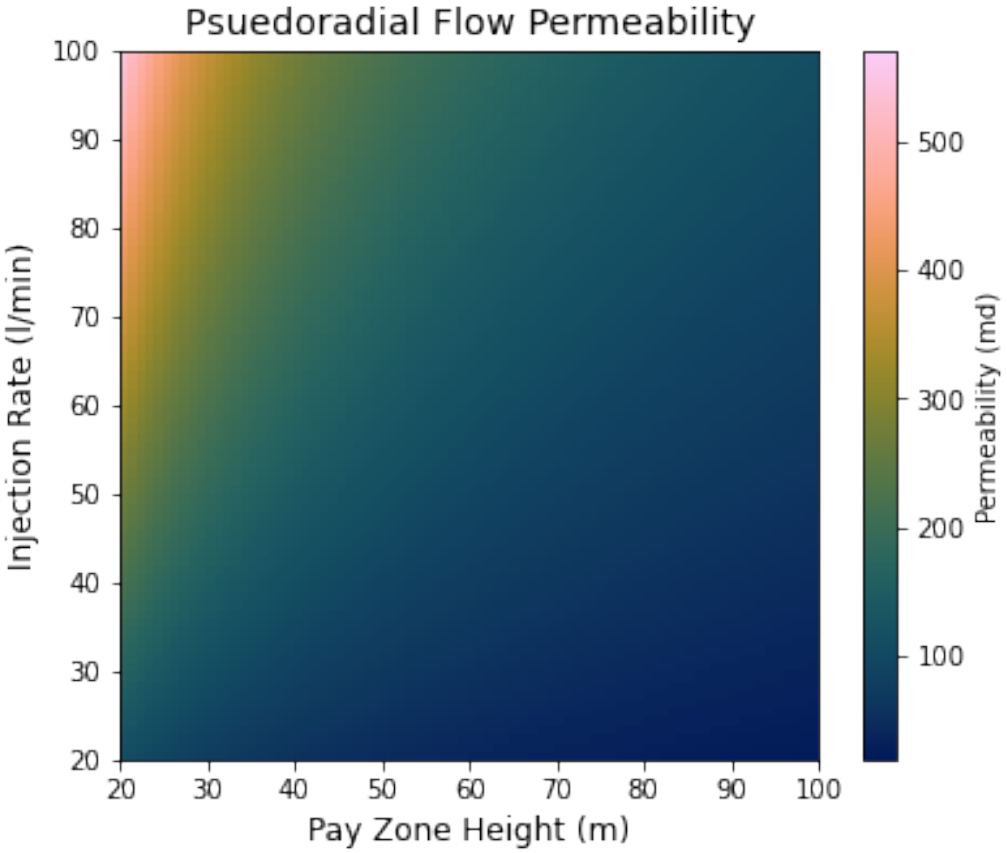

Figure 26: Calculated permeability for ranges of rate and height uncertainty

For the remaining flow regimes, the order of analysis does not have an effect on the target parameter calculations as both fracture half-length (linear) and fracture conductivity (bilinear) are rock properties and do not change over the time of the test. However as linear flow, or a linear transition phase, occurred prior to bilinear flow, fracture half-length will be discussed first. Figure 27 shows the straight-line analysis for linear flow. In this plot, pressure drop is plotted against the square root of time with both axes being Cartesian. Although the straight line section appears to be measured during the initial period of the test, the straight-line period of Figure 27 is the same as identified in Figure 23.

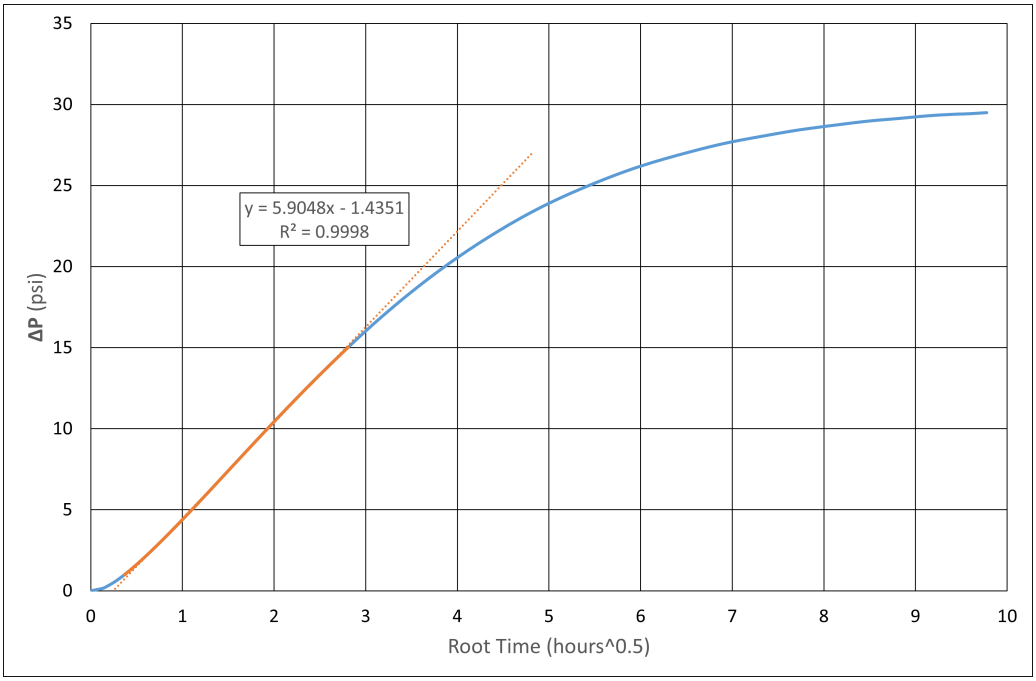

Figure 27: Square root time Cartesian plot for linear flow analysis

Figure 28 shows the formula for the the slope of the straight-line section of the linear flow plot. In this equation, the additional variables are the target variable fracture half-length (x_f), porosity (ϕ), total compressibility (c_t) which is the compressibility of both the rock and fluid combined, and a constant 'C' that is dependent on the time units used on the x axis of the plot (hours or days). Porosity was estimated to be 0.1 [9] and total compressibility was assumed to be 0.145 1/GPa, a reasonable estimate for porous units that are generally less compressible. As the units used are in hours and not days, 'C' is 4.06 and not 19.91. Again, this formula is in imperial oil field units and results in a half-length in feet which is then converted to meters. For calculating half-lengths, the uncertainty related to rate and pay zone height still remains in addition to the range of permeability values calculated. Figure 29 shows the range of half-lengths calculated based on the rate and height uncertainty. The lengths range from 69-331 m with an average of 156 m. These values are in line with those estimated from the previous test of over 100 m but likely near 130 m [9].

$$m_l = \frac{CqB}{x_f h}\sqrt{\frac{\mu}{k\phi c_t}}$$

Figure 28: Linear slope equation
[20]

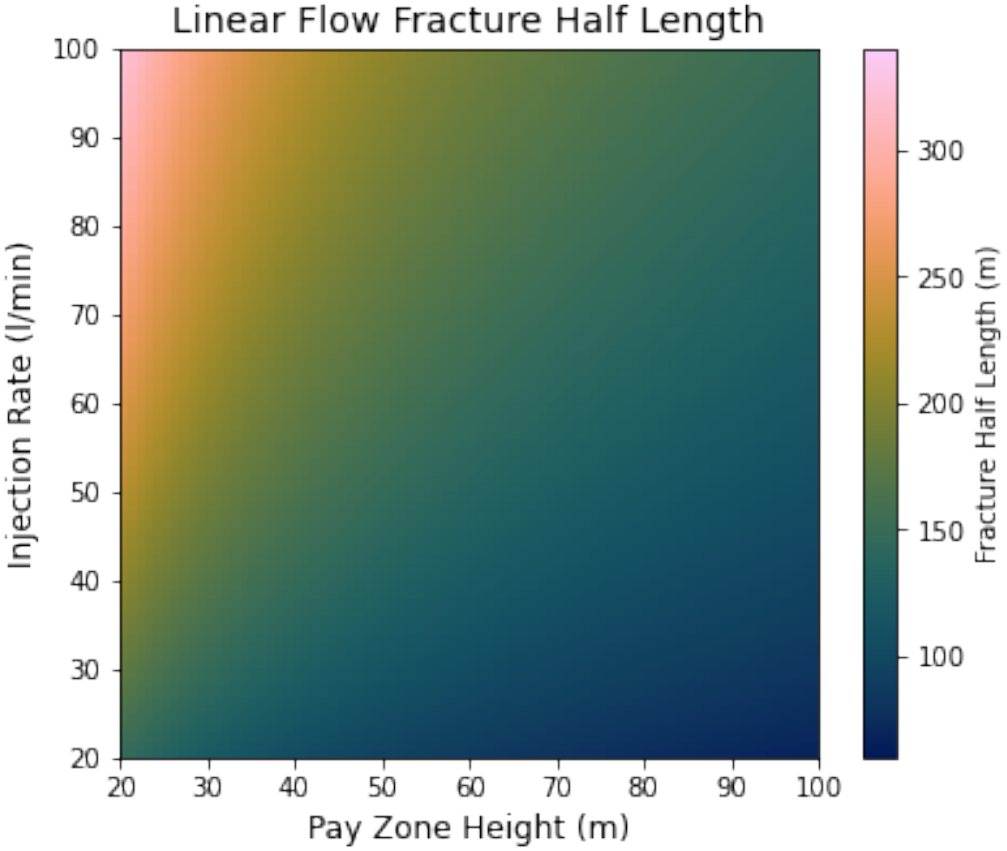

Figure 29: Calculated half-length for ranges of rate and height uncertainty

The linear flow plot can also give insight to damage in the well. In Figure 27, the y-intercept is related to the apparent skin, or mechanical damage to the well. Figure 30 shows the formula used to find apparent skin with $\Delta p_{skin,app}$ being the value of the y-intercept. Although apparent skin is a function of pay zone height, rate, and permeability which are all uncertain variables, permeability is itself a function of height and rate as it is calculated using Figure 25. Because of this, the specific values of rate, height, and permeability used to calculate apparent skin do not matter as all give the same value of -0.561. Because skin is negative, the 'mechanical damage' done to the reservoir is negative. This means flow is enhanced which is to be expected in a well with at fracture that is more conductive than the matrix.

$$\frac{141.2qB\mu}{kh} S_{app} = \Delta p_{skin,app}$$

Figure 30: Skin equation from linear flow [20]

The final flow regime to analyze is bilinear flow. Figure 31 shows the pressure change plotted against the fourth root of time. The straight line section was found and the slope was used in the equation found in Figure 32. In this formula, the only new variables are k_f and w which are the permeability of the fracture itself and the width of the fracture. The target parameter is the product of these variables, $k_f w$, and is known as fracture conductivity. This is generally preferred as the variables are difficult to find individually, and the product itself is a design parameter for fracturing companies that is important for fracture performance [20]. It should be noted that the constant 'C' is the same as the 'C' in the linear flow formula in Figure 28 in the sense that it depends on time units used, but the actual value of the constant changes from 4.06 to 44.1. The day value of 'C' for bilinear flow is 97.6.

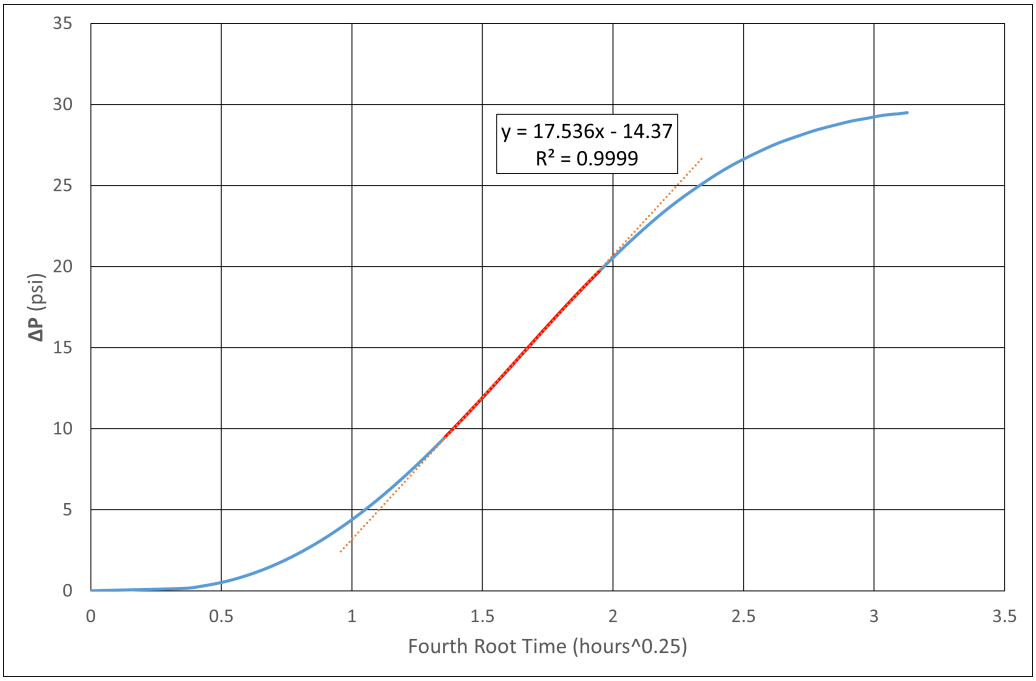

Figure 31: Fourth root time Cartesian plot for bilinear flow analysis

$$m_{bl} = \frac{C\,qB\mu}{h\left(k_f^2 w^2 k\phi\mu\, c_t\right)^{1/4}}$$

Figure 32: Linear slope equation
[20]

Like the other flow regimes, straight-line analysis for bilinear flow is dependent on rate and pay zone height. Figure 33 shows the range of calculated fracture conductivity in a form similar to Figures 26 and 29. Fracture conductivity ranged from 2.457e-13 to 3.071e-11 m^3 with an average of 4.226e-12 m^3. These values are 2-4 magnitudes larger than what was estimated in the 2020 injection tests [9]. This difference is substantial and likely invalidates the bilinear straight-line analysis results. Additionally, the linear section of Figure 31 does not correspond with the time where the Figure 23 diagnostic plot suggested bilinear flow occurred. In that section of time, the fourth root plot is not linear. if a slope were to be measured during this period and used to estimate fracture conductivity, the resulting $k_f w$ would be even larger.

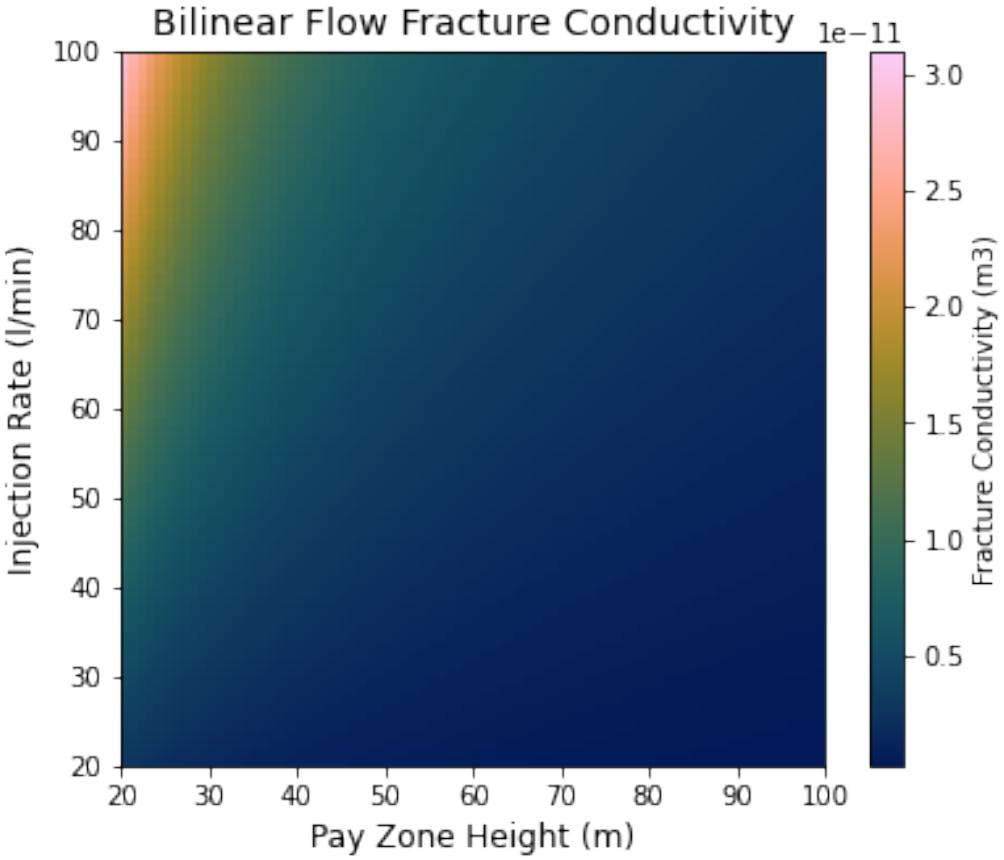

Figure 33: Calculated fracture conductivity for ranges of rate and height uncertainty

5.5.5 Type Curve Matching

No usable results were able to be gained from type curve analysis. The behavior recorded in the pressure change and pressure derivative plots did not match any available type curves. This was due to the lower slope in the initial time periods of Figure 19. In general, type curves have an initial slope of the unit slope for wellbore storage. Because of this, the lower slopes of the pressure change and pressure derivative curves cause the curves to be elongated compared to the type curves. This can be seen in Figure 34 where the shape downwards curves seem to align, but the initial tails differ in slope. The same occurs in the pressure change plot as it too has a slope under unit slope on the log-log plot.

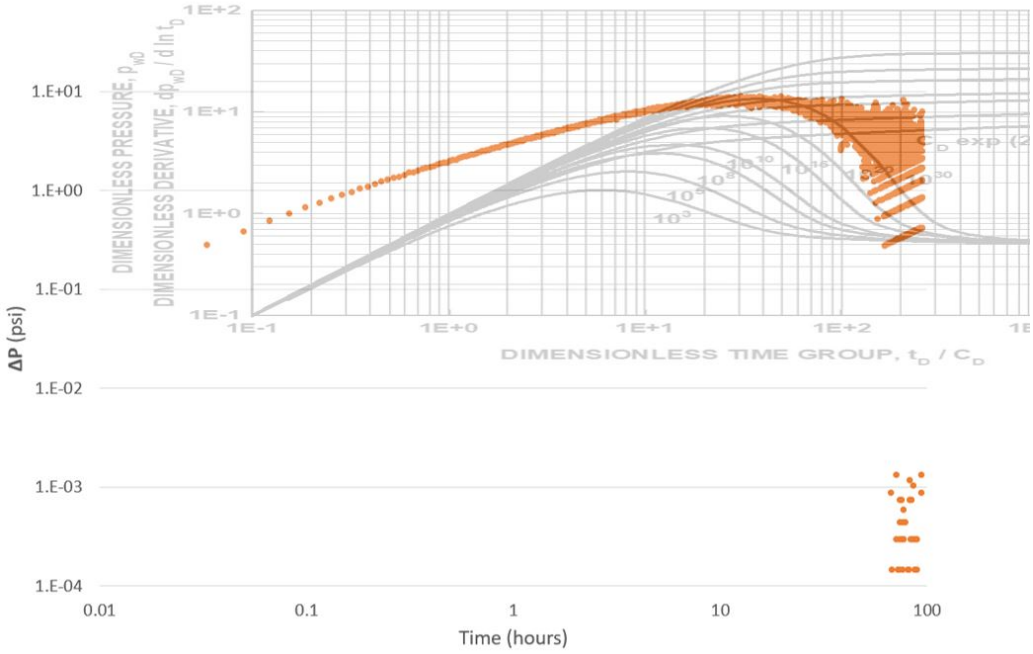

Figure 34: Pressure derivative curve type curve match

The unorthodox nature of this test is likely the reason for a lack of matching with the common type curves. Injection rates were very low, the injection period was very short, and there was little to no penetration of injected fluids into the well. Many of these curves were based on tests of much longer duration with injected fluids reaching well into the reservoir. However, while type curve matching was not successful in producing results in this analysis, the technique could still potentially be used with this dataset. This analysis used available images of curves from textbooks [4] and lecture notes [20]. However, software programs such as Saphir by Kappa [16] contain more type curves as well as the ability to fit curves using numerical methods. It is possible that if such a software was used with this dataset, a solution could be reached.

5.6 Downhole Measurement Conclusions

The 2023 slug test was performed to answer the following three questions: was the fracture still open and permeable, was the fracture connected to a shallow aquifer, and what was the half-length of the fracture. Although the results from both DTS temperature sensing and well testing analysis were not ideal, these questions were still able to be investigated. As previously mentioned, the DTS measurements did not give any information directly related to the main goals of the test, but were used to determine the water temperature at the fracture depth.

For well testing analysis, the results from the slug test had significantly more uncertainty than the well testing analysis results from September of 2020. The uncertainty related to injection rate and pay zone height are not the only concerning aspects of the slug test results. The pressure change and pressure derivative curves resembled standard curves, but were substantially different when considering analysis and looking past the general shape. This is almost certainly due to the unorthodox nature of the test performed. Both the volume added to the well and the rate at which fluid was lost to the fracture were very low. Well testing techniques are well suited for these types of tests.

In this situation, it is unclear if the standard flow regimes of bilinear, linear, and pseudoradial really occurred, or if fluid leaked off via linear flow within the fracture. Linear flow within a fracture is not normally considered, but in this scenario with a low leak-off rate and a relatively impermeable matrix rock, linear flow within the fracture is possible. The well testing analysis results of the 2020 tests suggested that the majority of the test occurred with bilinear flow [9]. With such high rates and confining surface pressure, it is very reasonable that fluid would travel linearly through the fracture, but also linearly from the fracture to the matrix perpendicularly to the fracture. In the slug test, when rates low and confining surface pressure is non-existent, it is reasonable

to conclude that the fluid travelled linearly though the fracture, but lacked the pressure or rate to penetrate the matrix. A pore pressure/wettability experiment using the rhyolite ignimbrite matrix would be beneficial in supporting or dismissing this theory. If the theory of only linear flow within the fracture is correct, the well testing analysis results in this report are of low quality and could be disregarded. If this is not the case, it is likely that the measured well testing results are relevant to some degree. In either case, information about the fracture can be determined to answer the initial questions about the fracture.

Regarding the first question and the current state of the fracture, it is clear that it is still open. The degree to which it is open is unclear, but flow can occur within the fracture. Having effective temperature changes at the fracture depth from the DTS data would have effectively confirmed that the fracture is open, but the well testing analysis strongly suggests that the fracture is still open. Because the fracture is still open to flow, it is also likely a shear fracture, further confirming the conclusion of the August/September 2020 test conclusions.

For the second initial question related to the fracture being connected hydraulically to a different permeable unit or a shallow aquifer, it is very likely that this is the case. Although the fluid loss in the well was very low, the rate at which this occurred was too quick for the rhyolite ignimbrite matrix to have taken all of the fluid. Rather, the fluid was likely transported to a different matrix that is permeable. Without additional hydraulic head data from the SH-13 well shown in Figure 9, it is difficult or impossible to say if the different unit where fluid was transported to was connected to the shallow aquifer or not, but based on past hydraulic head data, it is likely that this is the case.

Regarding the third initial question and the fracture half-length, the 2023 slug test can not certainly provide an answer. The test's ability to be analyzed with conventional well testing techniques is not certain, and the well testing analysis itself gave a range of values. These values are well within the expected range from previous estimates of $\sim$130 meters [9], but were based on permeability values for the system that did not match the previous results. Because of this, no concrete conclusion could be reached for the half-length of the fracture.

The 2023 slug test was unconventional in its approach, and the analysis of the test reflected that. A fourth test that included higher rates at higher pressures for longer periods would be recommended. Such a test would be similar to the 2020 injection tests and would produce higher quality results from DTS measurements and well testing techniques. Fracture condition as well as general subsurface behavior could be better understood 3+ years after the opening of the fracture. Unfortunately, a conventional injection test is no longer possible in the PVGT-LT1 well due to the existence of measuring devices that are sensitive to high pressures. However, such tests can be performed on wells to be drilled in the future.

6 Surface Geophysics

Several geophysical methods were applied in the project in order to gather more lateral information of the underground close to the current and future boreholes. These methods included electrical resistivity tomography, various seismic methods, and the processing of existing gravity data. As other studies have shown [14] results from these different methods complement each other and can be linked to existing (borehole) data on the local geology, as well as cross-correlated with each other. These measurements were conducted along a profile located about 400m east of the PVGT-LT1 borehole. This profile had previously been used for magnetotelluric (MT) measurements that were not used in this report.

6.1 Electrical Resistivity Tomography

6.1.1 Theory

Electrical resistivity tomography was used to gather lateral information on the structures in the shallow subsurface near the PVLT-GT1 borehole. Current electrodes induce a current in the subsurface and the potential electrodes measure the pressure drop caused by the subsurface. From this data, the resistivity distribution of the subsurface can be determined. The array used for the ERT measurements was the gradient array, in which the current electrodes are put on the outside of the array and the potential electrodes in the middle, as depicted in Figure 35.

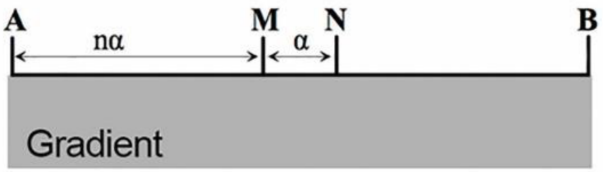

Figure 35: Gradient array configuration [24]

6.1.2 Methodology

First measuring tapes were laid down in a straight line along the location of the profile which can be seen in Figure 36. The exact location was recorded using GPS. Then 120 electrodes were placed into the ground with a spacing of 5 meters, resulting in a measured section of 600 meters. Along the electrodes, wiring was laid down and connected to the electrodes, the wiring cables were connected to each other through switch boxes. The whole system was linked to the ERT measuring device and a battery. Water was poured over the soil surrounding each electrode as wet soil conducts better, giving better results. Before starting the tomography, the ERT measuring device measures the resistivity of each electrode. This way, the position of disconnected electrodes could be determined. All disconnected electrodes were fixed and the ERT measurement started. This took one hour.

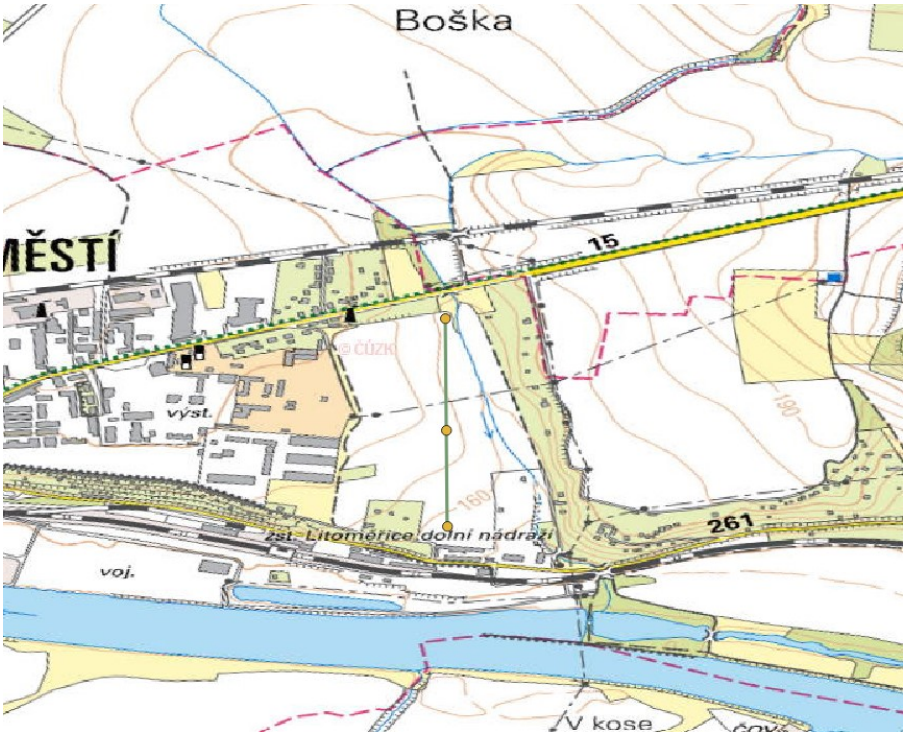

Figure 36: Profile ERT measurements

Figure 37: ERT measuring device and battery power source

Figure 38: Electrode connected to the wiring

Figure 39: Wetting soil around electrode

Figure 40: Switch boxes connecting the wires

Figure 41: ERT section

6.1.3 Results

The acquired ERT data was inverted using the program RES2Dinv and the result can be seen in Figure 42. The topography of the terrain was included. The horizontal layers appear relatively laterally continuous with some anomalies on the edges on the section and a disruption in the middle at a depth of 20m and at 270m from the starting point. The edges of a section are generally less reliable, as fewer measurements are taken there, therefore the anomalies could be attributed to this. The high resistivity region on the right (south) edge at a depth of 20m could potentially be caused by a change in water table. The Elbe river flows approximately 200m further South and lays 30m lower. The water table will decrease when moving towards the river, leaving the rocks above this water table dry and thus showing a higher resistivity.
For the cause of the disruption in the middle several hypotheses have been brought forward: the presence of a fault, interference caused by the overhead electricity cables and the presence of two pipelines. It is known that is a fault network present in the Cretaceous sediments, also near the section. In Figure 43 the estimated location of nearby faults are shown, however these locations are very uncertain. The fault which is estimated to run through the field has an offset of 40 meters. Such a fault should clearly show a shift in layers in the ERT section, on the contrary the ERT results show horizontally continuous layering, which rules out the fault hypothesis.
The map in Figure 36 shows a black dashed line that is depicted crossing the field and the ERT section. This is the location of the overhead electricity cables. These cables could influence some types of geophysical methods, however they should not be able to influence ERT measurements.

The location of the first pipeline is depicted as a yellow line in Figure 44. This pipeline is more or less parallel to the section, thus we would expect the influence of the this pipeline to be fairly constant along the section and therefore not able to cause the anomaly in our results.
The second pipeline runs underneath the round out-sticking objects indicated in Figure 46. It is perpendicular to the section, crossing the section near the location of the anomaly. The exact distance was evaluated in QGIS and resulted in a distance of 261m, approximately 9 meters short of the 270m as read from the ERT inversion. Therefore this pipeline will have caused the anomaly in the results and the artifacts beneath it.

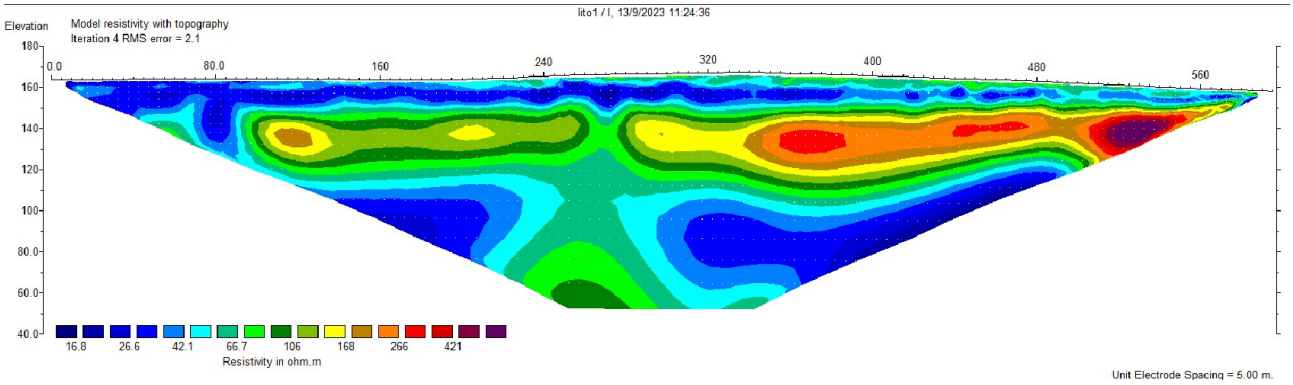

Figure 42: ERT inversion fieldwork conducted September 13th

The section can be divided in four horizontal layers. The top layer is approximately 10m thick and has a low resistivity but shows an increase in resistivity towards the end of the section. The second layer is 30 to 35 meters thick and has a higher resistivity with some lateral variability. The following layer is 35 to 40 meters thick with a low resistivity similar to the top layer. The medium resistivity region at the bottom of the section has an irregular shape which affects the middle part of the third layer, right underneath the location of the second pipeline. Taking into account these factors, it is likely that this medium resistivity region is an artifact caused by the pipeline.

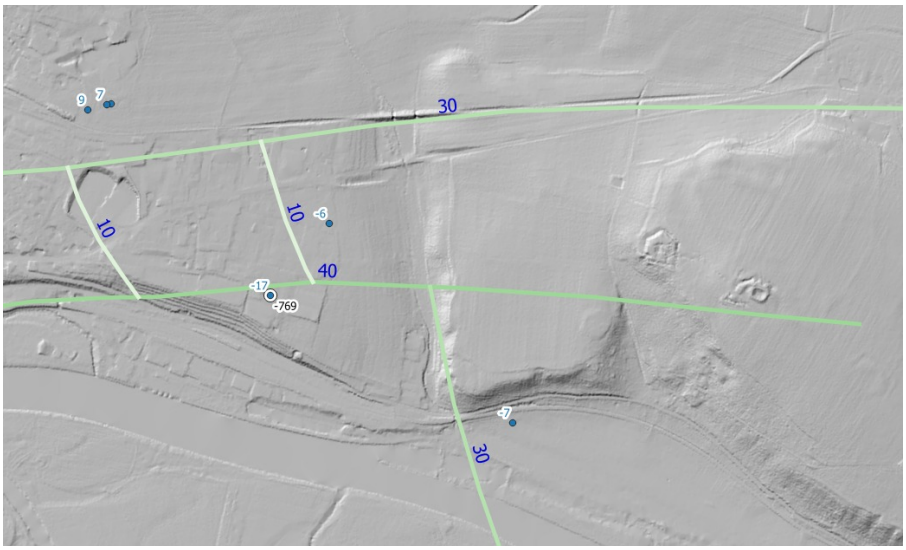

Figure 43: Estimated fault network around the field and PVGT-GT1 borehole

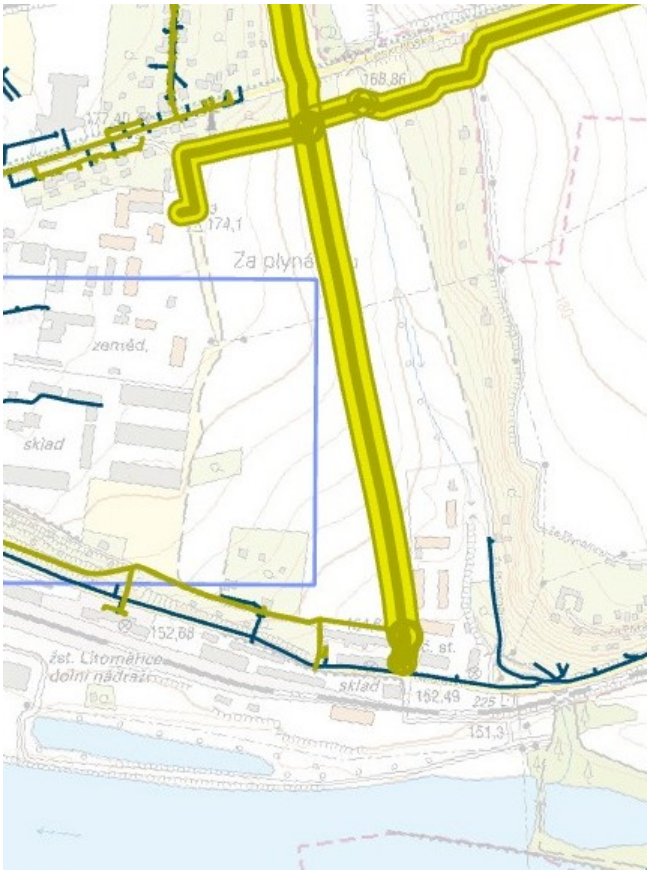

Figure 44: Location of pipeline 1 (yellow line)

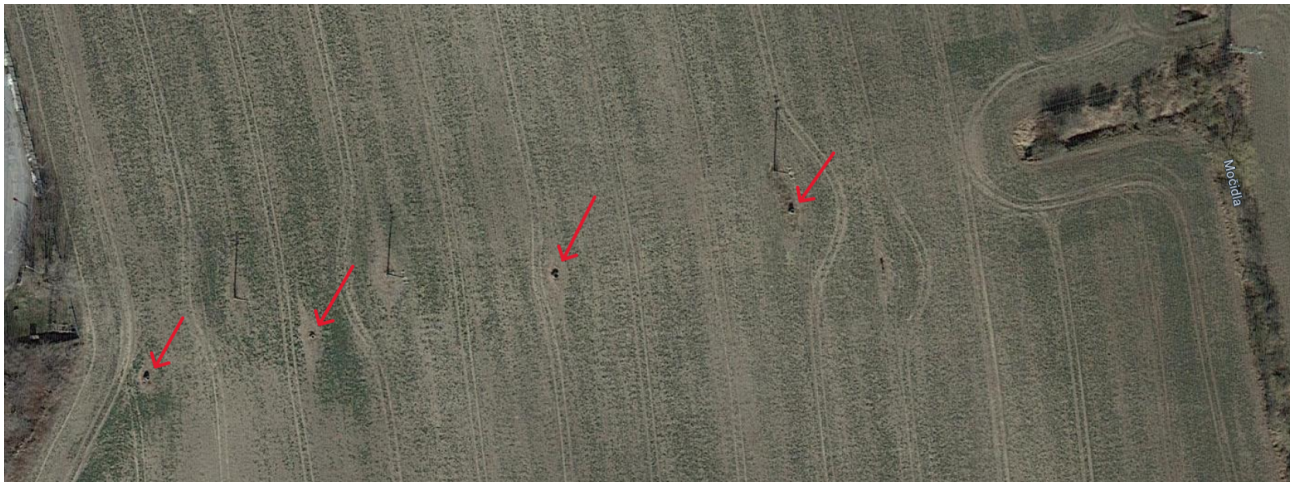

Figure 45: Location of pipeline 2

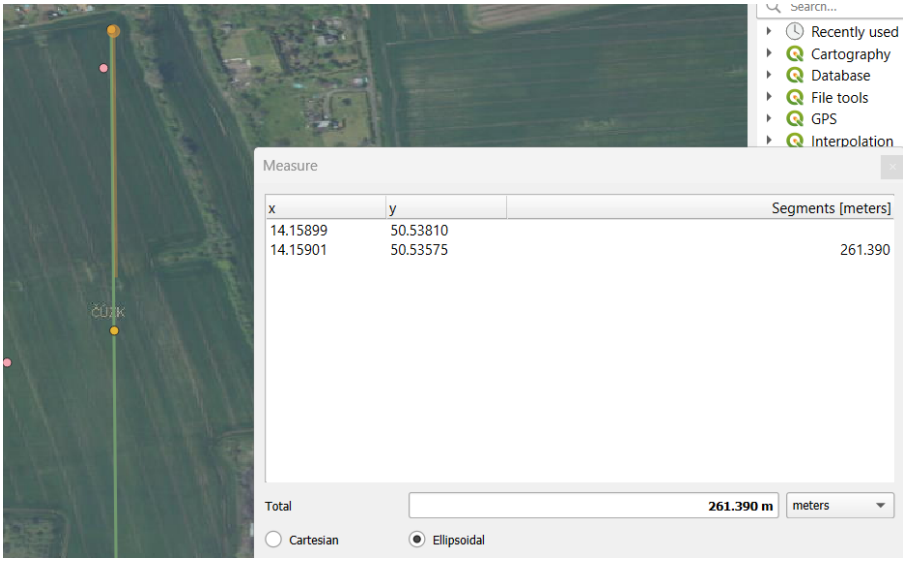

Figure 46: Distance between start of section and the crossing of the second pipeline and the section

6.1.4 Interpretation

The formations present in the upper part of the PVGT-LT1 borehole are the Cretaceous Jizera (0-90m), Bílá Hora (90-165m) and Peruc-Korycany (165-190m) formations [22]. The ERT data covers approximately 120 meters depth, meaning that the marine sandstones of the Jizera and Bílá Hora formations can be seen in the resistivity data. Muddy material conducts better than sand-rich layers, therefore it is likely that the blue coloured low resistivity layers are mud-rich and the high resistivity layers are more sandy. The elevation of the LT1 borehole is approximately 10 to 15 meters higher than the elevation of the ERT profile.

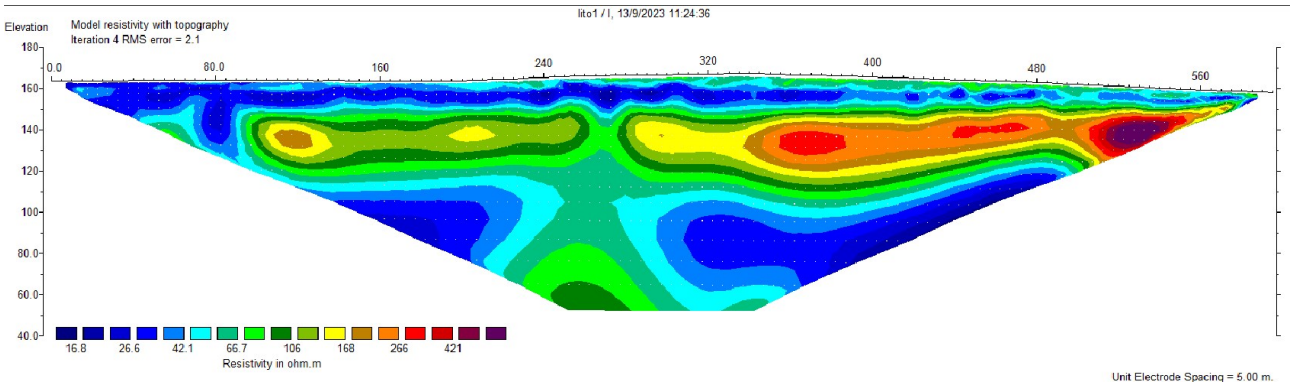

Figure 47: ERT inversion fieldwork conducted September 13th

6.2 Seismic refraction

Another way of geophysical exploration of the subsurface is the use of seismic methods. Various methods exist such as reflection or refraction seismics using body waves (P- and S-waves), or also the analysis of surface waves. In this study, refraction seismics were used first to create a tomography image of the underground. Additionally a surface wave analysis has been conducted using an active survey as well as a passive one. The two were later combined for a more accurate image.

6.2.1 Theory

The goal of the seismic refraction tomography survey is to get a 2D image of the P-wave velocities of the upper soil layers close to the RINGEN site. It uses the refracted waves at wave velocity contrasts that are apparent at changes of lithology in the underground. These different velocities are affected by the density and elastic properties of the sediments making up the subsurface. At interfaces of lithologies the wave propagation follows Snell's Law and refraction, reflection and diffraction occur. In this study we only consider the direct and critically refracted arrivals of waves at the measuring geophones, the refracted primary waves (P-waves), actively generated by us [3]. Multiple of these measuring "shots" are performed along different locations of a set up measuring profile, which will be further explained in the methodology section. The measured arrival times are then processed using the tomographic method which allows for the creation of a picture of the subsurface that highlights the continuous changes in velocity rather than the usual layered model of refraction surveys [25]. The basis for this is a initial velocity model where rays are iteratively traced through it to minimize the RMS error between the observed and the calculated travel times.

6.2.2 Methodology

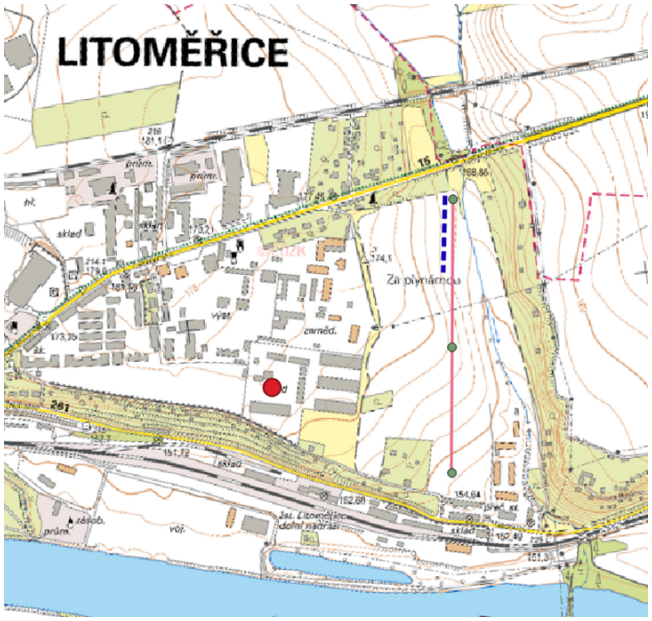

Figure 48: Location of the seismic profile (dotted blue line) and the pilot borehole (red dot)

The profile chosen was the same as the one used for ERT measurements. Here, only the most northern 120m of the ERT profile were used (see exact location in Figure 48). Using a measuring tape, a horizontal and a vertical geophone - both can be seen in Figure 49 - were placed into the ground every 5m. The horizontal geophones were placed to measure in the longitudinal direction. This lead to 24 geophones of each type along the profile. Geophones of the same type were connected and in the end connected to the measuring device (Figure 52). As a active signal source, a sledgehammer as seen in Figure 50 was used. This was done by hitting it on a metal plate that was connected to the measuring computer and thereby acted as a trigger. Overall, 17 shot locations within and outside of the geophone line were chosen, with 4 shots at each location inside the profile and 8 vertical and 8 horizontal shots at each of the offset shot locations situated 20, 10 and 2.5m north and south of the profile. Within the profile, shots were done every 10m. This meant the first shot within the profile was 7.5m into the profile. Figure 51 gives an schematic overview of the locations of shots along the geophone profile.

The exact setup for all shot locations as seen in SeisImager is in appendix 91. After the active measurements, a passive measurement was conducted for a duration of 30 minutes. The horizontal geophones were then rotated by 90° to measure the transverse signal. Then 8 measurements were taken at the offset shots locations again and another 15 minutes of passive signal was measured.

Figure 49: Horizontal (left) and vertical (right) geophones used

Figure 50: Group member Luis with the hammer and the metal disk on the ground

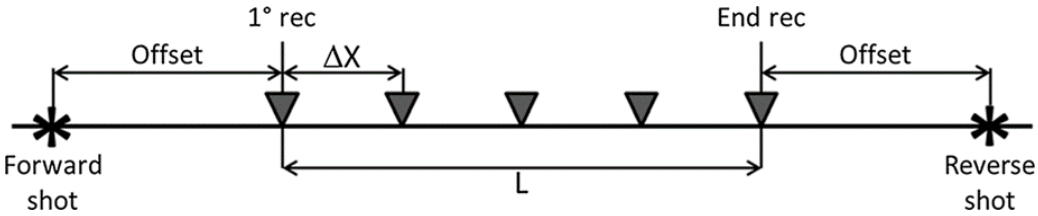

Figure 51: Schematic setup of the seismic profile including offset shots (from [10])

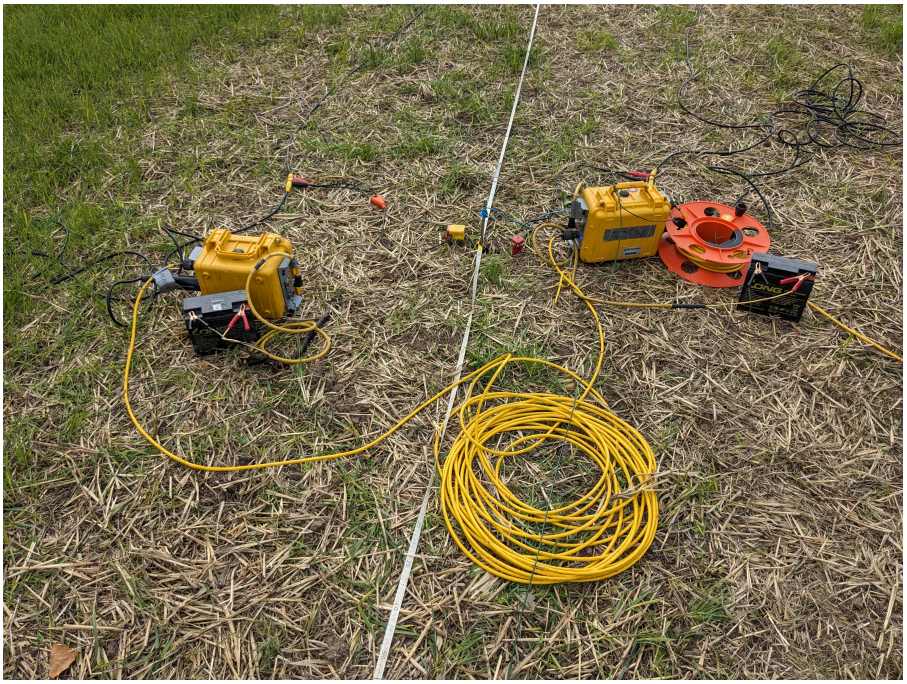

Figure 52: Set up seismic refraction measurements

For the following processing steps, the SeisImager software by Geometrics was used. Stacked files for each shotpoint were generated. First arrival times were picked for each of the 17 shot locations (see appendix 92 for an example). The traveltime curves resulting from the picking can be seen in appendix 93. The reciprocal traveltimes were checked to ensure a low error. When this is not the case, picks were adjusted and updated to reach a lower error (ideally lower than 5 %, but due to the data quality that was not possible for all reciprocal traveltimes). From these curves, the break points are selected at which the curves for each shot location first deviate from their approximately straight trajectory (see 93). This is done once for a initial two layer model that was chosen for this analysis. The resulting initial two-layer model is shown in figure 53. That layered model acts as the base for a 15 layer initial model used in the next step, the inversion.
The inversion was executed using the standard parameters of the SeisImager Plotrefa software. A total of 30 iterations from the initial model were used. Additionally raytrace paths through the model were calculated as can be seen in the results section.

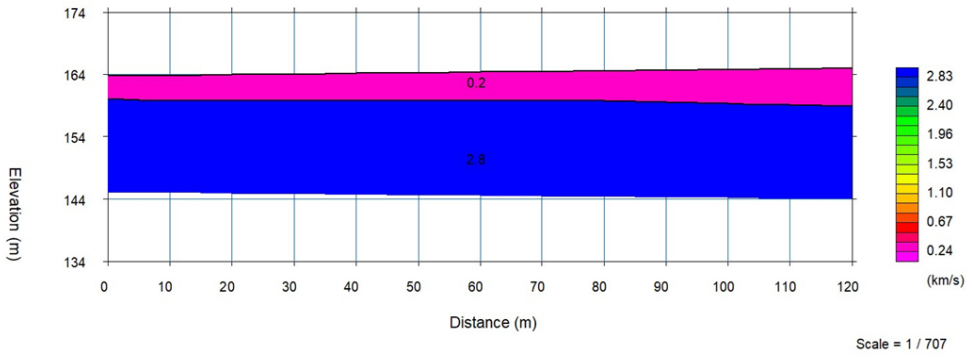

Figure 53: Initial two layer model for refraction seismics

6.2.3 Results

The figures 54 and 55 show the final inversion result of the reflection tomography survey conducted. In figure 54 we can see the smoothed refraction velocity image for the 12m long profile plus the included offset. It is important to note that the part of the image below 140m elevation can be neglected as there was no data

available below this point. This is further logical when looking at figure 55. This image shows the raytraces created for the simulation within the gridblock cells that were used in the model. No rays reach further down than 140m elevation. The high density of raytrace paths means a high resolution of the final simulation result. In the appendix 94 additionally the traveltime curves calculated from the inversion compared to the observed ones are shown.
P-wave velocities range from 0.3km/s to 3km/s as that were the boundaries set during the inversion process. The velocity generally increases with depth in this study. Overall we can see a dip at around the 50m mark of the profile. Towards the right (towards south along the profile) the lower velocity layers reach about 10m deeper into the ground.
This survey was mostly done to get a general overview of the structure in the underground, and less to get specific velocity values. In conclusion it can be said that this goal was reached to a satisfying degree, although the low depth penetration is a limitation that needs to be equated for with future deeper seismic surveys.

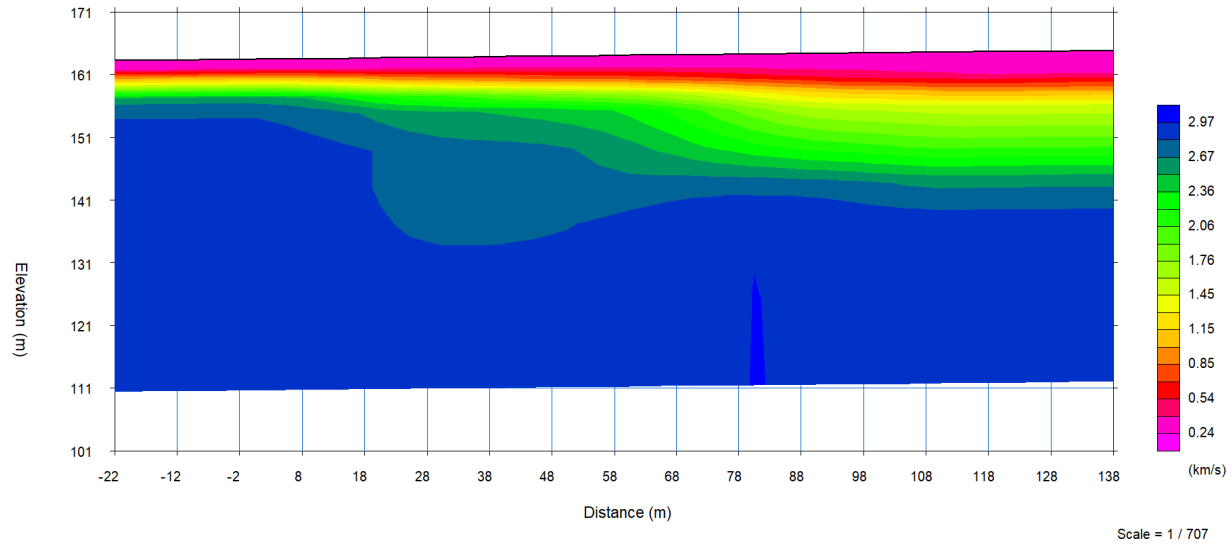

Figure 54: modelling result for the seismic refraction tomography

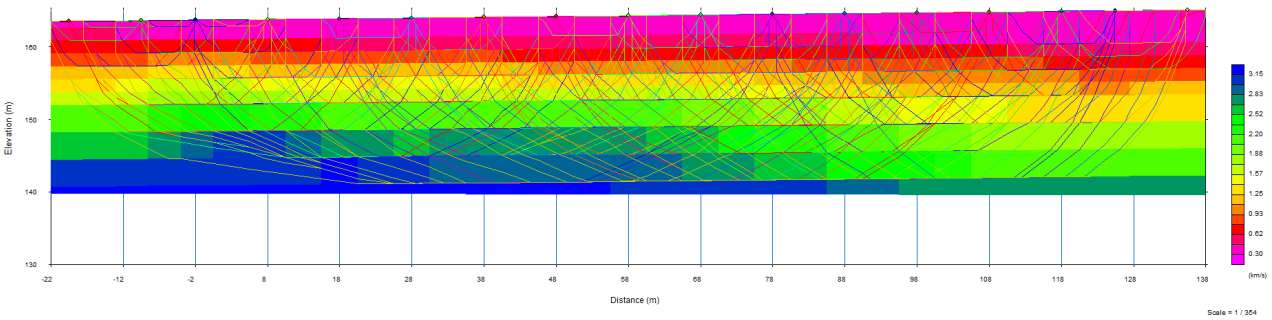

Figure 55: refraction tomography grid blocks including raytraces

6.3 Surface wave analysis

6.3.1 Theory

Additionally we analyzed surface waves generated in the same general setup with the goal to acquire 1D S-wave velocity profiles of the uppermost subsurface layers. This is a simple good tool to enhance the interpretation of

the refraction survey conducted before [17]. Here Multichannel Analysis of Surface Waves (MASW) as an active method and Microtremor Array Measurements (MAM) as a passive one were conducted. Surface waves carry the highest amount of seismic energy that travels in the form of Rayleigh waves or Love waves which are detectable with vertical and horizontal geophones respectively. To achieve a higher depth penetration, low frequency data is required which is provided by the passive data that is processed together with the active data generated by a hammer impulse. The multiple steps carried out to arrive at the s-wave velocity model are further described in the methodology section. It mostly revolves around the creation and interpretation of dispersion images created from the measurement data. A phenomenon that might occur during the interpretation of MASW data is the occurrence of higher modes in the dispersion images.

6.3.2 Methodology

As the data used was taken from the same measuring campaign as the before mentioned refraction survey, see that section for the acquisition.
For processing, we again used the SeisImager software. With the surface wave analysis wizard it is possible to go through all analysis step, for the MASW or the MAM separately. All the following steps were done once for the vertical signal, so the Rayleigh waves, and a second time for the transversal signal, so the Love waves. Starting with the MASW, the shot results are stacked for each location and loaded into the software. Here a dispersion image is created (like the one in figure 56) and the dispersion curve is picked by selecting the highest signal. This dispersion curve is then cut to only account for the frequency that were detectable in the image. For the MASW, the frequency range in this case was usually between 12 and about 45Hz. The same steps were carried out for the MAM by loading in all analysis files at once (appendix 95 shows the signals in the frequency domain for the MAM). Here the lower frequency spectrum of 5 to 15Hz was covered. For the MASW two offset shot locations with good data were selected and the dispersion curve between the two averaged out. That dispersion curve was then combined with the MAM one, resulting in the dispersion curve displayed in figure 57.
All dispersion images and curves not shown here (MASW and MAM) can be found in the seismic appendix B from 96 to 98.
From a 15 layer initial velocity model ranging down to 50m depth an inversion is carried out. With 15 inversion steps, the final error is about 7% for the velocity model combined from active and passive Rayleigh measurements as shown in the results.

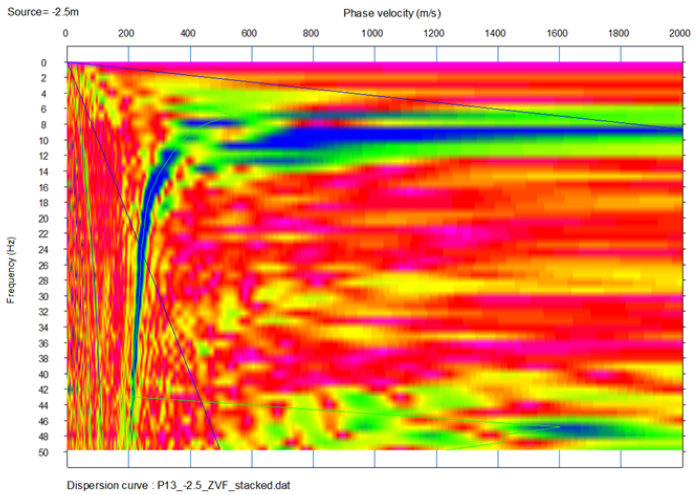

Figure 56: Dispersion image used for the MASW analysis

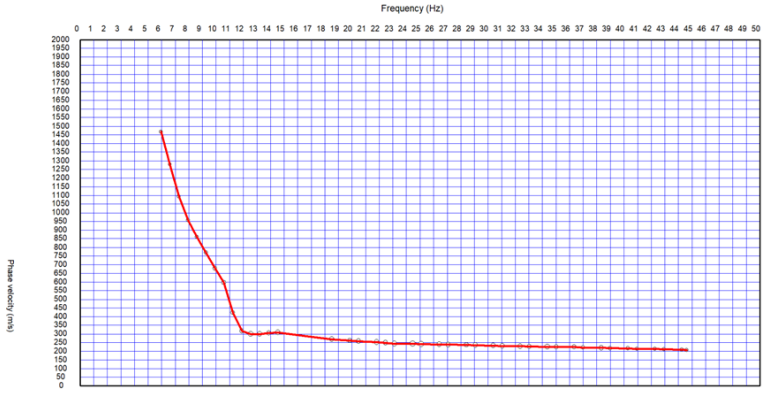

Figure 57: Dispersion curve from combined MASW and MAM results

6.3.3 Results

A final 1D S-wave velocity model until 50m depth for the covered profile east of the PVGT-LT1 borehole is displayed in figure 58. The profile shown is as mentioned based on the Rayleigh wave measurements for combined MASW and MAM. The light gray part in the topmost meter indicates low accuracy, which is caused by the lack of very high frequency data in the dispersion curve. As it is only the upmost soil layer this can be neglected. As visible from the profile the s-wave velocity increases throughout depth. The Love waves did not yield any velocity profile results in the end. That was due to an unresolvable software error which made it not possible to invert the data. That means the Love and Rayleigh wave results could not be combined which would probably have lead to a more accurate result.
As interpretation of these results it can be said that the s-wave velocity is generally higher than it could be expected from the borehole information throughout the determined profile. The soil profile at the pilot borehole 400m away from the profile can be seen in figure 59. The sediments found there would generally give lower s-wave velocities than seen here. The increase with depth is reasonable, we expect increasing density throughout the unconsolidated soil with increasing depth which leads to higher wave velocities. The s-wave velocity ranges from about 150m/s in the shallowest accurate section (dark grey parts) to about 1900m/s at 50m depth. When trying to match the profile to the known shallow ground geology of the borehole, it can be observed that there are jumps in s-wave velocity in similar depths as in the borehole, for example the boundary from Quaternary to Jizera marlstones at 25m. One possible explanation for the divergence in velocities is the possible accidental selection of higher modes instead of the fundamental mode for the dispersion curve in the dispersion curve. This cannot be fully ruled out.
Overall the data quality was not ideal for the entire surface wave analysis. The end result still gives a good first approximation of shallow geophysical ground characteristics that should be combined with further (seismic) studies in the future. This leads to better understanding and therefore a better integration into the considerations for the planned BTES systems.

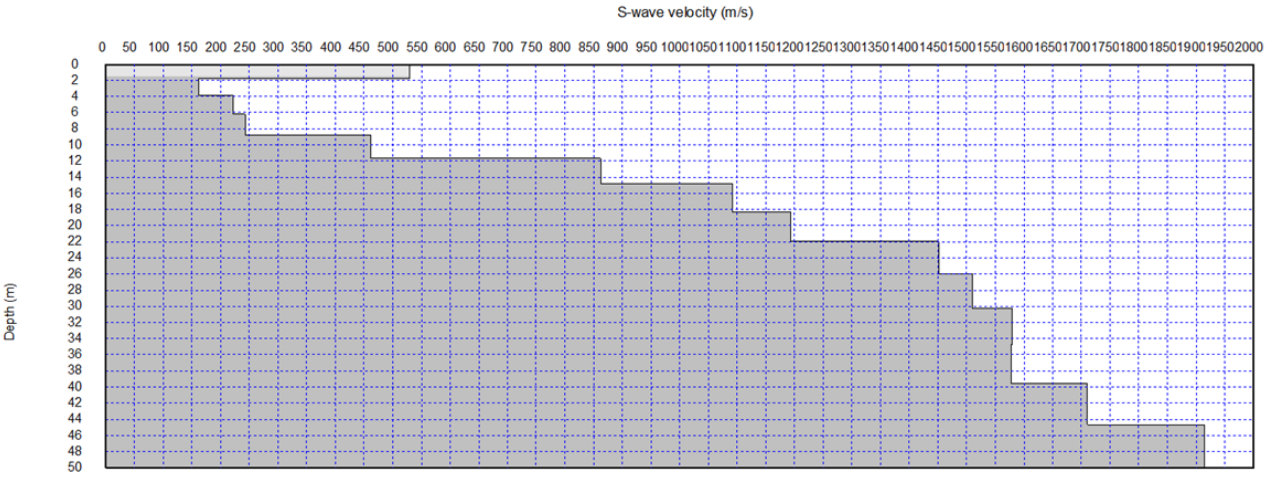

Figure 58: S-wave velocity results for combined MAM & MASW Rayleigh wave analysis

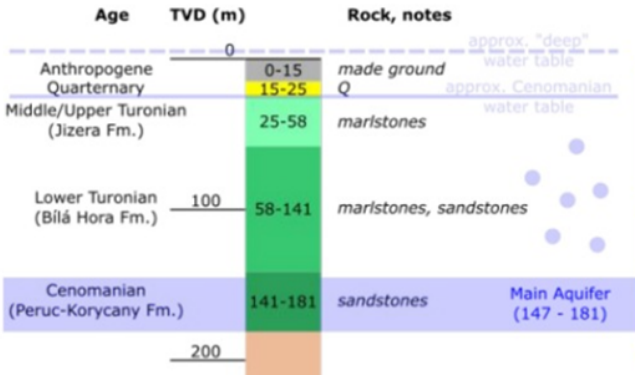

Figure 59: Soil data from the PVGT-LT1 pilot borehole

6.4 Linking ERT and seimics results

As mentioned earlier, it is desirable to carry out a broad range of geophysical methods on the same area to combine these and gather a broader and less error prone picture of the underground conditions. Two of those methods that go well together are the ERT and refraction tomography surveys discussed in the previous chapters. The two results are displayed alongside each other in figure 60. Again, the tomography profile only includes data above 140m so greater depths than that are not part of the comparison. Here it is visible that - despite the quite low accuracy of the ERT results in that part of the profile close to its edge - the two methods show similar results. Especially the layer boundary at about 10m depth is depicted in both method's results. That again aligns with the borehole data, see figure 59.
Overall the results give a good approximation of shallow underground geophysical parameters and give the option to later combine them with the data resulting from future deeper seismic measurements along this same profile as one of the planned profiles.

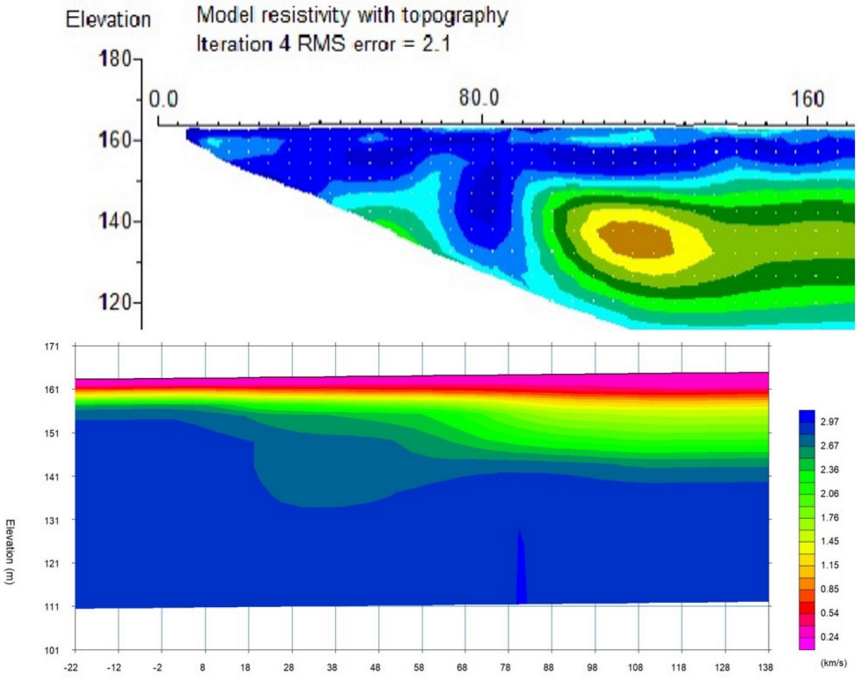

Figure 60: Results of the ERT and refraction seismic section roughly compared

6.5 Gravity data

In addition to the conducted measurements of resistivity and seismics, we also took a closer look at pre-existing gravitational datasets of the surrounding area.

6.5.1 Theory

The gravitational field at the surface is dependent on all kind of parameters. The altitude on it's own would results in a lower measured field, as it's a further distance from the core. Further more it takes in account the attraction of the rocks that cause this altitude. To correct for all this, we use the Complete Bouguer Anomaloy or CBA [30]. This method includes a removal of topographic features and more terrain features.
This allows us to use the CBA to directly draw conclusions about the sub-surface structure of the region. We no longer have to take the topography and such in account. The CBA thus helps us to make statements about the subsurface density contrast.

6.5.2 Methodology of data processing

1. **Data acquisition.** For this part we have not acquired the gravity-data ourselves, but used data acquired by other institutions. In this specific instance we have used the data provided to us by the České geologické služby (Czech geological survey). The data is provided in complete Bouguer anomaly in milligals. The spatial data is in the UTM format with a resolution of $\approx 30/km^2$.

2. **Conversion to regular grid.** To do some mathematical analysis it is useful to convert the data to a regular spaced grid. We use Universal Kriging for this. We found that fitting the variogram to an exponential form yielded the most natural results. The resolution of the resulting is dependent of the the size of the domain, for computational reasons.

3. **Data visualisation and analysis** In order to get a feel for the gravitational we have plotted the data using Matplotlib. We have created a contour map, and a map of derivative of the field. Which helps you to visually determine where gravitational anomalies occur.

6.5.3 Linsser-Method

A method commonly used in the Czech Republic for inversion of gravitational data is the Linsser-method. This method assumes that a gravity field can be described as a linear combination of a gravity master curve and the regional gravity field. We attempt to use this technique as well in this report. Following the steps as outlined by Anastasiia[2]. The Linsser-method enables us to describe the measured gravitational field as the superposition of these two aforementioned fields as given in equation 1. Were $M(x)$ is the master curve caused by the subsurface density contrasts, E the fitted amplitude of this master curve. $B(x)$ the regional (long distance) field and R it's coefficient.

$$g(x) = EM(x) \ + \ RB(x) \tag{1}$$

For our purposes, we will ignore any regional changes and will just focus on the Master curve. To filter out these long term variations we apply a high pass filter. Yielding $B(x) = 0$. What we are left with is an map of the region with only the local variations, the "high frequencies". These variations are generally caused by localized anomlaies. We now have $g(x) = EM(x)$. As an example we will take almost ideal anomaly as shown in figure 63. We now use forward modelling to calculate certain master curves and fit a geometry and density contrast to the measured profile.

6.5.4 Results

When creating a contourplot of the region using the kriged data, we get figure 61. It can can clearly see there is quite some variation in the region, with a peak in the NW direction.

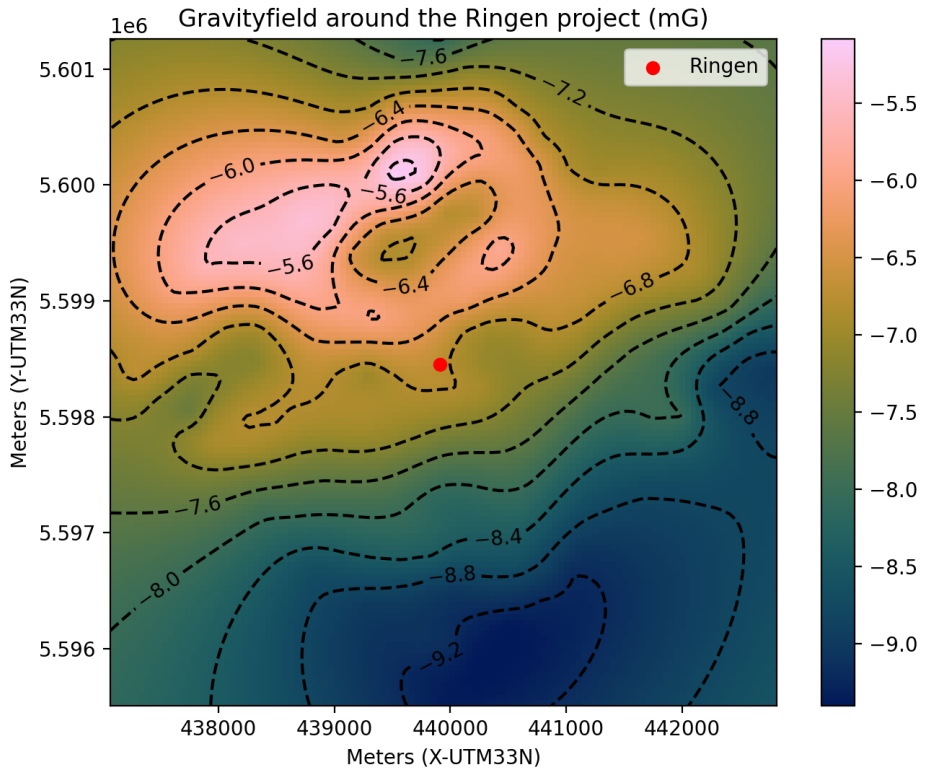

Figure 61: Gravityfield around Ringen

The derivative field is shown in figure 62. In this plot the colour again corresponds to the measured CBA. The arrow direction is the direction of the derivative and the size of the vector the euclidian norm. Finding the boundaries of anomalies are easier to find in such a figure. As indicated for ideal situations in figure 63.

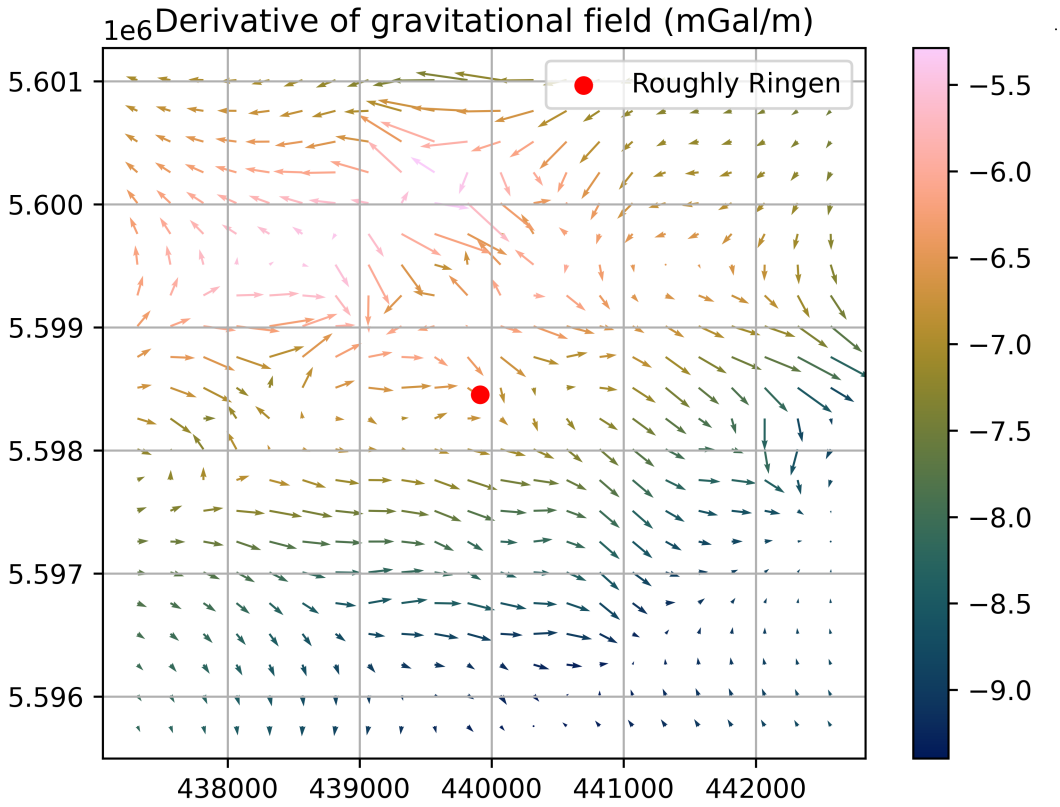

Figure 62: Derivative of the gravityfield around Ringen.

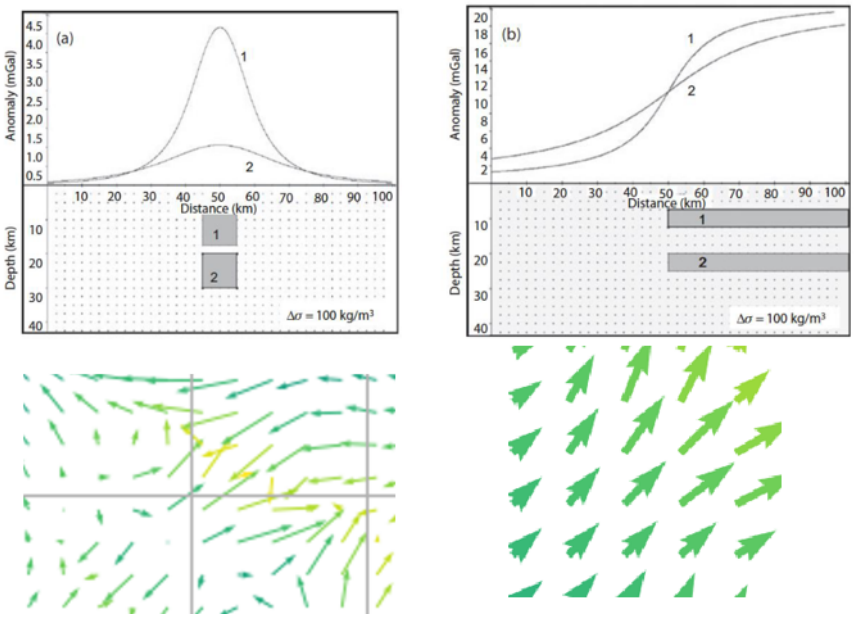

Figure 63: Examples of anomalies and corresponding vectorfield.

As mentioned before we use pyGIMLI for inversion. We use an unstructured grid for this. For an inversion such as this one we have a bunch of degrees of freedom and thus need to tune the parameters to fit the real world, geological, model. A few examples of possible inversions for a 2D crossection are given in figure 64.

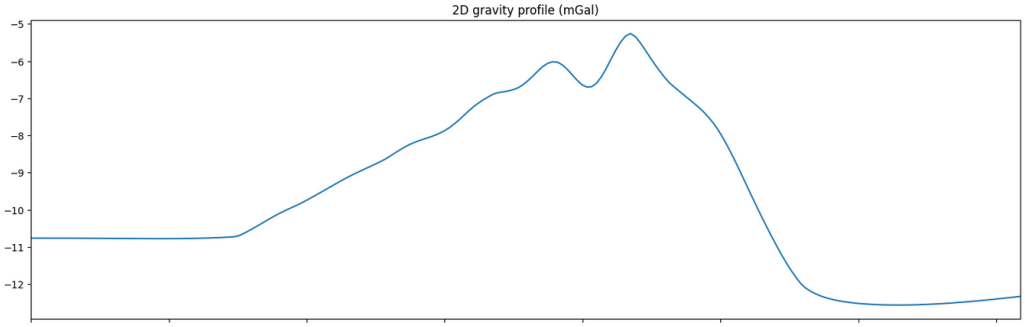

(a) Measured profile

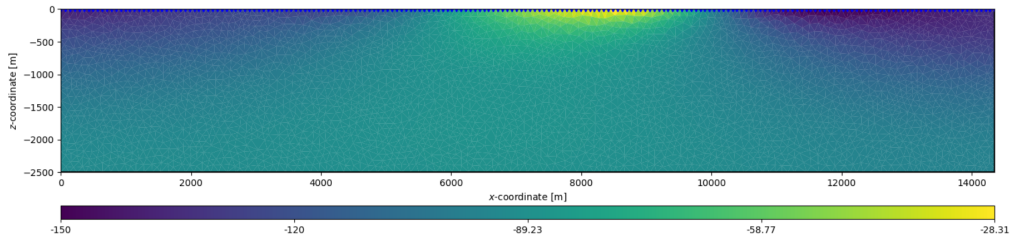

(b) Possible inversion, density is given in relative density.

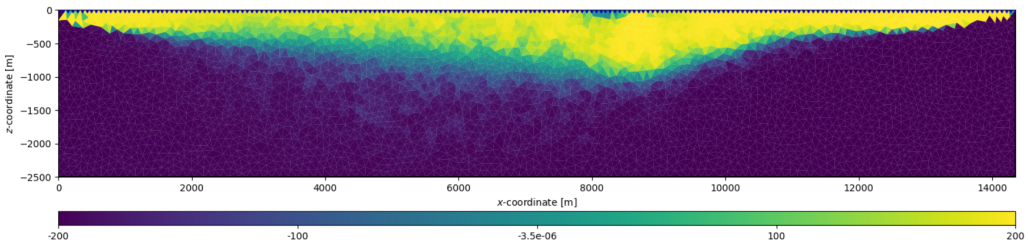

(c) Possible inversion, density is given in relative density.

Figure 64: A 2D measured profile inverted in two different ways.

The figures produced by the inversion differ greatly from each other. This is caused by the fact we have numerous of degrees of freedom that do not provide boundary conditions.
A result of a possible geometry and corresponding field master curve is given in figure 65.

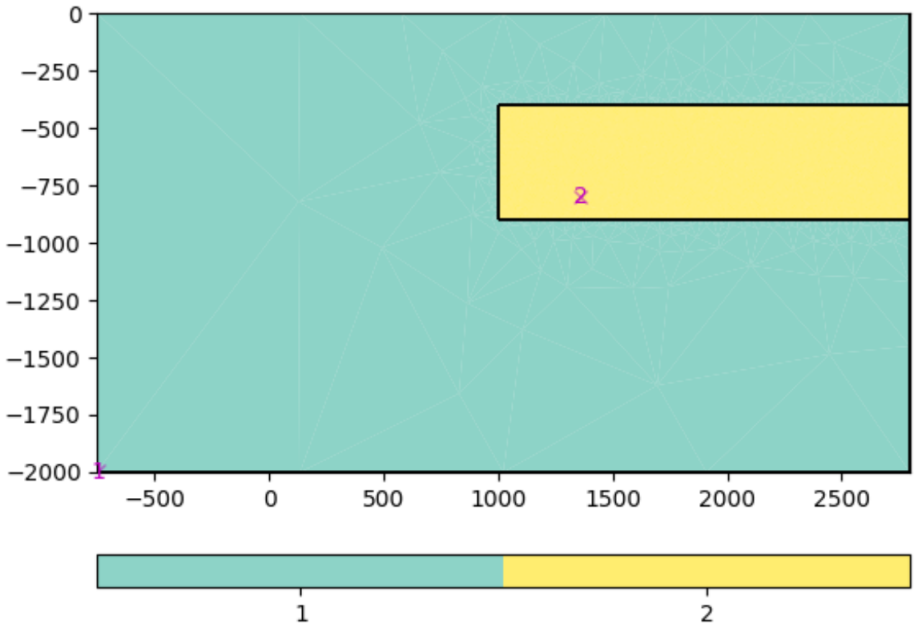

(a) Best fit geometry assuming conditions

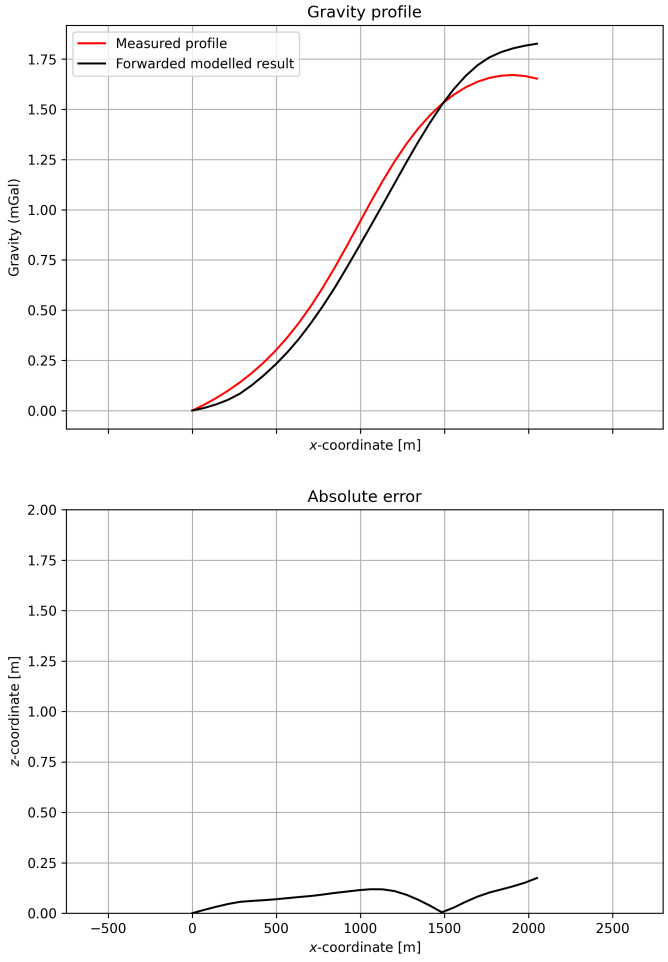

(b) The measured and forward modelled gravity profiles

Figure 65

6.5.5 Interpretation

As shown in the previous examples, certain anomalies can be connected to certain subsurface heterogenities. When we look at the geological map [22], we can see that this overlaps very well with our measured signal. The geological map used as reference is also partly constructed using these same gravitational measurements, thus we can confirm these findings.

7 Rock sample analysis

The measurements and studied rocks in this section are not related to the planned geothermal well in Litoměřice but originate from a uranium mine in the east of the Czech Republic. The original plan was to use cores from a newly drilled well at the RINGEN site, however as the drilling was delayed other options had to be considered. The uranium mine rock cores were retrieved from several depths in eight different boreholes. These are additional measurements carried out for another study conducted by the Charles University. Measurements were conducted on these uranium mine cores using two devices to determine the same two thermal properties: thermal conductivity and thermal diffusivity. The results will be compared to evaluate the similarity between the results as well as the advantages and disadvantages of each of the two methods. Conclusions on these topics can be taken into account in future measurements. Specifications on the samples can be found in Appendix A.

7.1 Methodology Hot Disk

The Hot Disk method or the transient plane source method uses a thin sensor which can measure thermal conductivity, thermal diffusivity, thermal effusivity and specific heat capacity. The sensor is placed between either two sample pieces (double sided) or a sample and insulating styrofoam (single sided). The conducting double spiral of the hot disk is warmed by electrical pulses and the rate at which the heat dissipates into the sample is measured by the sensor.

Sensors are available in different shapes and sizes, the appropriate sensor to use for a certain sample depends on the shape and size of the rock sample itself. The prerequisite is that the distance from the sensor to the nearest sample boundary is larger than the probing depth, following:

$$\Delta = C\sqrt{\kappa t} \tag{2}$$

where C is a constant of the order of unity, t is the total time of the transient, κ is the thermal diffusivity and Δ is a measure of how far the heating pulse has propagated into the sample during the time t.
Having a smaller Δ than the distance to the nearest boundary is important as the method assumes that the heat source is placed in an infinite medium. [12] This means that the length of the current pulse is significant as well. [11]

The samples were screwed down in the device with the Hot Disk in between the sample and the insulating styrofoam. In the computer program the right amount of power to use can be approximated based on material type. The linear part of the resulting transient graph is taken and the program will show the resulting measured thermal conductivity and diffusivity. If there are any errors the results will show a yellow coloured cell. The temperature applied to the sample should be between 3 and 5 Kelvin, if this is not the case the process should be repeated and the power increased or decreased. After a successful first measurement the properties of the same sample will be measured a second time. The rock is screwed loose and slightly shifted within the device before being screwed down again and measured a second time.

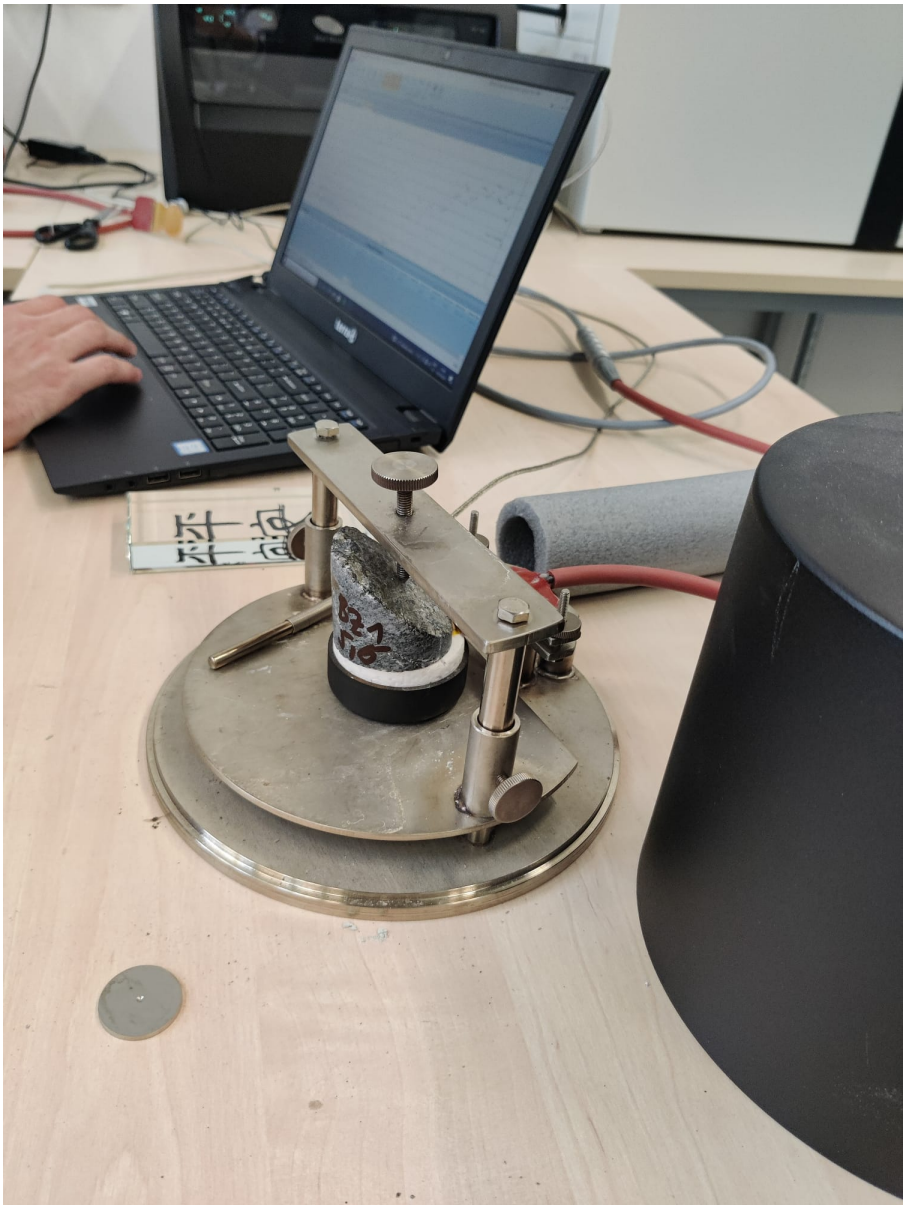

Figure 66: The hot disk device conducting a single sided measurement with sensor between rock sample and insulating styrofoam.

7.2 Results Hot Disk

The resulting thermal conductivity and diffusivity of the samples were plotted against the depth per borehole in the Figures below. In general the two measurements seem to give a similar result, which indicates that the samples are relatively homogeneous, having similar thermal properties at different locations. Samples from borehole BZ1-XII-55R (Figure 71) however show the most variation in both thermal conductivity and diffusivity. This means these samples are the most heterogeneous.

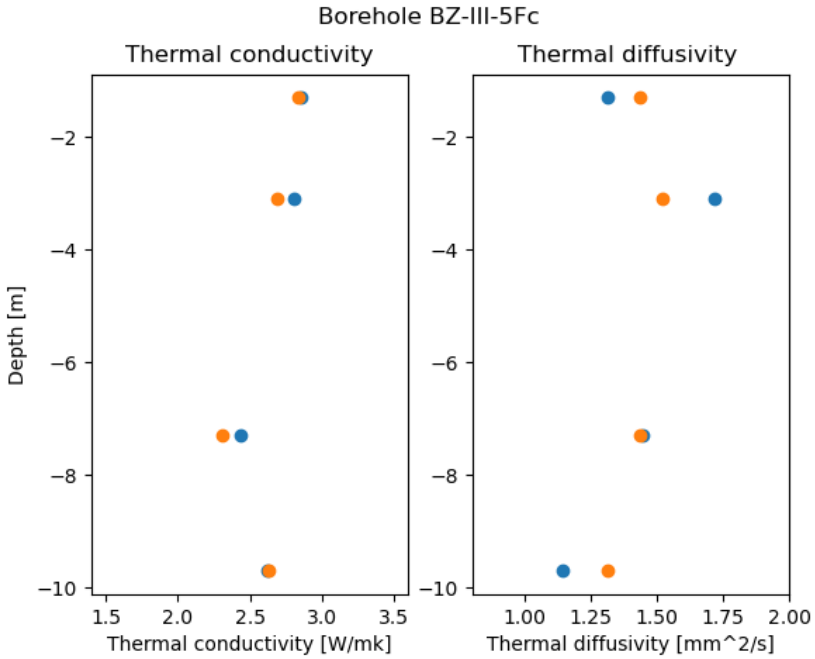

Figure 67: Thermal conductivity and diffusivity measurements borehole BZ-III-5Fc.

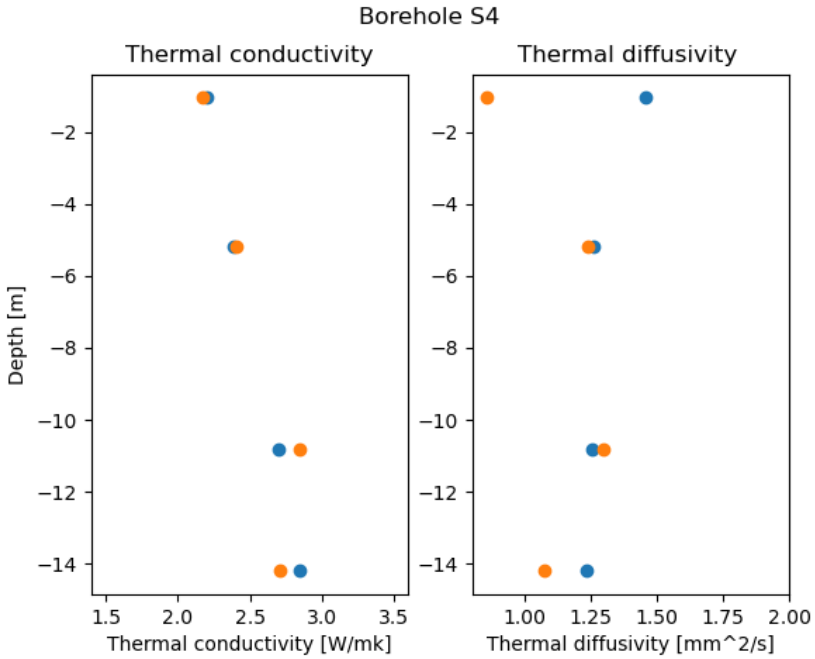

Figure 68: Thermal conductivity and diffusivity measurements borehole S4.

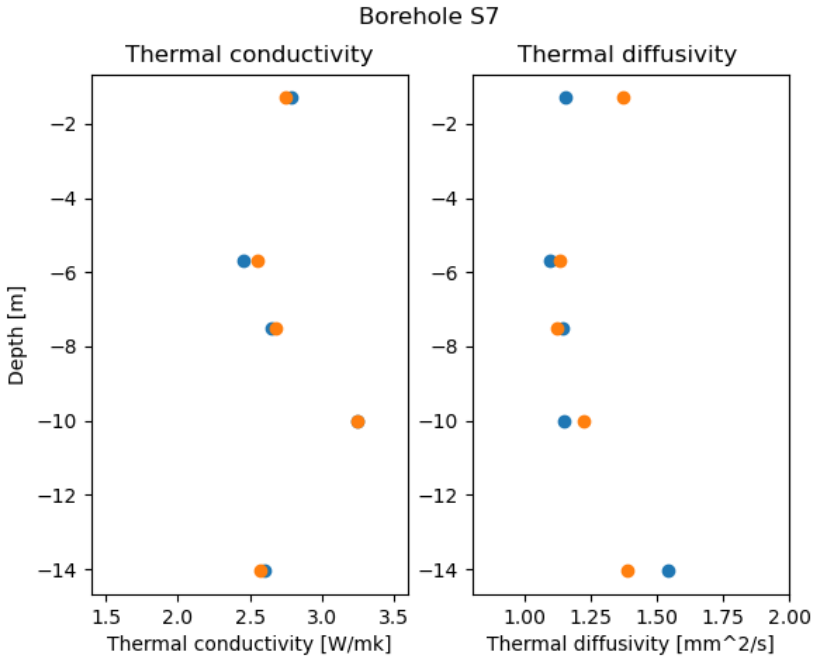

Figure 69: Thermal conductivity and diffusivity measurements borehole S7.

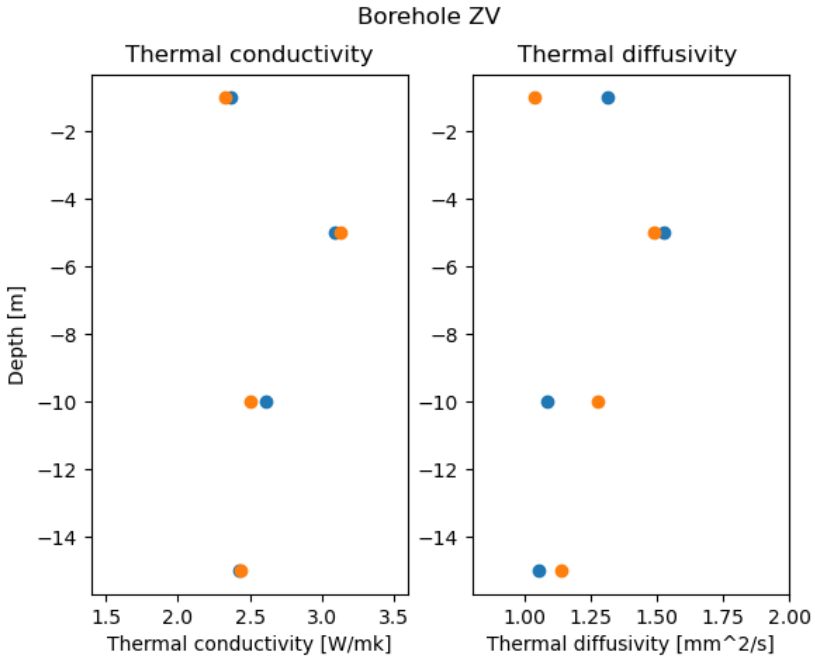

Figure 70: Thermal conductivity and diffusivity measurements borehole ZV.

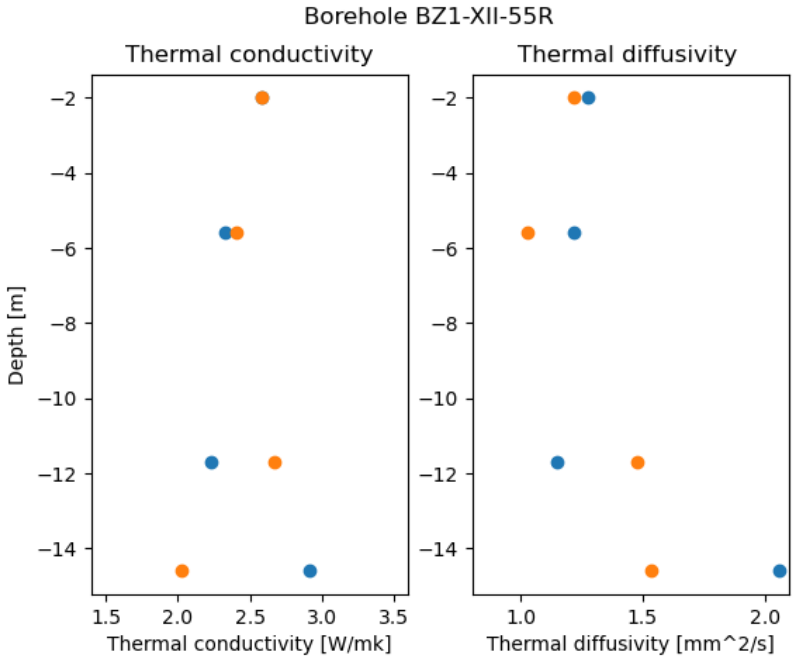

Figure 71: Thermal conductivity and diffusivity measurements borehole BZ1-XII-55R.

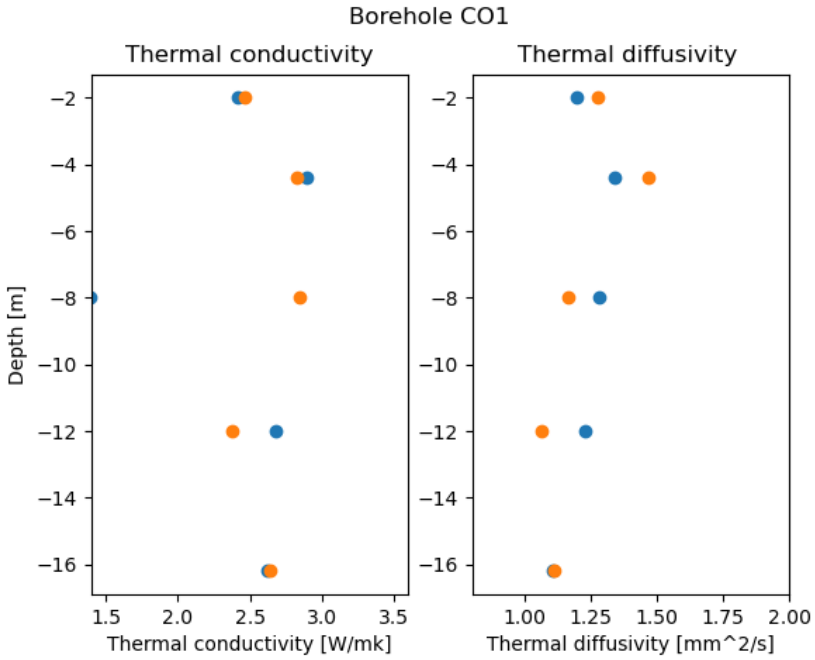

Figure 72: Thermal conductivity and diffusivity measurements borehole CO1.

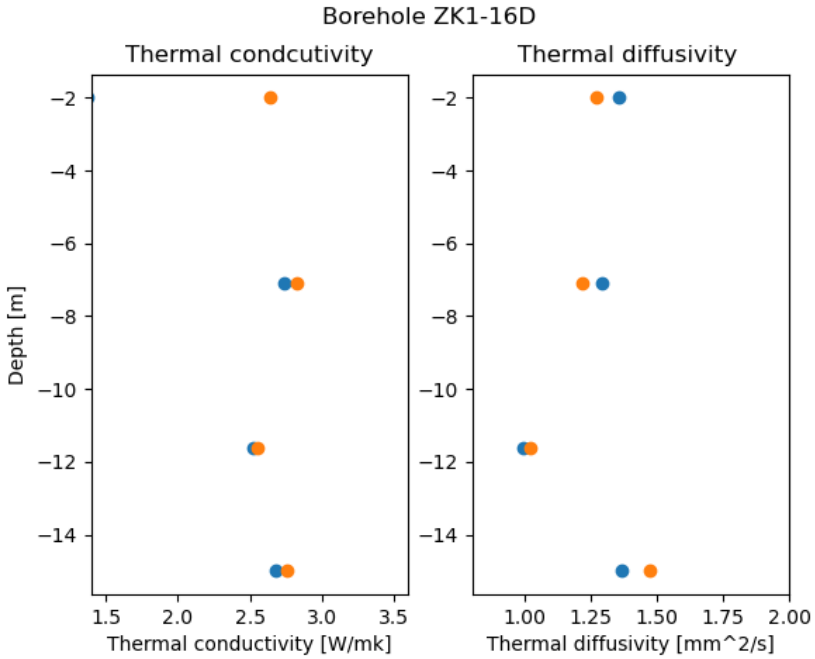

Figure 73: Thermal conductivity and diffusivity measurements borehole ZK1-16D.

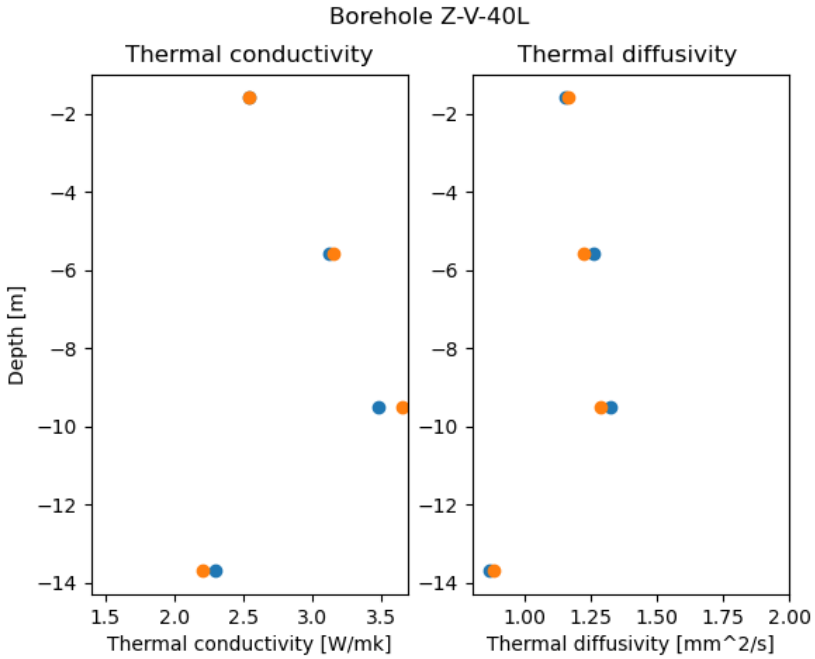

Figure 74: Thermal conductivity and diffusivity measurements borehole Z-V-40L.

7.3 Methodology Thermal Conductivity and Thermal diffusivity Scanner

The second methos we used for the thermal properties measurement was the use of a scanning apparatus. The method uses a moving heat source using the principles outlined by Yu. Popov in his paper [21]. The heat source aimed at the rock sample heats up the rock and reaching a quasi-steady state. Making the assumption of an infinite body because the total heat capacity is much bigger than the energy generated by the heat-source, this assumption is thus justified. The moment this quasi-steady state sets in, the temperature at location x (we measure across a 1D line so it is kept to a 1D case) is only dependent on the thermal conductivity and distance to the heat-source. We end up with equation 3, where we have set the position of the heat source to $x = 0$. In

this equation is θ the excess temperature, q the source power, and λ the thermal conductivity.

$$\theta(x) = \frac{q}{2\pi\lambda|x|} \tag{3}$$

Finding the exact factor for $\frac{q}{2\pi|x|}$ is tough. That's why we use two standards with known thermal conductivity as standards for the measurement. One made out of glass, which we have placed at the beginning of the profile and one made out of titanium which we have placed at the end of the profile. The thermal conductivity is known for both these standards and the distance between the heatsource and sensor ($|x|$) is known as well. This allows us to calculate this fraction, following the reasoning found in Yu. Popov's paper[21]. We can now express the thermal capacity of the rock sample we are interested in, in terms of known or measured parameters as shown in equation 4. Where the *st* subscript denotes the standard and *sample* subscript the sample we are interested in.

$$\lambda = \lambda_{st}\frac{\theta_{st}}{\theta_{sample}} \tag{4}$$

The cores are not entirely homogeneous and they have internal structure. One source of this anisotropy is the lamination within the core. Because of this we can not treat the heat conductivity as a scalar, but must consider it to be a tensor. We would like to measure this full tensor, we do this by measuring along varies angles: 0°, 45° and 90°. We can now see and quantify the amount of anisotropy.

7.4 Results optical scanner

Figure 75: The optical scanner, with samples on top.

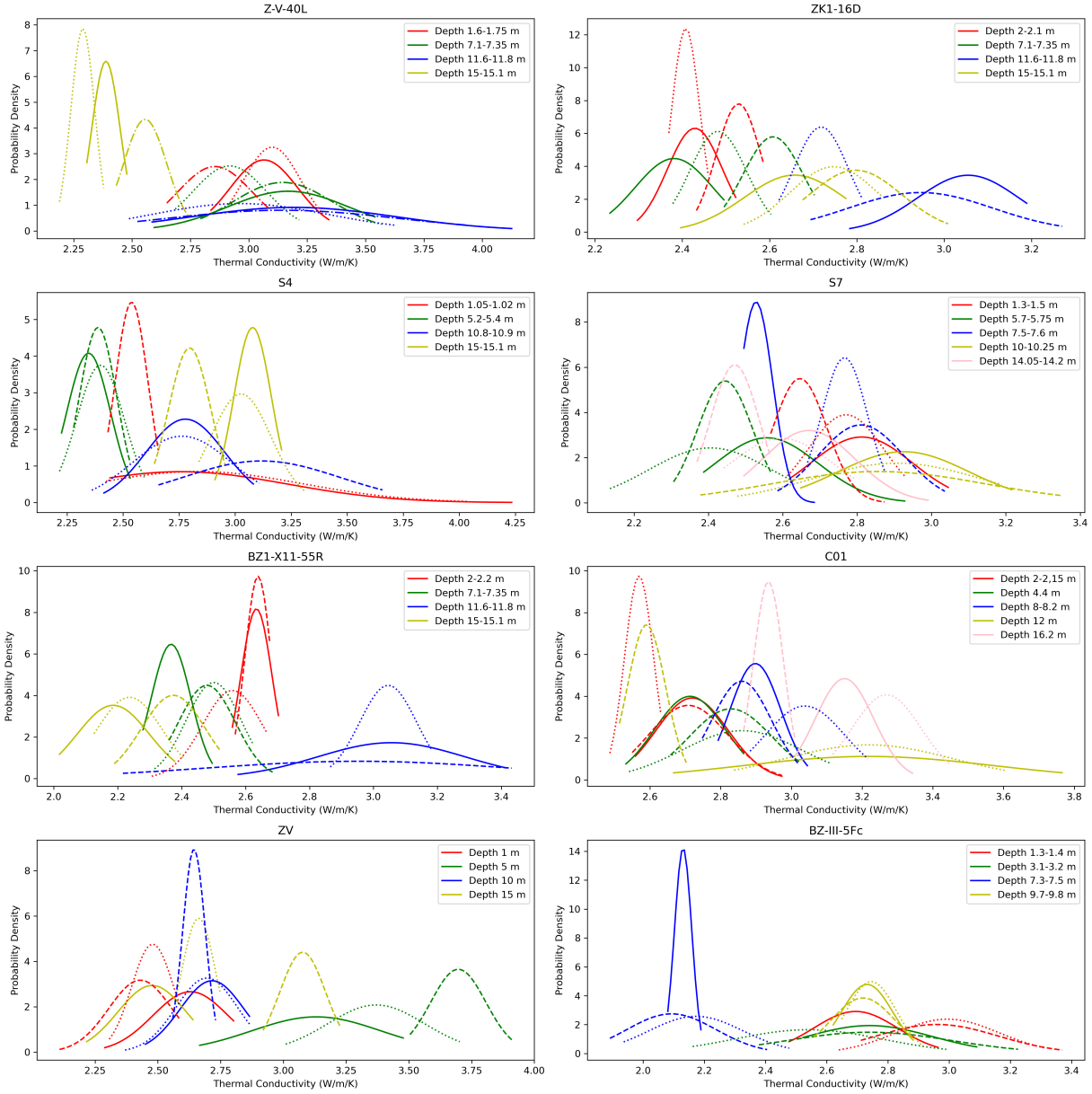

Figure 76: The measured heat conduction for every borehole. The linestyle corresponds to the angle measured. Solid: 0 Degree, Dotted: 45 Degree, Dashed: 90 Degree

We would like to quantify the anisotropy present in the cores. We take a simple approach for this, where we take the ratio of the lowest and highest measured thermal conductivity of a sample. This will yield a dimensionless quantity we will call α. As shown in equation 5.

$$\alpha = \frac{k_{min}}{k_{max}} \tag{5}$$

In Figure 77 these values are shown for all boreholes. Generally the anisotropy values within one borehole are quite similar or sometimes seem to contain a trend. However with only five data points, it's mostly guess work.

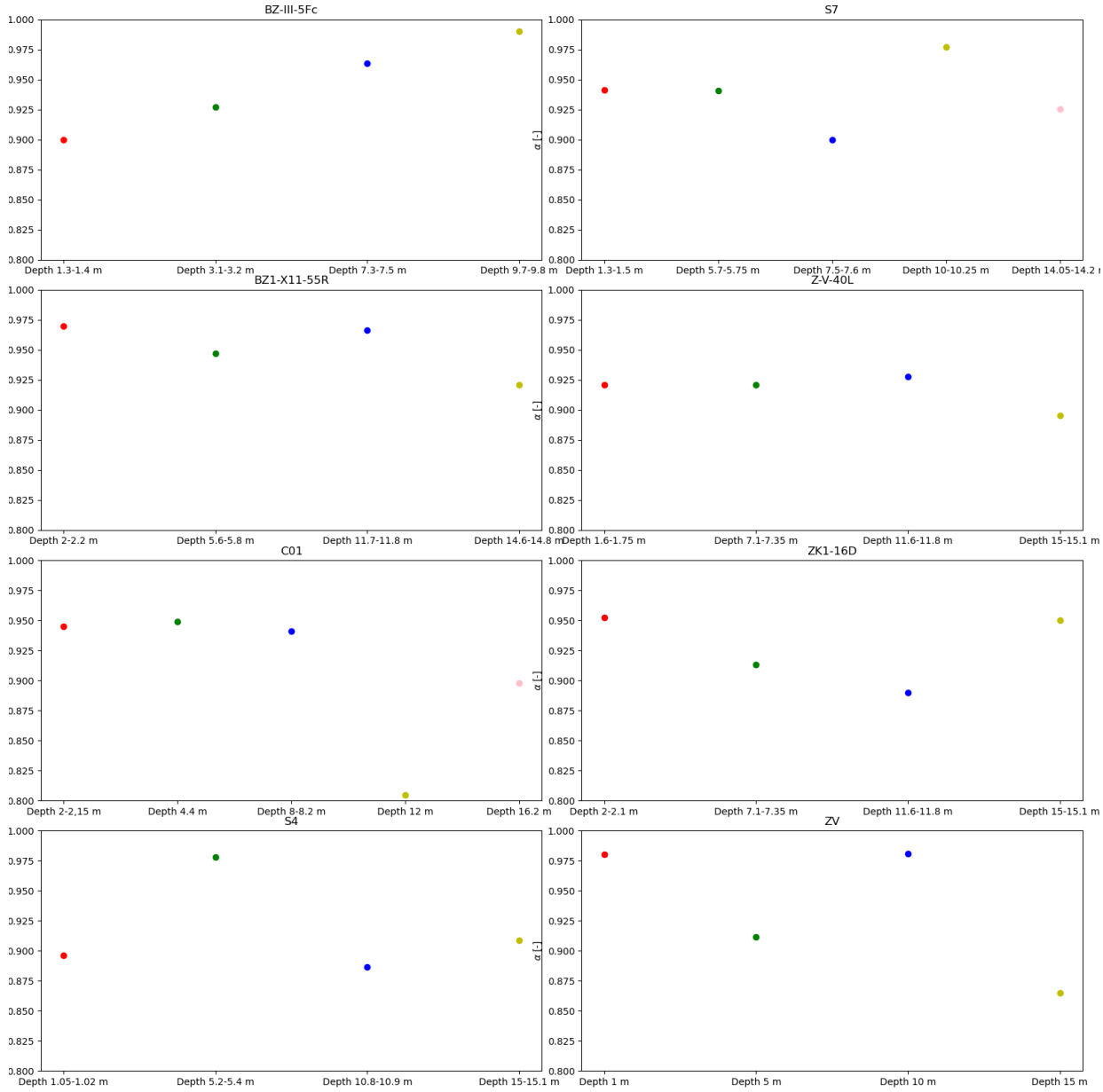

Figure 77: Found ratios for depth and borehole.

7.5 Comparison

The optical scanner allows the user to evaluate the degree of (an)isotropy as the thermal properties can be determined in different orientations, whereas the Hot Disk gives the average over one of the axes. Several cores can be evaluated at the same time with the optical scanner by lining them up on the device, making it time efficient. Measuring all uranium mine cores with the Hot Disk took approximately twice the time compared to the optical scanner, even though the measurements with the scanner were taken in three directions for each core. However, one huge advantage of the Hot Disk is being able to put the set up into the furnace in order to mimic the in-situ borehole conditions. The scanner is therefore best applicable to get a quick overview of a large number of samples in a time efficient manner while the Hot Disk is better for further in-depth research of the thermal properties in a realistic environment.

We would like to compare the measurements of both measurement techniques to see if there is some relative bias in the measurements. In Figure 78 we can see the plotted difference between the two measurement techniques per sample. As can been see, there seems to be almost no bias between the measurement technique. Even though differences between single measurements exist, they average out with almost no remaining bias.

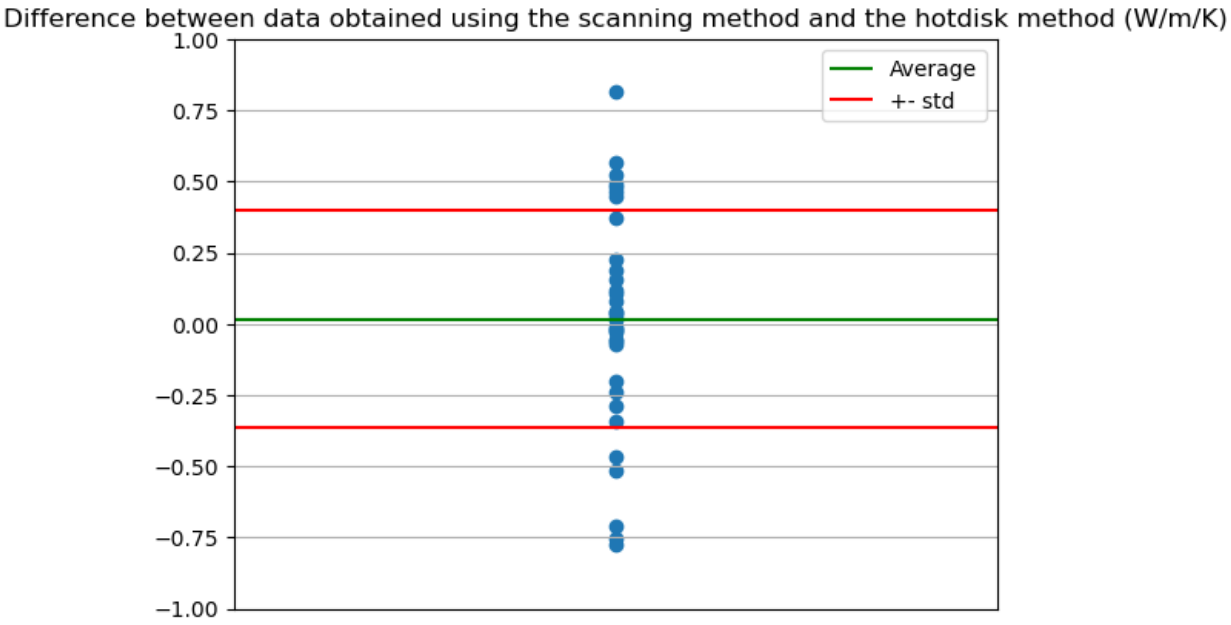

Figure 78: Difference between measurement techniques.

As the Hot Disk test does not measure any form of anisotropy while the optical scanner inherently does, we hypothesized that this could be a reason for the difference in the measured values between techniques. To test this hypothesis we calculate the correlation between the found difference and the aforementioned α ratio and fit a simple linear line to it. This is shown in Figure 79. We find no correlation between the anisotropy and measurement differences and thus reject this hypothesis.

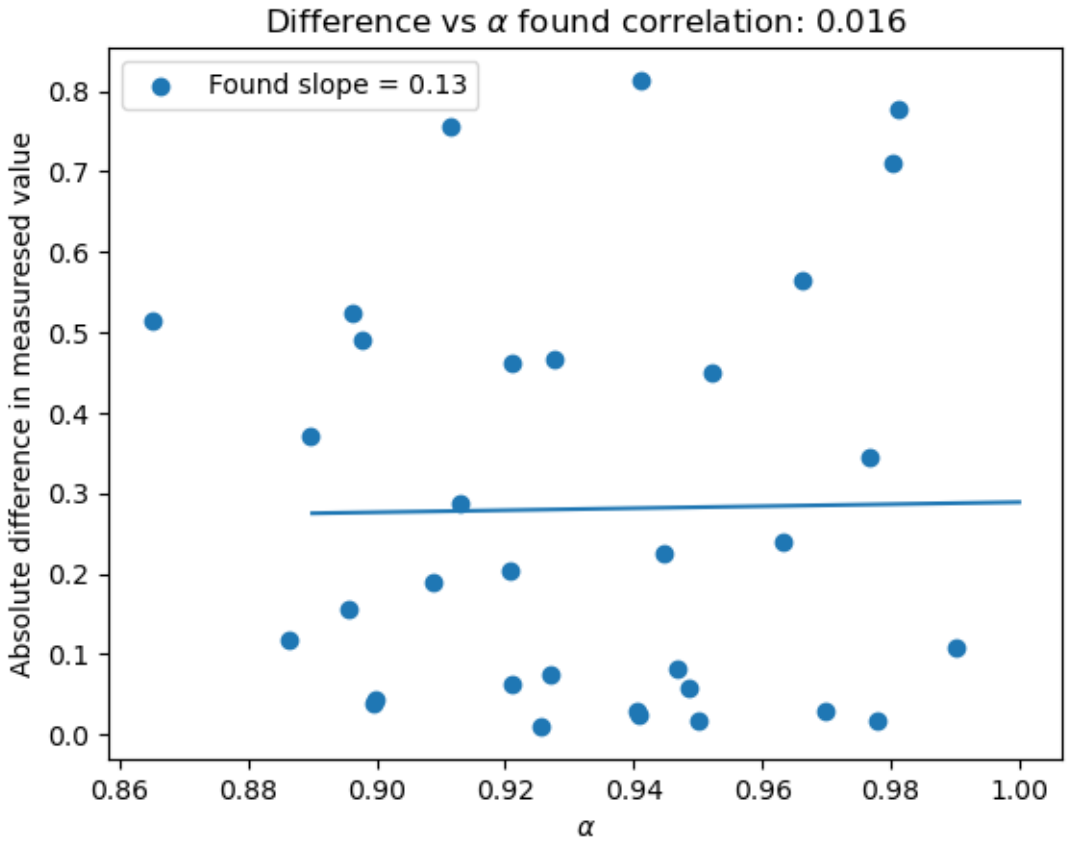

Figure 79: Difference versus α. Correlation plotted as a line.

7.6 Conclusion

After working with both these devices we find that each have their own pros and cons. We have summarised these as the following:

- **Optical Scanner:**
  - Capable of measuring (an)isotropy
  - Faster measurements and capable of measuring several at the same time.
  - More data points, it generates a stream of data which could in theory even be more analysed than in this paper
  - The core does not need to be cut into smaller pieces to be able to fit into the measuring device.
- **Hot Disk:**
  - Can be put in an oven to mimic the in-situ environment
  - Only one single measurement
  - It takes an average of an area of one axis and is not capable of measuring (an)isotropy
  - Time-consuming, slow measurement and only one sample at the time

Additionally, we have compared measurements done by both devices. We conclude that there does not seem to be a relative-bias between the devices.

8 Earth Observation

Past analysis of geothermal regions have shown that exploration of geothermal energy causes surface displacement. It can also be observed during the drilling phase. For instance the geothermal power plant located south of the city of Landau, Germany had been running successfully since 2007, but the production stopped on 14 March 2014, when a major surface deformation was observed in the vicinity of the plant. Synthetic Aperture Radar (SAR) acquisitions from the TerraSAR-X satellite were used to analyse surface deformation in that region and a displacement map was created which indicated an average 5 cm per year uplift during the study period [13].

8.1 Analysis of InSAR Data

Preparation: Copernicus Open Access Hub is a portal that provides free access to Sentinel data through an interactive user interface. The Sentinel Application Platform (SNAP) is an earth observation data processing tool which allows analysis of satellite imagery data. A time period of approximately eight years between 25th December 2015 and 26th September 2023 has been studied. The data used is captured by Sentinel-1 satellite. The swath mode is Interferometric Wide (IW) and type of data is Single Look Complex (SLC).

8.1.1 Steps involved in preparing a displacement map of the region using InSAR

1. Visit Copernicus Hub and select area of interest (AOI).
2. Download the data which consists of multiple TIFF files.
3. Download The Sentinel Application Platform (SNAP).
4. Import data on SNAP.
5. Split data and focus on sub swaths of interests to reduce processing time.
6. Read1 and Read2 uses the data imported to SNAP (1 refers to the data of reference date i.e. 25th December 2015 while 2 refers to the latest data used 26th September 2023 as indicated in Figure 80. They are called master and slave images respectively.
7. Apply Orbit File: Provides accurate satellite position and velocity information.
8. Back Geocoding: Co-registration ensures that each ground target contributes to the same pixel on range and azimuth in both master and slave images.
9. Enhanced Spectral Diversity: performs range and azimuth correction for overlapping bars. It is a refinement step.
10. Interferogram: Represents the phase difference between the 2 images (master and slave images). The interferogram contains both topography and deformation information.
11. TOPSAR Deburst : Our image consists of series of bursts so we deburst the image in order to produce a continuous coverage of the ground.
12. Coherence: Coherence values vary between 0 and 1 which is an indirect measurement of the quality of interferogram. Areas of high coherence appear bright otherwise dark. Bright and white areas have a coherence value close to 1 and represent buildings and urban areas while dark and black areas have a coherence value close to 0 and represent vegetated areas.
13. Topo-phase removal: For this step we design a processing chain where the final output will be the differential interferogram which contains only the deformation.
14. Multi look : Reduce speckle noise and improves image interpretability.
15. Goldstein phase filtering : Reduce phase noise for visualisation purposes.
16. Snaphu export: Export the date for processing in order to apply the phase unwrapping.
17. Phase unwrapping: Phase information is wrapped within the interval [-π, π]. Phase unwrapping is the process of removing phase ambiguities and reconstructing the true continuous phase values. This is crucial for quantitative analysis, as the wrapped phase values do not directly correspond to the actual ground displacement.
18. Phase To Displacement: converts phase into displacement and creates a displacement map as shown in Figure 84.

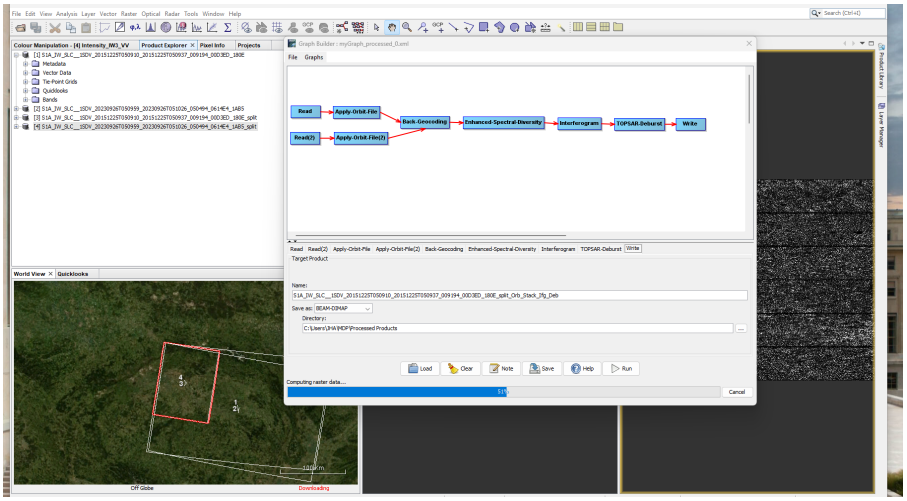

Figure 80: Screenshot of data processing using Sentinel Application Platform (SNAP).

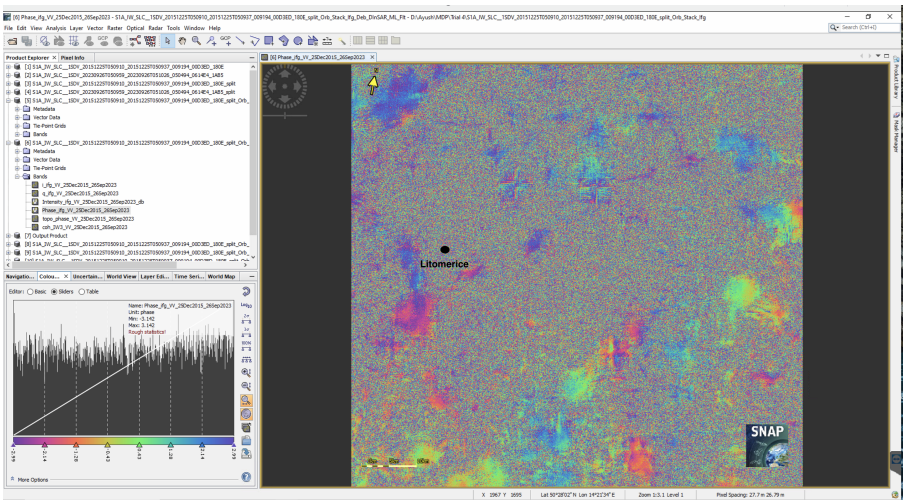

Figure 81: Interferogram: is a visual representation of the phase difference between two synthetic aperture radar (SAR) images of the same area acquired at different times. It contains information of both phase and topography.

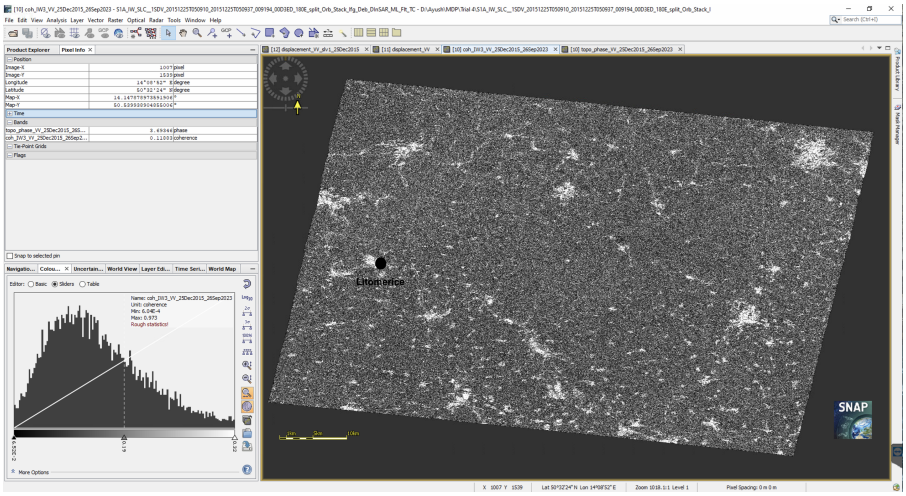

Figure 82: Coherence: is an indirect measure of the quality of interferogram. A value of 1 means high coherence whereas 0 means low coherence. Areas of high coherence appear bright otherwise dark. Dark areas may represent vegetated areas while white ones urban areas.

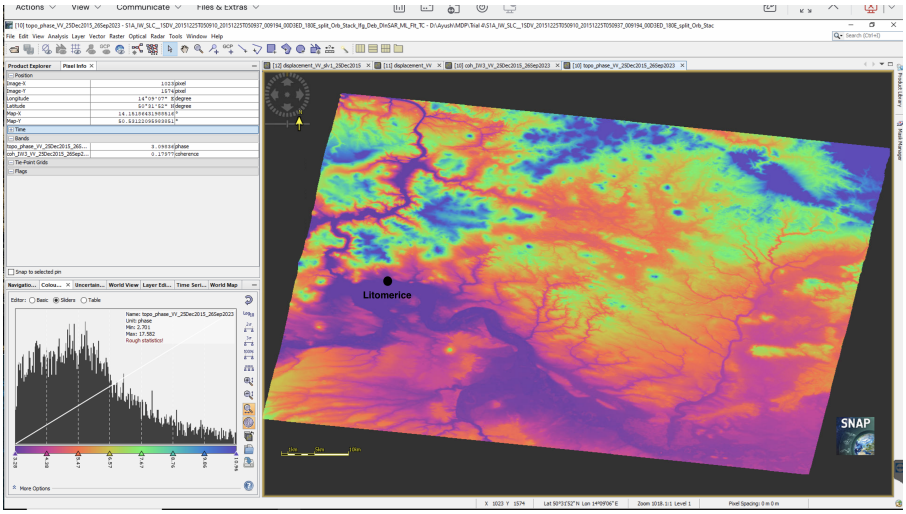

Figure 83: Topography: indicates landform features such as altitude.

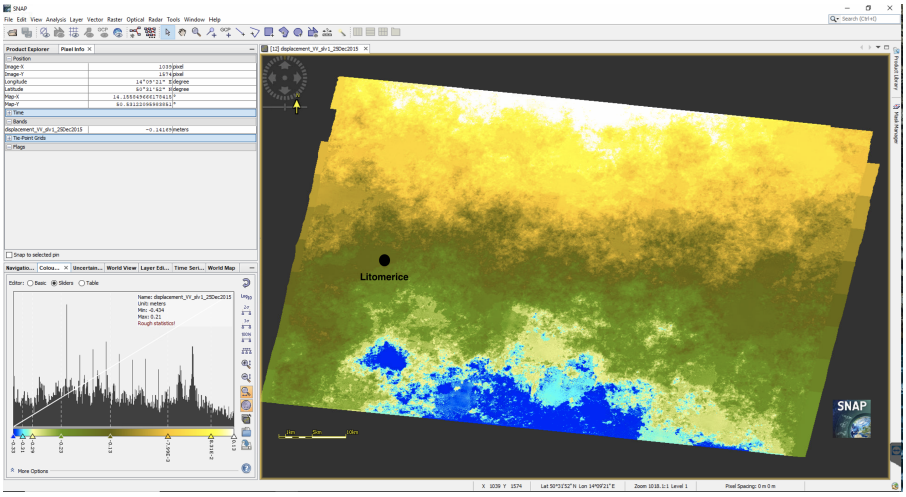

Figure 84: Displacement Map of the region: Blue region denotes subsidence while the white region denotes uplift. The other colours denote intermediate values as shown in the figure. The region of Litomerice falls in the value of about -0.13 metres which indicates subsidence. The blue region is the outskirts of Prague where construction activities and urbanisation may be responsible for the subsidence that we see in the region.

8.2 Analysis of GNSS Data

Global Navigation Satellite System (GNSS) data of Litomerice was used to study past surface deformation in the region. Five years of data between 2018 and 2022 from the Institute of Rock Structure and Mechanics, Czech Academy of Sciences was obtained which needed to be processed. It included 5 years of data with 365 files for each year. However, due to time and processing constraints we analysed monthly data only so there are 12 data points for each year. Data files were extracted and run through a software tool called PPP (Precise Point Positioning) Direct to obtain a SUM (Summary) file which contained parameters and results of the processing. Data of height, latitude, longitude and epoch were extracted from the SUM files. Finally, the following plots were obtained indicating change of various parameters over time.

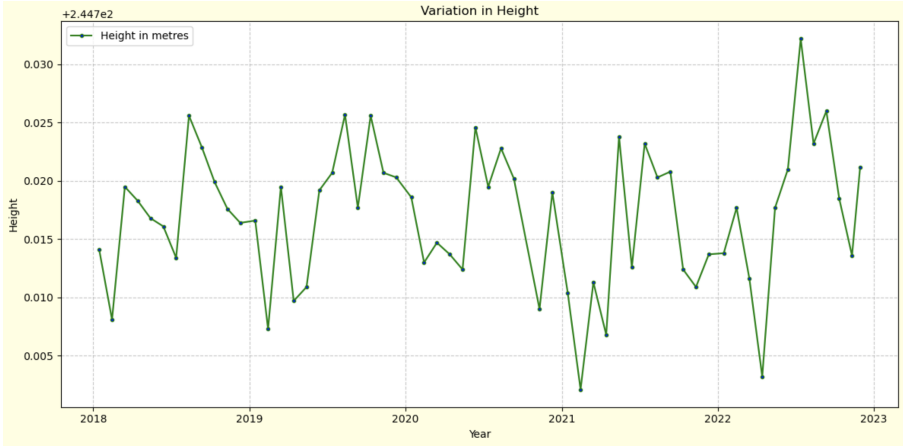

Figure 85: Vertical deformation

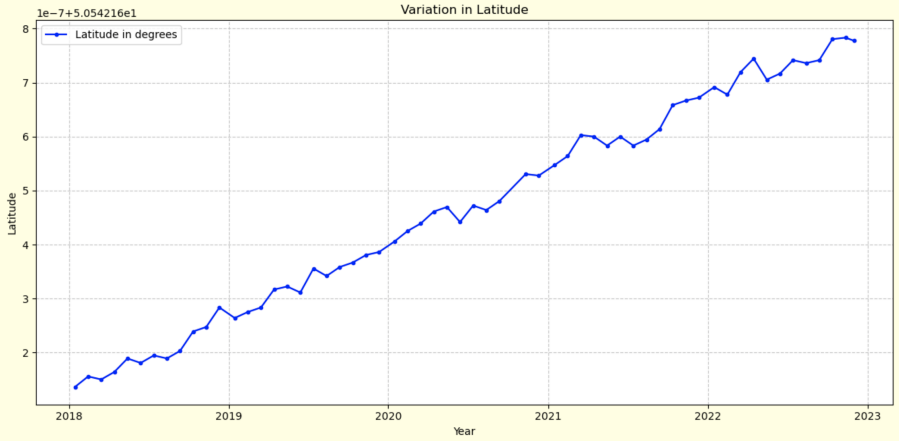

Figure 86: Variation in Latitude

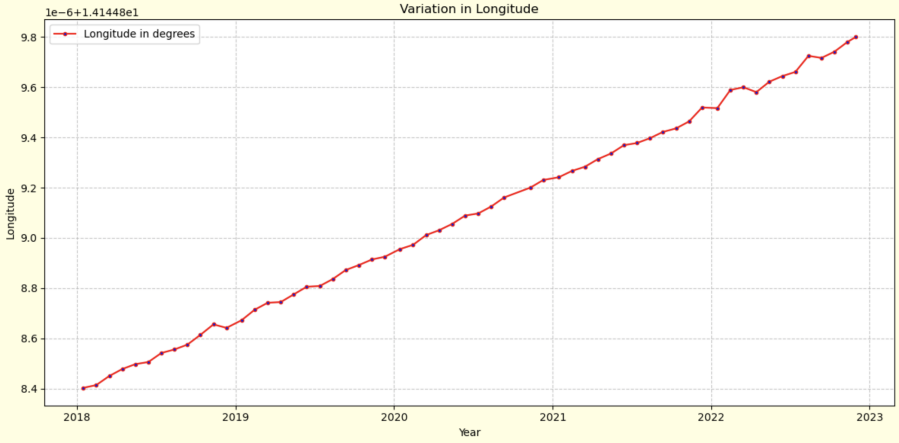

Figure 87: Variation in Longitude

The analysis of GNSS data indicates an uplift of approximately 7 mm between the years 2018 and 2022 as in Figure 85. However, there is seasonality over the years. During winter, colder temperatures can lead to the contraction of materials such as soil and rocks. This contraction can result in subsidence as the materials compress under the lower temperatures. Conversely, in summer, warmer temperatures can cause the expansion of materials, leading to uplift. As the ground warms up, materials like soil and rocks expand, potentially causing the observed uplift. The region seems to be slowly moving northwards and eastwards as latitude and longitude values increase marginally as indicated by Figure 86 and Figure 87. The latitude changes by approximately 6×10^{-7} degrees while the value for change in longitude is 14×10^{-7} degrees. In terms of distance these values can be approximated as 66 mm and 99 mm respectively [7]. This could be attributed to movement of plate tectonics[15].

8.3 Conclusion

The well in the region does not seem to have contributed to any kind of subsidence or uplift. However, such monitoring is necessary if deeper wells are drilled in the future as they may contribute to surface deformation. GNSS is helpful when both horizontal and vertical deformations need to be monitored. Geodetic monitoring can also help determine the history and origin of incidents. Complementary methods like levelling have also been proved to be effective and can be used in the future for monitoring surface displacement in addition to techniques such as InSAR and GNSS used in the project.

9 Discussion potential BTES simulation

An initial goal of the project was also to develop a simulation model for the BTES. We were asked to develop a model of the BTES field, and take water flow within the cretaceous sediments into account.
We have started building a simulation based on the open-darts infrastructure[19]. DARTS is generally used for all kind of geothermal applications, we could not find a BTES application so far. We built an model with cyclic warm and cold water injection, mimicking BTES. Futhermore to simulate a constant ground-water flow we used volume controlled wells injection and production wells outside of the domain we are interested in. This creates a constant flow within the region we are interested in.
The idea of a proper simulation was however abandoned, exploratory drilling was delayed and it made more sense to shift our focus to other parts of the report, as this drilling data would play a big part of the simulation.

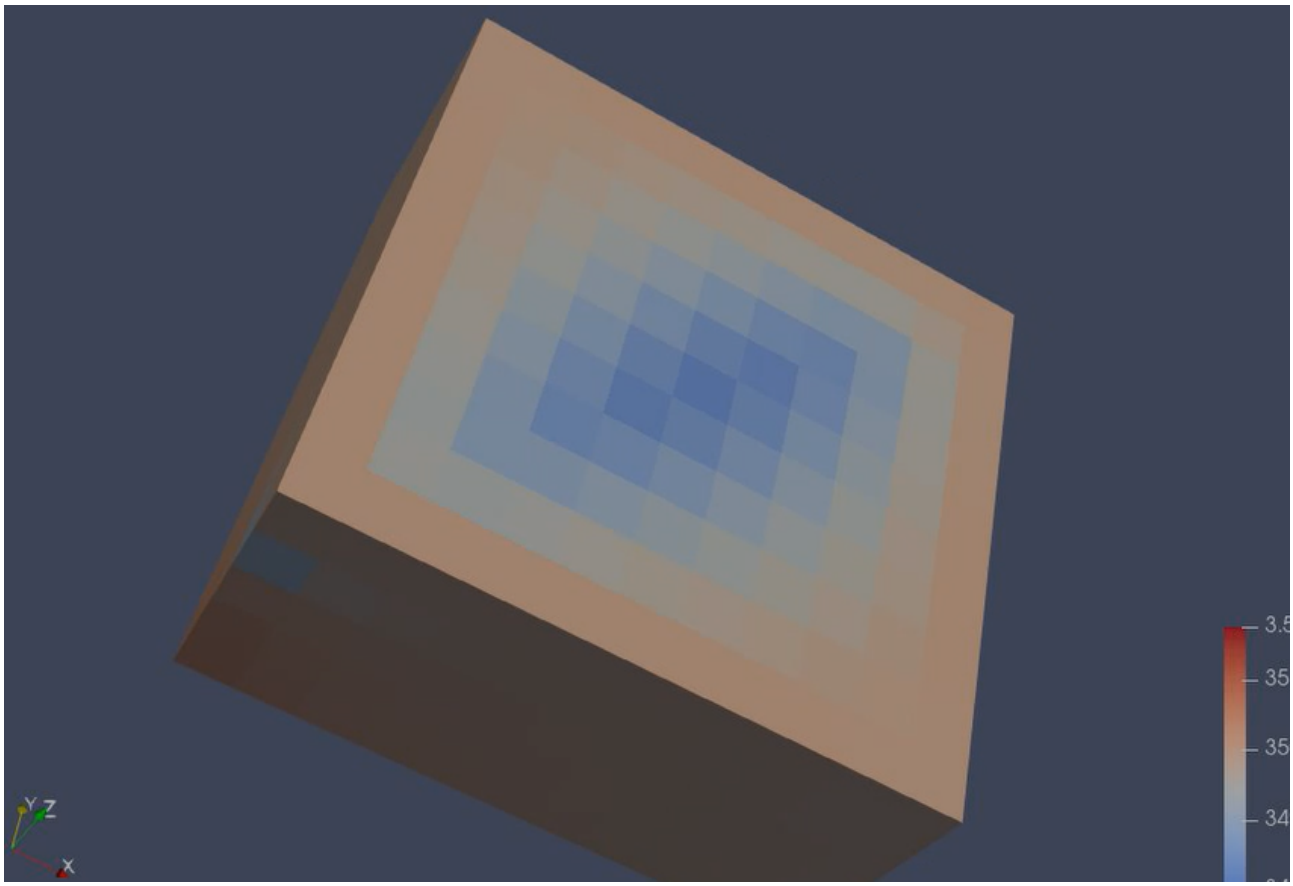

Figure 88: A screenshot from an early model

10 Synthesis of our findings

In this multidisciplinary project, several aspects of geosciences are combined to investigate a promising geothermal region. The regional geology of the Litoměřice area has unique potential for geothermal development. Due to the extensional movement which started in the Oligocene and the subsequent crustal thinning the heat flux increased. This increased heat flux makes the area interesting for a geothermal project. By using a wide range of techniques, a better understanding of the geothermal potential can be obtained. Studying the geology and linking it to the borehole data gave an idea of the different geological units in the subsurface around the RINGEN site. The areas of focus in this project were diverse, but are all critical for future development of the Litoměřice geothermal site.

In terms of understanding the shallow geology, the three methods of geophysical measurements (ERT, semismics, and gravity data) can all be compared to each other to create a single image and understanding of the subsurface. This is especially important for the array of shallow borehole thermal energy storage wells. In addition to the shallow BTES wells, the shallow geophysical methods can give insight into the geology for drilling purposes. Every well at the site is drilled through the shallow units of the area.

Additionally, the results from the injection test and related well testing analysis can give insight into the shallow subsurface. It is now known that the fracture in the PVGT-LT1 well is connected to a shallower unit. This information can be potentially combined with these geophysical measurements or future measurements.

The comparison of the two different methods to determine thermal properties gave insights on the applicability of the measurement devices. The scanner is best applicable to get a quick overview of a large number of samples in a time efficient manner while the Hot Disk is better for further in-depth research of the thermal properties in a realistic environment.

Finally, there are a number of risks associated with EGS systems and other geothermal systems. The remote sensing techniques used in this study will be useful in establishing a baseline for any future measurements to be compared to. This will be critical in detecting potential anomalies such as uplift or other regional changes before they potentially become issues.

References

Adamovič, J., & Coubal, M. (1999). Intrusive geometries and cenozoic stress history of the northern part of the bohemian massif. *Geolines*, *9*, 5–14.

Anastasiia, M., Jan, Č., Lubomil, P., & Jiří, A. (2022). New geophysical and geological data on the moldanubian plutonic complex and the kaplice fault, southern bohemia. *International Journal of Earth Sciences*, *111*(4), 1315–1331.

Appendix 6 seismic refraction method a 6. (2014). Retrieved from https://api.semanticscholar.org/CorpusID:214622229

Bourdet, D., Ayoub, J. A., & Plrard, Y. M. (1989, 06). Use of Pressure Derivative in Well-Test Interpretation. *SPE Formation Evaluation*, *4*(02), 293-302. Retrieved from https://doi.org/10.2118/12777-PA doi: 10.2118/12777-PA

Cajz, V., Rapprich, V., Erban, V., Pecskay, Z., & Radoň, M. (2009). Late miocene volcanic activity in the české středohoří mountains (ohře/eger graben, northern bohemia). *Geol Carpath*, *60*(6), 519–533.

Čermák, V., Král, M., Krešl, M., Kubik, J., & Šafanda, J. (1991). Heat flow, regional geophysics and lithosphere structure in czechoslovakia and adjacent part of central europe. In *Terrestrial heat flow and the lithosphere structure* (pp. 133–165). Springer.

Data Scout. (2016, August). *Distance between points.* Retrieved from https://www.thedatascout.com/2016/08/09/distance-latitude-longitude/

et al., J. P. (2010). Terciérní pánve a ložiska hnědého uhlí české republiky (tertiary basins and soft coal seams of the czech republic).. Retrieved from https://api.semanticscholar.org/CorpusID:132189957

Fischer, T., Vlček, J., Dědeček, P., Řihošek, J., Zimmermann, G., Holeček, J., ... Káldy, E. (2023). Hydraulic injection tests in the pilot egs borehole pvgt-lt1 in litoměřice, czechia. *Geothermics*, *115*, 102805.

Foti, S., Hollender, F., Garofalo, F., Albarello, D., Asten, M., Bard, P. Y., ... Socco, L. (2017, 9). Guidelines for the good practice of surface wave analysis: a product of the InterPACIFIC project. *Bulletin of Earthquake Engineering*, *16*(6), 2367–2420. Retrieved from https://doi.org/10.1007/s10518-017-0206-7 doi: 10.1007/s10518-017-0206-7

Gustafsson, S. E. (1991). Transient plane source techniques for thermal conductivity and thermal diffusivity measurements of solid materials. *Review of scientific instruments*, *62*(3), 797–804.

Gustavsson, M., Karawacki, E., & Gustafsson, S. E. (1994). Thermal conductivity, thermal diffusivity, and specific heat of thin samples from transient measurements with hot disk sensors. *Review of Scientific Instruments*, *65*(12), 3856–3859.

Heimlich, C., Masson, F., Gourmelen, N., Schmittbuhl, J., Azzola, J., & Kim, S. W. (2014, December). Uplift Around the Geothermal Power Plant of Landau (Germany) Observed from InSAR Monitoring. In *Agu fall meeting abstracts* (Vol. 2014, p. H41I-06).

Himi, M., Anton, M., Sendrós, A., Abancó, C., Ercoli, M., Lovera, R., ... Casas, A. (2022). Application of resistivity and seismic refraction tomography for landslide stability assessment in vallcebre, spanish pyrenees. *Remote Sensing*, *14*(24). Retrieved from https://www.mdpi.com/2072-4292/14/24/6333 doi: 10.3390/rs14246333

Horne, R. N. (1990). *Modern well test analysis.* American.

Kappa engineering. (n.d.). Retrieved from https://www.kappaeng.com/software/saphir/overview

Mazanec, M. (2023, 9). Surface waves as a cost-effective tool for enhancing the interpretation of shallow refraction seismic data. *Acta Geodynamica et Geomaterialia*, 121–138. Retrieved from https://doi.org/10.13168/agg.2023.0012 doi: 10.13168/agg.2023.0012

Mlcoch, B., & Konopasek, J. (2010). Pre-late carboniferous geology along the contact of the saxothuringian and teplá-barrandian zones in the area covered by younger sediments and volcanics (western bohemian massif, czech republic). *Journal of Geosciences*, *55*(2), 81–94.

Open Darts Contributors. (Year of Access). *Open darts.* https://gitlab.com/open-darts/open-darts. (Accessed: 9 10, 2023)

Ozkan, E., & Dean, E. (2017, Setember). *Lecture notes on well test analysis and design.* Colorado School of Mines Petroleum Engineering.

Popov, Y., Semionov, V., Korosteliov, V., & Berezin, V. (1983, 01). Non-contact evaluation of thermal conductivity of rocks with the aid of a mobile heat source. *Phys. Solid Earth*, *19*, 563-567.

Šafanda, J., Verner, K., Franěk, J., Peřestỳ, V., Holeček, J., & Fischer, T. (2020). Geology and geothermal potential in the eastern flank of eger rift (litoměřice area, czech republic). *Geothermics*, *86*, 101808.

Sensornet dts. (2021, Feb). Retrieved from https://www.sensornet.co.uk/sentinel-dts-sensors/

Simyrdanis, K., Papadopoulos, N., & Oikonomou, D. (2021). Computation of optimized electrode arrays for 3-d electrical resistivity tomography surveys. *Applied Sciences*, *11*(14), 6394.

Smarttomo. (2021). *An introduction to seismic refraction tomography (srt).* Retrieved from https://www.smarttomo.com/wp/documents/an-introduction-to-seismic-refraction-tomography-srt/

Solinst levelogger. (2020). Retrieved from https://www.solinst.com/products/dataloggers-and-telemetry/3001-levelogger-series/levelogger/

Stampfli, G. M., & Borel, G. D. (2004). The transmed transects in space and time: constraints on the paleotectonic evolution of the mediterranean domain. In *The transmed atlas. the mediterranean region from crust to mantle: Geological and geophysical framework of the mediterranean and the surrounding areas* (pp. 53–80). Springer.

Št'ovíčková, N. (1973). Deep-fault tectonics and its relation to endogenous geological processes. *Academia, Prague*, 1–198.

Uličnỳ, D., Laurin, J., & Čech, S. (2009). Controls on clastic sequence geometries in a shallow-marine, transtensional basin: the bohemian cretaceous basin, czech republic. *Sedimentology*, *56*(4), 1077–1114.

U.S. Geological Survey. (1997). Introduction to potential fields: Gravity. *Fact Sheets*(FS–239–95). Retrieved from https://pubs.usgs.gov/fs/1995/fs239-95/ (U.S. Geological Survey Fact Sheets. FS–239–95.)

Ziegler, P. (1990). *Geological atlas of western and central europe.* London: Geological Society of London.

A Borehole information

Figure 89: Information on boreholes.

Our ID — different names of the boreholes… — length — direction — inclination — diameter

mine floors	id	Dokumentační bod	Databáze vrtů SÚRAO/DIAMO						
			Index důlního díla	Název vrtu SÚRAO	Staniční (m)	Délka (m)	Směr (°)	Sklon (°)	Průměr (mm)
12th floor	T1	296VFA0001	BZ-XIIJ *	S-4	117,8 *	50,0 *	270	-1	76
12th floor	T2	296VFA0002	ZK-1	ZK1-16D	16,0	15,3	-	-89	76
12th floor	T3	296VFA0003	BZ-XIIJ(VrK-1)	S-7	244,0	15,0	130	10	76
12th floor	T4	296VFA0004	BZ1-XII	BZ1-XII-55R	54,7	15,3	2	-7	76
3rd floor	T5	296VFA0005	BZ-III	BZ-III-5Fc	-5,4	15,3	82	-3	72
5th floor	T6	296VFA0006	Z-V	Z-V-40L	40,0	15,2	172	-5	72
9th floor	T7	296VFA0007	BV-IX 9.p. B-1	C-01	7,9	16,3	171	-4	72
12th floor	T8	296VFA0008	Z3-XII	ZV	103,6	33,9	173	2	59* (76)

Figure 90: Depths of samples per borehole as well as slope of lineation in samples.

Borehole	sample	Slope
T1_S4	1,05 - 1,2	60-70
	5,2 - 5,4	20-30
	10,8 - 10,9	60-70
	14,2 - 14,4	50-60
T2_ZK1-16D	2 - 2,1	48 a 25
	7,1 - 7,35	33 a 46
	11,6 - 11,8	34 a 40 a 39
	15 - 15,1	35
T3_S7	1,3 - 1,5	??
	5,7 - 5,75	50-60
	7,5 - 7,6	??
	10 - 10,25	65-75
	14,05 - 14,2	20-30
T4_BZ1-XII-55R	2 - 2,2	43
	5,6 - 5,8	40 a 39
	11,7 - 11,8	40 a 61 a 32
	14,6 - 14,8	33 a 37 a 54 a 50
T5_BZ-III-5Fc	1,3 - 1,4	??
	3,1 - 3,2	30
	7,3 - 7,5	20-30
	9,7 - 9,8	20-30
T6_Z-V-40L	1,6 - 1,75	70-80
	5,6 - 5,8	70-80
	9,5 - 9,6	70-80
	13,7 - 13,9	80
T7_C01	2 - 2,15	40
	2-2,15	40
	8-8,2	70-80
	12	??? 80
	16.2	70-80
T8_ZV	1	50
	5	70
	10	65
	15	60

B Additional seismics images

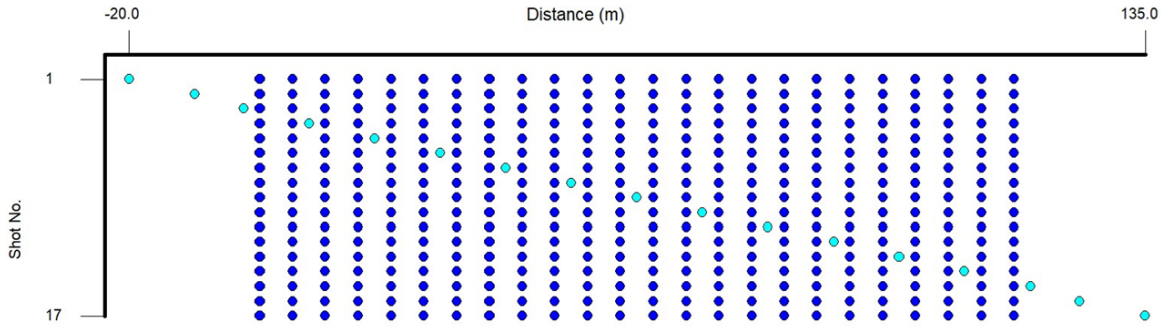

Figure 91: Layout of shot and geophone locations including offset shots

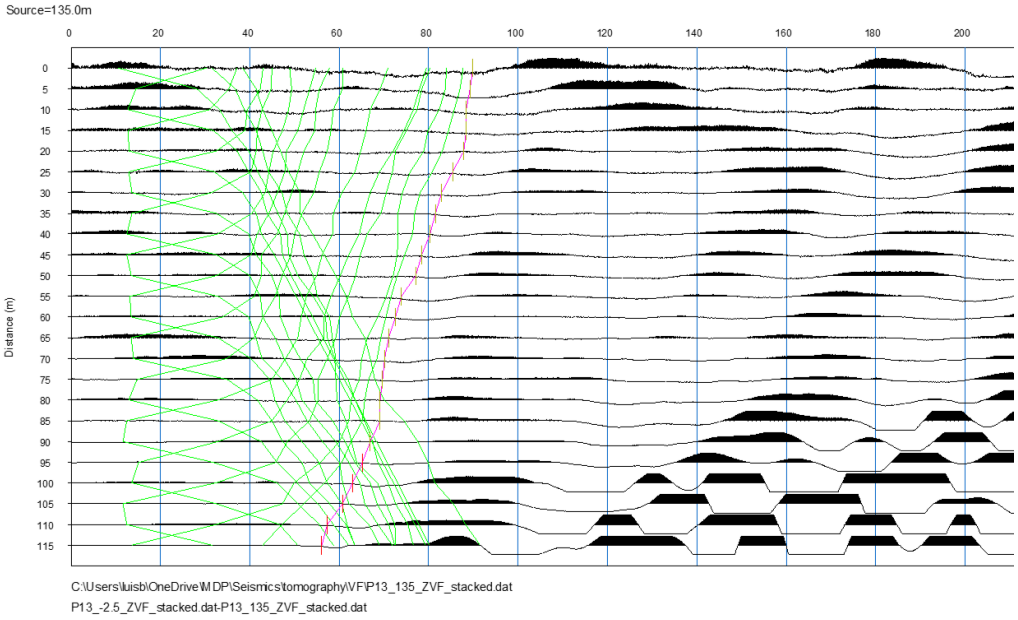

Figure 92: Example SeisImager screenshot for the picking of first arrival times

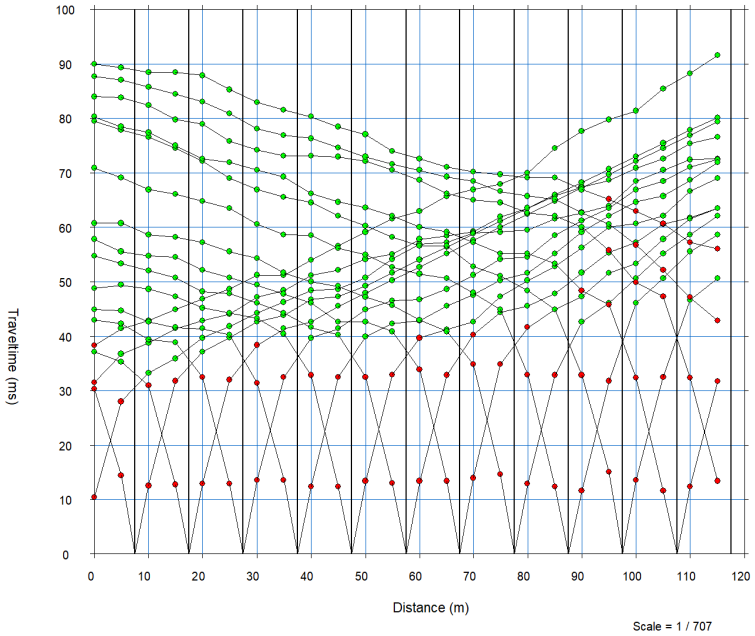

Figure 93: Traveltime curves with breaks highlighted for the refraction seismic analysis

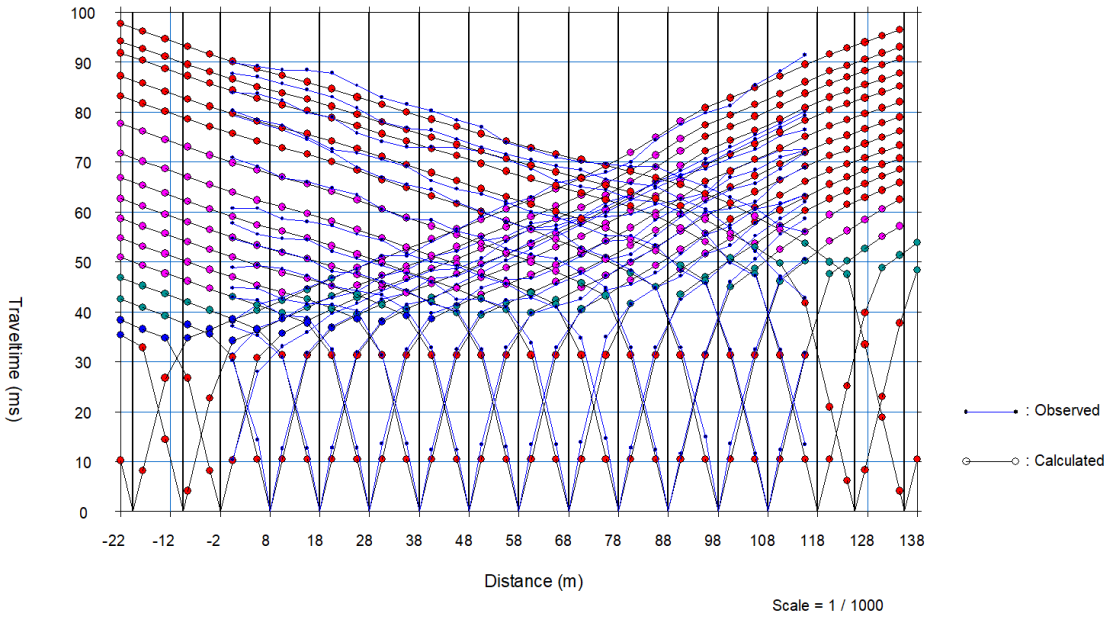

Figure 94: Observed traveltime curves plotted next to the calculated curves from the inversion

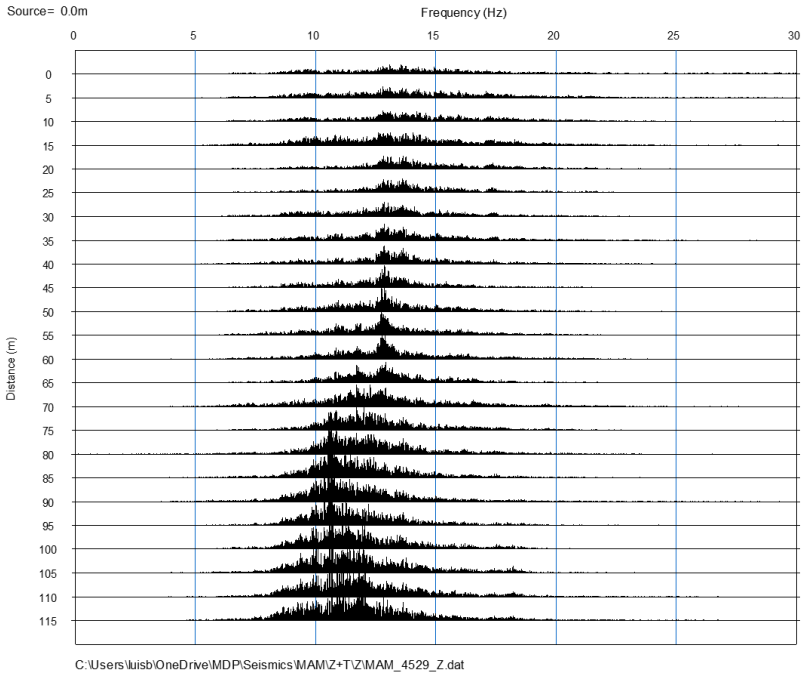

Figure 95: Measured MAM data displayed in the frequency domain

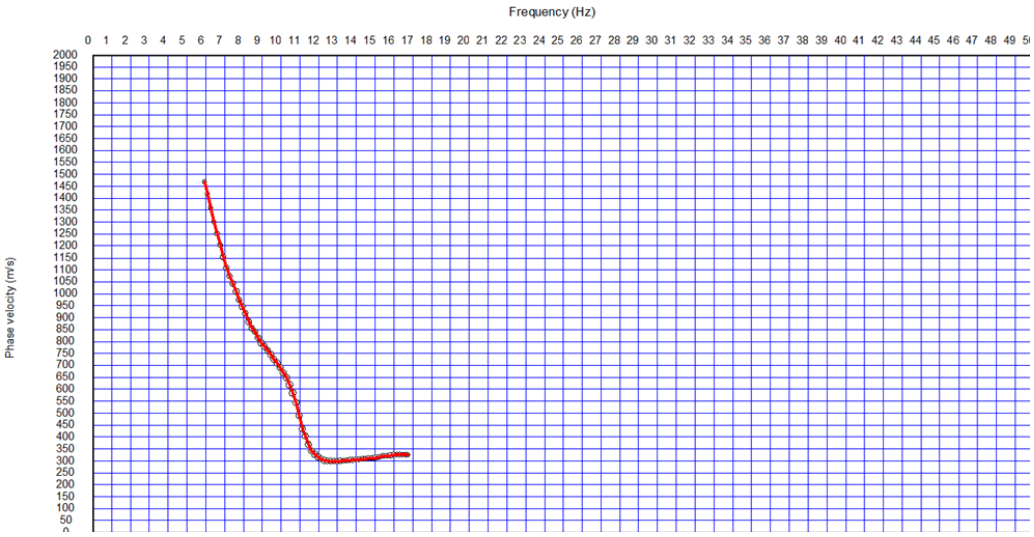

Figure 96: Dispersion curve created from the MAM image

Figure 97: Dispersion curve created from the MASW image

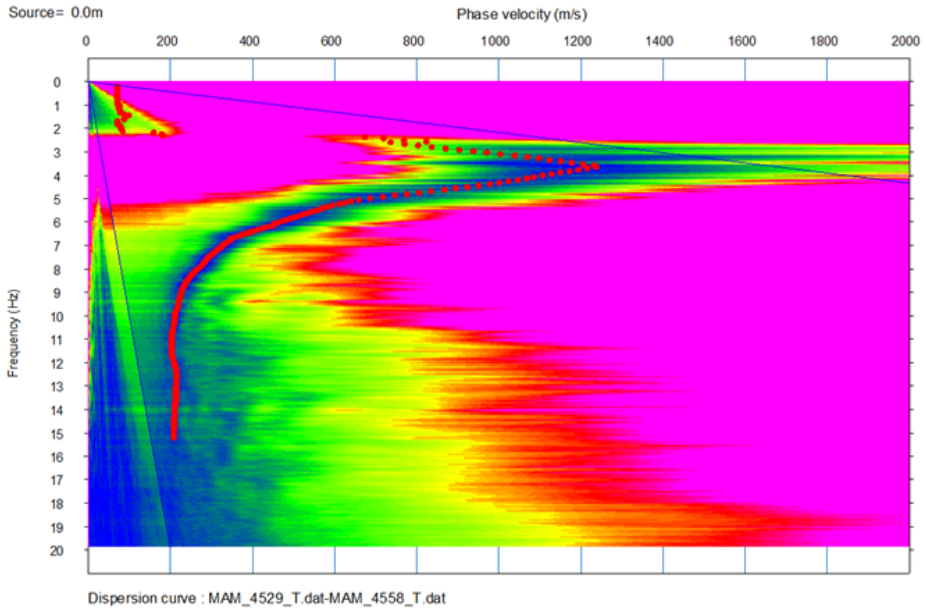

Figure 98: Dispersion image of the passive MAM survey